Oxyhydrides – Synthesis, Crystal Structure and Properties

Øystein Slagtern Fjellvåg

Dissertation for the degree of Philosophiae Doctor

Department of Chemistry

Faculty of Mathematics and Natural Sciences

University of Oslo

Preface

This thesis is submitted in partial fulfillment of the requirements for the degree of *Philosophiae Doctor* at the Department of Chemistry, Faculty of Mathematics and Natural Sciences, University of Oslo (UiO). The experimental work presented has been carried out at the research group for Nanostructures and Functional Materials (NAFUMA) at UiO, ISIS pulsed neutron and muon source, the Swiss-Norwegian beamlines (SNBL) at ESRF, and the CRISMAT laboratory in Caen, between August 2014 and December 2018 as a part of the strategic research initiative FOXHOUND. Professor Dr. Anja Olafsen Sjåstad and Associate Professor Dr. Anette Gunnæs have supervised the work and first I would like to express my sincere gratitude to them. A special thanks to Anja for always encouraging me and my ideas, and her endless support.

Thanks to my co-authors, Wojtek, Jeff, Vajeeston, Kristin, Vegar and Magnus. A special thanks to Kristin for her master work, which is included in **Paper II**. I would like to thank Matthew Krzystyniak for carrying out NCS measurement and analysis, and Wojtek for carrying out neutron PDF analysis. Thanks to Magnus at IFE for carrying out neutron diffraction experiments, the staff at ISIS pules neutron and muon source and SNBL at ESRF for experimental support, and David Wragg for discussions and assistance with diffraction experiments at the home laboratory. Thanks to Erik and Nicolai for joining beamtimes at ISIS pulsed neutron and muon source.

I would like to thank Felix Fernando-Alonso for fruitful discussions and for putting me in contact with Jeff, and a most sincere gratitude is directed towards Jeff for our collaboration and the beamtimes at ISIS pulsed neutron and muon source. This thesis would not have been the same without your interest and efforts. Large thanks also to Philippe Boullay, Bruno Gonano, Yohann Breard and the other guys in Caen for showing great hospitality and cycling enthusiasm, in addition to our attempts with PEDT.

Great colleagues and friends have been valuable the last years, and I would like to thank Asbjørn, Henrik, Ina, Ingvild, Jon Einar, Kristian, Magnus and the rest of the NAFUMA staff. A special thanks to Amund for being a great office-mate and cycling companion.

At last, I would like to thank Ingrid Marie, my parents, the rest of my family and friends for support during the last years.

Summary

This thesis is focused on the research of a new and scarcely explored material class where the compounds are described to have a lattice consisting of both oxide and hydride anions, so-called oxyhydrides. Their exotic nature, with respect to the mixed anion lattice, has attracted attention as it may open for new technology based on hydride anion conductivity. The aim is to investigate aspects of selected oxyhydrides and add this material class to the portfolio of the NAFUMA research group.

In this work, selected oxyhydrides described by the formula $La_{2-x}Nd_xLiHO_3$ ($0 \leq x \leq 2$) have been obtained by a halide salt flux method in large quantities (gram scale), which is in contrast to the usual mg scale for high-pressure approaches. Large sample quantities are particularly useful with application in mind or for fundamental investigations using probes requiring substantial material quantities. We furthermore describe key factors for preparation of oxyhydrides by this approach, and we discover lithium chloride to serve as an excellent flux also below its melting temperature. This finding opens for a completely new temperature range for synthesis of oxyhydrides, and phase pure Nd_2LiHO_3 was in this work produced phase pure for the first time by operating the halide salt flux at low temperatures.

The thermal aspects of the $La_{2-x}Nd_xLiHO_3$ oxyhydrides have been investigated by the means of *in situ* SR-XRD, TGA-DSC-MS and QENS; leading to the conclusion that the oxyhydride decomposes at around $400-450\,°C$, with $Ln_2LiO_{3.5}$ as the main decomposition product. It is speculated if the decomposition is kinetically controlled and facilitated by the increased hydride anion mobility around the decomposition temperature. Further, a decreasing decomposition temperature is observed with increasing neodymium content, both at oxidizing conditions (in air) and in the reductive synthesis flux.

By means of X-ray and neutron diffraction, aspects connected to the crystal structures of La_2LiHO_3, $LaNdLiHO_3$, $La_2LiO_{3.5}$, $LaSr_3Fe_3O_9$ and $LaSr_3Fe_3H_{1.1}O_{8.9}$ are explored at short- and long length scales. The crystal structure of the four latter compounds are described for the first time in this thesis (a new polymorph of $La_2LiO_{3.5}$ is described). La_2LiHO_3 and $LaNdLiHO_3$ are confirmed to take the orthorhombic RP1 type crystal structure, and interestingly for La_2LiHO_3 neutron PDF indicate a change in the local structure at elevated temperatures. $La_2LiO_{3.5}$ prepared in this work showed a structural distortion compared to the reported tetragonal RP1 structure and was successfully described to take an orthorhombic structure.

In addition to structural determination of oxyhydrides by X-ray and neutron diffraction, PEDT was evaluated as a probe for structural determination and verification of hydride anions in oxyhydrides with basis in electron diffraction. The crystal structure of La_2LiHO_3 was determined by PEDT. However, due to twinning, satisfactory refinements were not possible to perform.

Therefore, the feasibility of PEDT for structural determination and verification of hydride anions in oxyhydrides was not proven and remains pending.

Neutron spectroscopy is employed to investigate details connected to bonding and diffusion in La_2LiHO_3. INS combined with DFT modelling confirm the presence of hydride anions in the compound. Furthermore, the bonding is described by DFT and found to be anisotropic, with covalent lanthanum-oxygen bonds in the rock salt layer and ionic bonding around lithium in the perovskite layer. Calculations show the favorable migration path for the hydride anions to be within the perovskite layer. We further calculated surprisingly high migration barriers for the hydride anions to migrate into and within the rock salt layer, which we link to the covalent bonding in the rock salt layer. With basis in the bonding considerations and migration barriers, we describe guidelines for design of new oxyhydrides which we believe should display enhanced hydride anion conductivity compared with La_2LiHO_3.

The momentum distribution of the hydride anions in La_2LiHO_3 measured by NCS was successfully described by a phonon model calculated from DFT, indicating that additional dynamics, *i.e.* diffusion, for the hydride anions is absent in the system. However, what is observed is reduced binding energy of the hydride anions with increasing temperature when comparing the measured momentum distribution with that calculated from the Maxwell-Boltzmann approximation of a free not interacting particle. Thus, we suggest that the decomposition of the oxyhydride originates in reduced binding energy of the hydride anions. Altogether, the various techniques employed to study hydride anion diffusion in La_2LiHO_3 show that hydride anion diffusion is absent in the samples prepared in this work.

Oxygen vacant $LaSr_3Fe_3O_{10-x}$ ($0 \leq x \leq 1.21$) composition are investigated with respect to phase content relations, crystal structure and magnetic properties. Two distinct crystallographic phases ($LaSr_3Fe_3O_{10-\delta}$ and $LaSr_3Fe_3O_{9\pm\epsilon}$) are documented, and a two-phase region for $0.51 < x < 0.85$ is verified. We report $LaSr_3Fe_3O_9$ to take a RP3 related crystal structure with brownmillerite elements, and to be antiferromagnetic to above 350 K with a G-type magnetic structure. With basis in the fundamental knowledge acquired for $LaSr_3Fe_3O_{10-x}$, attempts to prepare corresponding oxyhydrides by topotactic anion-exchange with CaH_2 was carried out. Preliminary neutron diffraction experiments indicate successful preparation of an oxyhydride with the composition $LaSr_3Fe_3H_{1.1}O_{8.9}$. However, further investigations are needed to conclude with certainty.

Table of Content

List of Papers

Paper I:

Thermal and Structural Aspect of the Hydride Conducting Oxyhydride La$_2$LiHO$_3$ obtained via a Halide Flux Method

ØS Fjellvåg, J Armstrong, WA Sławiński, AO Sjåstad

*Inorganic Chemistry, **2017**, 56, 11123−11128*

Paper II:

Advances on the LiCl salt flux method and the preparation of phase pure La$_{2-x}$Nd$_x$LiHO$_3$ ($0 \leq x \leq 2$) oxyhydrides

ØS Fjellvåg, KH Nygård, P Vajeeston, AO Sjåstad

*Chemical Communications, **2019**, 55, 3817−3820*

Paper III:

New Insights into Hydride Bonding, Dynamics and Migration in La$_2$LiHO$_3$ Oxyhydride

ØS Fjellvåg, J Armstrong, P Vajeeston, AO Sjåstad

*The Journal of Physical Chemistry Letters, **2018**, 9, 353−358*

Paper IV:

Crystal structure of LaSr$_3$Fe$_3$O$_9$ and its phase relation with LaSr$_3$Fe$_3$O$_{10}$

ØS Fjellvåg, V Øygarden, MH Sørby, AO Sjåstad

*Journal of Solid State Chemistry, **2019**, 275, 56-62*

x

Glossary

AIMD	-	*Ab initio* molecular dynamics
BOP	-	Bond overlap population
ccp	-	Cubic closest packing
cNEB	-	Climbing nudged elastic band method
DFT	-	Density functional theory
DINS	-	Deep inelastic neutron scattering
DSC	-	Differential scanning calorimetry
DTA	-	Differential thermal analysis
e.g.	-	For example
ESS	-	European Spallation Source
Et al.	-	And others
Etc.	-	And more
hcp	-	Hexagonal closest packing
HZB	-	Helmholtz-Zentrum Berlin
i.e.	-	That is
IFE	-	Institute for Energy Technology
ILL	-	Institut Laue-Langevin
INS	-	Inelastic neutron scattering
MS	-	Mass spectroscopy
NCS	-	Neutron Compton scattering
NMR	-	Nuclear magnetic resonance
PDF	-	Pair distribution function
PEDT	-	Precession electron diffraction tomography
PZT	-	$PbZr_{1-x}Ti_xO_3$
QENS	-	Quasi-elastic neutron scattering
RMC	-	Reversed Monte-Carlo
RP	-	Ruddlesden-Popper
SEM	-	Scanning electron microscopy
SQUID	-	Superconducting quantum interference device
SR	-	Synchrotron radiation
STM	-	Scanning tunneling microscope
TGA	-	Thermogravimetric analysis
XAS	-	X-ray absorption spectroscopy
XRD	-	X-ray diffraction
YBCO	-	$YBa_2Cu_3O_{7-\delta}$
YZT	-	Yttria-stabilized zirconia

1. Introduction

1.1 Motivation

Discovery of new materials has been a motivation behind innovation for centuries. This is reflected in how materials have defined civilizations, for example the Stone Age, Bronze Age, and Iron Age have all gained their names from materials. The names reflect the most advanced material in the era, *i.e.* in the Stone Age the tools were made of stone and objects found in nature, in the Bronze Age the tools were made of bronze and in the Iron Age the tools were made of iron. The progress of development is in the superiority of the tools; iron tools are cheaper, stronger and lighter than the bronze equivalents. Advanced materials are the basis for modern technology and in the field of solid-state materials science they are explored and developed. Notably, it is also common to differentiate between load bearing- and functional materials, whereof both material classes are of key importance for today's civilization.

Functional materials are characterized by having their distinct and characteristic properties that can be controlled or exploited. These can be properties as superconductivity, semiconductivity, magnetism, piezoelectricity, ferroelectricity, multiferroicity, optic, catalytic activity or ionic conductivity, all spanning traditional themes in chemistry, physics and materials science, with significant input from engineering.[1-3] Further, functional materials are found in all classes of materials, including ceramics, metals, polymers and organic molecules.

Many functional materials take the perovskite structure (section 2.1). The perovskites are within the field of materials science is considered equally flexible and important as the potato is in food preparations, due to the extreme variety of combinations of cations and anions that can be mixed and still maintain the atomic arrangement of the perovskite. Such compounds turn out to be prime examples of materials with functional properties for technological applications.[4] In the following some few examples will be given.

- Ionic conductivity is a functional property which is exploited in electrochemical devices, such as batteries and fuel cells. In these devices we depend on the ability of ions to migrate through an electrolyte between electrodes, while the electrons are collected by an external circuit which yields electrical energy. In solid oxide fuel cells the fluorite yttria-stabilized zirconia (YZT) is the most common electrolyte, while perovskite are found in the electrodes due to their properties as mixed electronic and ionic conductors.[5] The perovskite $La_{1-x}Sr_xMnO_3$ is the most common cathode material in solid oxide fuel cells.[6]
- The piezoelectric effect is utilized in a wide range of applications. A piezoelectric material gives an electrical voltage as response to a deformation, which *e.g.* is used in sensors to measure pressure.[2] We also find piezoelectric materials to be used in trivial devices as lighters, and in more advanced application as high-precision motors for scanning

tunneling microscopes (STM). The effect is additionally utilized in microphones to detect sound, or in speakers to generate sound. The perovskite $PbZr_{1-x}Ti_xO_3$ (PZT) is the most used piezoelectric perovskite in modern technology.[1] However, extensive research is ongoing to replace PZT with lead-free alternatives.

- Magnetoresistance is the property where the electrical conductivity in a material varies up to several orders of magnitude when exposed to a magnetic field.[7-8] The changes in conductivity can be a few percent in conventional magnetoresistive materials, however, colossal magnetoresistance is a property found in some manganese-based perovskite where the conductivity can vary by orders of magnitude. The prototypical colossal magnetoresistance compound is derived from the perovskite $LaMnO_3$, and possible application in data storage is foreseen, where a material which displays colossal magnetoresistance may be used as a disk read head.[7]

- Superconductivity is an exotic phenomenon associated with zero resistance in a conductor. The phenomena was discovered by Heike Kamerlingh Onnes at Leiden University when he investigated the conductivity of mercury at 4.5 K in 1911.[9-12] 4.5 K is too low temperatures for practical applications, however in 1987 the reduced perovskite $YBa_2Cu_3O_{7-\delta}$ (also known as "YBCO") was reported to be superconducting at 90 K, above the temperature of liquid nitrogen.[13] Thus, YBCO is more applicable in technology, and Bednorz and Müller was in 1987 awarded the Nobel Prize in physics for the discovery of YBCO. Due to the zero resistivity in superconductors, they can be used to generate large magnetic fields, which *e.g.* is utilized in magnetic resonance imaging (MRI); and also detect magnetic fields as in superconducting quantum interference devices (SQUID).[14-15]

- For industrial high-temperature oxidation of ammonia (NH_3) to nitric oxide (NO), Pt/Rh metals is used as catalyst. However, significant amounts of expensive Pt metal is lost in the industrial process.[16-17] An alternative catalyst to Pt/Rh would yield significant economical savings and is therefore desirable. The perovskite $LaCoO_3$ is used as decomposition catalyst of the undesirable byproduct and greenhouse gas N_2O. Due to the fact that $LaCoO_3$ shows low selectivity towards nitrous oxide (N_2O), it can potentially be used as a catalyst for the ammonia oxidation process.[1, 18] However, the current $LaCoO_3$ catalysts do not show sufficiently high selectivity towards nitric oxide and research is ongoing to improve the catalytic activity of the compound.

It is complex to prepare new materials with improved or completely new functional properties. Numerous challenges are encountered; how can we predict the existence of a new material, what is the best strategy to prepare the material, and which material properties will dominate the compound? Material scientists chose different strategies to obtain new materials; spanning from careful design strategies to blue sky research. In this context, mixed-anion compounds (section 2.4), emerge as an unexplored class of materials with great potential.

As different anions (*e.g.* O^{2-}, S^{2-}, N^{3-}, F^-, H^-) offer different properties with respect to size, electronegativity, charge, orbitals and chemical bonding, we can by allowing mixing of different anions in the anionic lattice achieve new property configurations. Mixed anion lattices are considered to control *e.g.* electronic and ionic transport properties, magnetic properties, *etc*. Thus, it is great is potential to discover and understand new materials within the material class of mixed-anion compounds.

1.2 Scope of work

Oxyhydrides (section 2.5) are a relative unexplored class of mixed-anion compounds with an anionic lattice composed of oxide (O^{2-}) and hydride (H^-) anions. They often take the perovskite- or a perovskite related crystal structure and offers exotic chemistry with respect to the anionic lattice, as the strongly reducing hydride anions are rarely incorporated in combination with other anions.

Oxyhydrides are challenging to synthesize as well as their functional properties are not well studied. Based on this we foresee that the establishment of synthesis strategies that provide reproducible preparation of phase pure oxyhydrides in large quantities is a necessity. The development of such procedures is based on understanding of the target material's expected stability. We must consider the possible existence of the material in terms of the extreme reductive nature of the hydride anion in combination with possible redox active cation(s), including their somewhat limited thermal stability. Equally important, for routes based on soft-chemistry, *i.e.* by means of topotactic anion-exchange reactions, full understanding of the precursor-compounds also becomes a prerequisite.

Pure hydride anion conductivity is attractive for applications in *e.g.* solid-state metal hydride batteries. Recently, oxyhydrides received massive attention due to the report of pure hydride anion conductivity in the $La_{2-x-y}Sr_{x+y}LiH_{1-x+y}O_{3-y}$ oxyhydride system.[19] The highest observed hydride anion conductivity in the system was of 3.2×10^{-5} S cm^{-1} at 300 °C for Sr_2LiH_3O ($y = 2$). The conductivity is somewhat lower than proton conducts as the perovskite $BaScO_2(OH)$ which show a protonic conductivity of 1.7×10^{-2} S cm^{-1} at 500 °C, and the proton conducting polymer NAFION displays a higher conductivity of 7.8×10^{-2} S cm^{-1} at ambient temperatures and 100 % relative humidity.[20-21] To modify and improve functional properties of a compound, *e.g.* ionic conductivity, insight to transport and migration properties at an atomic scale is a necessity. Currently this is not at hand in the case of oxyhydrides.

With these aspects in mind, questions about the fundamental properties of materials can be addressed. This thesis aims to contribute to these topics through the following objectives:

- Investigate the unexplored halide salt flux method for synthesis of the $La_{2-x}Nd_xLiHO_3$ ($0 \leq x \leq 2$) oxyhydride system.

1. Introduction

- Study the defect situation of $LaSr_3Fe_3O_{10-x}$ and investigate the possibility to prepare an oxyhydride with this compound as precursor by topotactic anion-exchange.
- Explore thermal stability correlations of the $La_{2-x}Nd_xLiHO_3$ oxyhydrides to optimize temperature-pressure conditions for preparation of oxyhydrides.
- Describe the atomic arrangement of relevant compounds by X-ray and neutron diffraction.
- Evaluate the feasibility to use electron diffraction as an alternative probe to determine the presence of hydride anions in the La_2LiHO_3 oxyhydride.
- Utilize the combination of neutron spectroscopy and computational modelling to gain insight to the behavior of hydride anions in the La_2LiHO_3 oxyhydride with respect to ionic transport properties and chemical bonding.

2. Background

2.1 Perovskites

Perovskite is a mineral that was discovered by Gustav Rose in the Ural Mountains and named after the Russian mineralogist Count Lev Aleksevich von Petrovski.[4] The crystal structure of perovskites is related to the *perovskite* mineral, $CaTiO_3$, which is the parent phase with general formula ABX_3. In a normal perovskite A is a large cation, B is a small cation and X is an anion. The alkali, alkali earth and lanthanides are typical A-site elements, while the B-site is typically occupied by transition elements. The most common X-site anion is oxygen. Note that in the antiperovskite structure, anions occupy the A- and B-sites and cations the X-site.

The perovskite $SrTiO_3$, with space group *Pm-3m*, is commonly regarded as the archetypal cubic perovskite and will for this reason be used to illustrate the structural aspects of perovskites.[22] In crystal chemistry, we can consider the perovskite structure from both the sphere-packing approach and from the linked polyhedra approach. In the sphere-packing approach, we consider atoms as hard and non-compressible spheres. The perovskite structure is then described as built up of cubic close packed (ccp) layers of "SrO_3" with titanium occupying one quarter of the octahedral sites in a systematic manner.[3] In the linked polyhedra model, the perovskite structure is explained in terms of corner-connected TiO_6-octahedra with strontium occupying the 12-coordinated position in the middle of this network, Figure 1. The atomic coordinates for cubic $SrTiO_3$ are then $Sr(½, ½, ½)$, $Ti(0,0,0)$ and $O(½, 0, 0)$.[23]
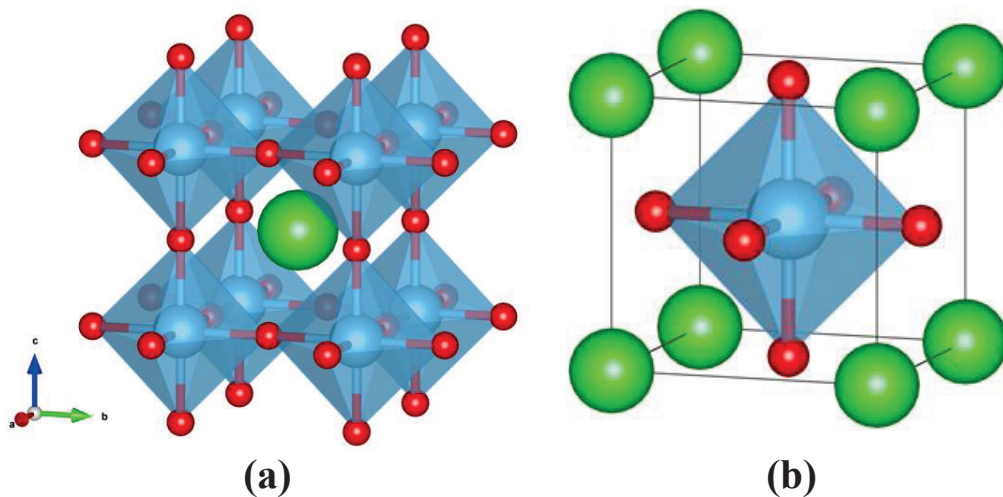

(a)   **(b)**

Figure 1: Illustration of the cubic perovskite structure of $SrTiO_3$ with space group *Pm-3m*. (a) The corner-connected octahedra, (b) cell in (a) shifted (½, ½, ½). Green atoms correspond to strontium, blue to titanium and red to oxygen.

2. Background

The perovskite class also includes compounds with symmetry deviating from the cubic one. Size effects of the atoms, stoichiometry, chemical bonding or special effects as the Jahn-Teller distortion may trig deviations from the cubic symmetry. Deviations from the cubic symmetry include distortion of the crystal structure typically in the form of tilting of the octahedra due to anion displacement, or displacement of the B-site cation or both. Goldschmidt proposed a tool for predicting the distortions of the perovskite structure based on geometric considerations of ionic radii, expressed by the following equation:[24]

$$\tau = \frac{R_A + R_X}{\sqrt{2}(R_B + R_X)}$$

Where R_A, R_B and R_X is the ionic radius of the A, B and X-atoms. For a perovskite to be cubic the tolerance factor, τ, must be close to unity, *e.g.* $SrTiO_3$ have a tolerance factor of 1.002 and adopts the cubic perovskite structure. The tolerance factor might serve as a guide to whether a compound will take the perovskite structure or not. However, it cannot predict the crystal structure or symmetry as other factors as chemical bonding also influences the picture.[22]

The $AFeO_3$ (A = Ca, Sr, Ba) perovskites nicely illustrate the influence of size effect on the symmetry of the compound. $CaFeO_3$ has a tolerance factor lower than unity. This puts compressive strain on the Fe-O bonds and tilt the octahedra so that $CaFeO_3$ takes an orthorhombic crystal structure, Figure 2 a. Lower tolerance factors will lead to greater distortions and even lower symmetry. $SrFeO_3$ has a tolerance factor close to unity and takes the cubic perovskite structure, Figure 2 b. The tolerance factor of $BaFeO_3$ is larger than unity, which places the Ti-O bonds under expansive tension. This gives hexagonal and rhombohedral crystal structures with sequences of cubic- and hexagonal close packing (ccp and hcp) of BaO_3-layers, Figure 2 c. The symmetry associated with different rotations and distortions is classified in the Glazer notation.[25]

Another aspect that makes the perovskite structure flexible is the possibility to tune oxidation states and combine cations with different charges, *i.e.* for oxides we have the combinations $A^{+I}B^{+V}O_3$, $A^{+II}B^{+IV}O_3$ and $A^{+III}B^{+III}O_3$; all possible combinations for a perovskite. In addition, double perovskites further give flexibility in terms of oxidation states and cation charges.
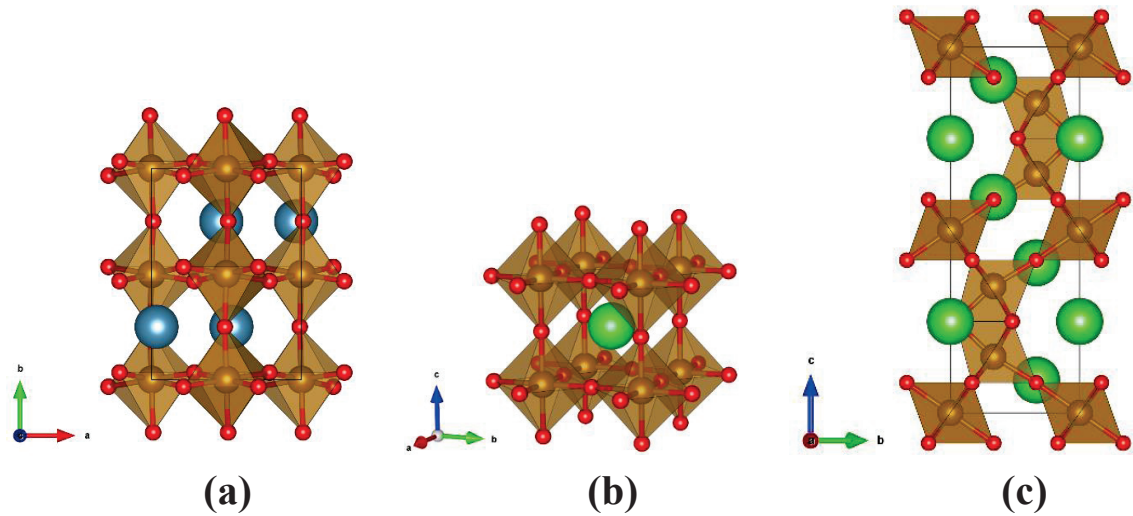
Figure 2: Illustration of the (a) CaFeO₃, (b) SrFeO₃ and (c) BaFeO₃, with space group *Pnma*, *Pm-3m* and *P6₃/mmc*, respectively. Orange-brown colored atoms correspond to iron, red to oxygen, blue to calcium and green to strontium and barium in (b) and (c), respectively.

2.2   Non-stoichiometric perovskite phases

The perovskite structure can also incorporate non-stoichiometry in the form of vacancies and interstitial atoms, still maintaining the perovskite structure. As most transition metals can take multiple oxidation states, the B-cation in a perovskite can have a partial oxidation state, *i.e.* in the reduced perovskite, $SrFeO_{2.80}$, the average oxidation state of iron is +3.6.

The $SrFeO_{3-x}$ system nicely illustrates the aspects of anion vacancies and non-stoichiometric phases for different oxygen content, Figure 3. For $x = 0$, $SrFeO_{3.0}$ adopts an ideal cubic perovskite structure. Here, iron have an oxidation state of +4, and high oxygen pressure is needed to prepare the compound.[26]

If prepared without high oxygen pressure, $SrFeO_{3-x}$ will display oxygen non-stoichiometry. When the compound is prepared, the oxygen content is controlled by temperature and oxygen partial pressure. At high temperatures the compound will contain oxygen vacancies which are randomly distributed in the crystal structure, thus cubic $SrFeO_{3-x}$ compounds are observed. Upon cooling the vacancies will order, and compounds like $Sr_8Fe_8O_{23}$ ($SrFeO_{2.875}$) and $Sr_4Fe_4O_{11}$ ($SrFeO_{2.75}$) may be formed.[26-29] If a sample do not have a stoichiometric oxygen content, a two-phase situation will occur with a mixture between the corresponding low and high oxygen content phases.[26]
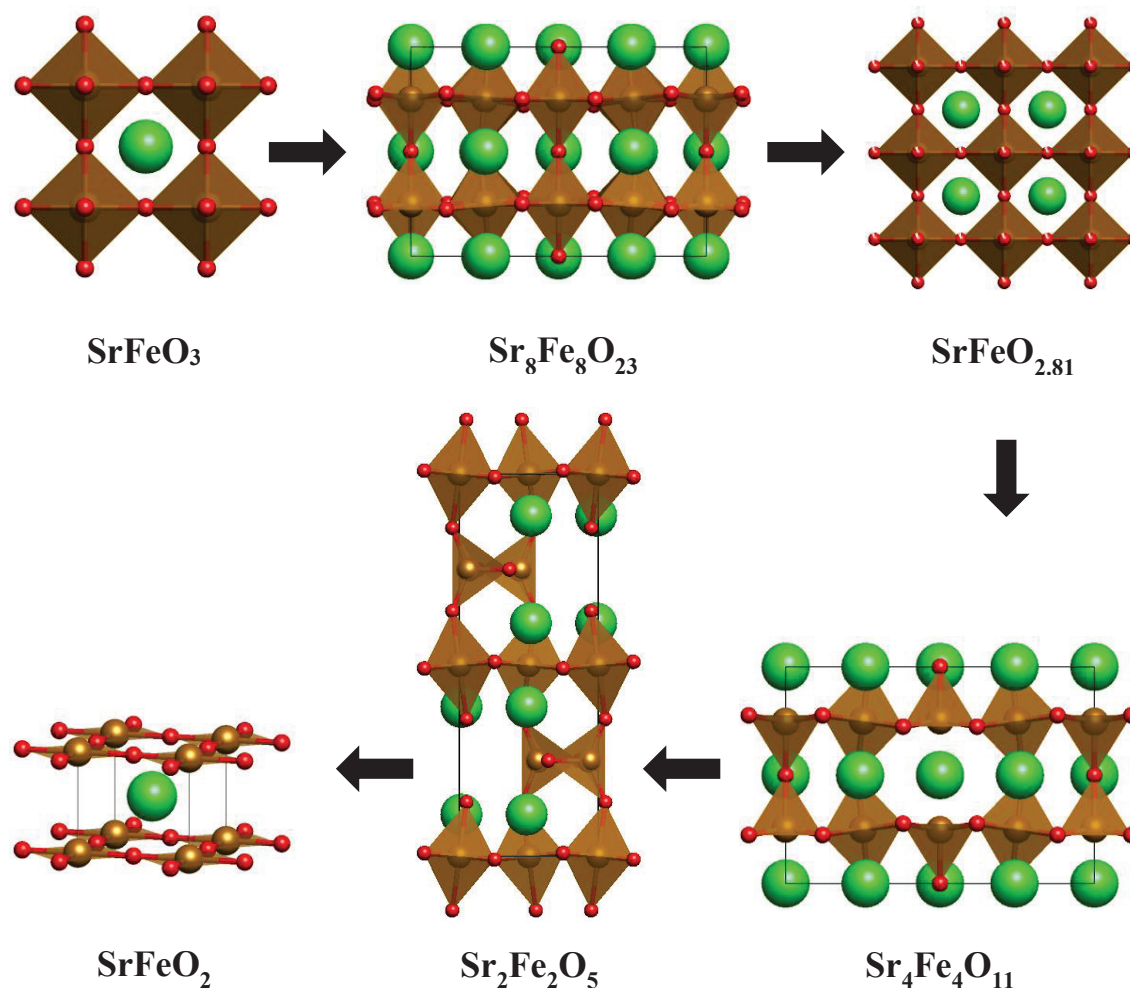
Figure 3: Illustration of possible anion deficiency / non-stoichiometry in the SrFeO$_{3-x}$ system. The arrows indicate decreasing oxygen content. SrFeO$_3$ (*Pm-3m*) without vacancies on oxygen site.[26] Vacancies can order for special compositions as Sr$_8$Fe$_8$O$_{23}$ (*I4/mmm*) and Sr$_4$Fe$_4$O$_{11}$ (*Cmmm*).[26] SrFeO$_{2.81}$ (*Fm-3c*) is not stable at room temperature, only at elevated temperatures.[29] The brownmillerite Sr$_2$Fe$_2$O$_5$ (*Ibm2*) is considered as a separate structure type from the perovskite where some of the iron atoms are tetrahedral coordinated.[30] SrFeO$_2$ (*P4/mmm*) is the most reduced compound in the SrFeO$_{3-x}$ system with square-planar coordination of the iron atoms.[31]

For $x = 0.5$, the perovskite structure is no longer kept intact, and the compound transform into a brownmillerite. The brownmillerite structure is similar to the perovskite structure (Figure 3). However, in the brownmillerite structure every second octahedral layer is exchanged by a tetrahedral layer.[30]

Reduction (removal of oxygen from the crystal structure) of a precursor compound is a well-established method to change the oxidation state of the cation in a compound and can be achieved

by several approaches, *i.e.* reduction can be achieved by heat treatment in H_2-atmosphere, reduction by metal hydride, by an oxygen getter (catcher) as NbO or Zr, or quenching from high temperature. In the $SrFeO_{3-x}$ system, $SrFeO_2$ can be formed by reduction of $SrFeO_{2.75}$ by CaH_2.[31] In this compound, iron is square-planar coordinated to oxygen, which is an unusual geometry for iron.

$LaMnO_{3+\delta}$ is another example of a non-stoichiometric perovskite, where the defect situation was for long debated. The apparent excess of oxygen was determined by neutron diffraction to in reality be A- and B-site cation vacancies.[32] In other words, the anionic lattice was not modified. Thus it is more correct to write the chemical formula $La_{1-\epsilon}Mn_{1-\epsilon}O_3$ with $\epsilon = \delta/(3+\delta)$.[33] This can be explained based on the closest packed framework of the perovskite structure. As the crystal structure is composed of closest packed layers of SrO_3, there are no space for interstitial anions. Thus, vacancies must be formed at cation position instead.

2.3   Layered perovskites

Compounds with layered crystal structure can exhibit interesting properties with respect to ion conductivity, electronic conductivity or magnetism due to effects from the dimensionality. In layered crystal structures related to the perovskite structure, an intergrowth structure is introduced by combining perovskite blocks with a second structure type. The most well-known layered perovskite families are:[22]

- Aurivillius phases: $(A_2X_2)(A_{n-1}B_nX_{3n+1})$
- Dion-Jacobsen phases: $(A)(A_{n-1}B_nX_{3n+1})$
- Ruddlesden-Popper phases: $(AX)(ABX_3)_n$

As for perovskites (Section 1.2), A is a large basic cation, B is a smaller cations and X is an anion. The Ruddlesden-Popper (RP) family is the most investigated of the three. From the general formula given above, and Figure 4, we see that the crystal structure is described in terms of *n* layers of ABX_3-perovskite blocks, separated by one-half AX-rock salt layer. Dependent on the number of perovskite blocks, we get RP1 ($n = 1$), RP2 ($n = 2$), RP3 ($n = 3$), *etc*. This imply that the RP∞-phase ($n = \infty$) corresponds to the pure perovskite structure as there is no separating rock salt layers.

In the RP-phases, there are strong chemical bonding between the layers. This is in contrast to other layered compounds as graphite and MoS_2, which have weak van der Waals bonds between the layers, making them suited as solid lubricants.[34] The bonding in RP-phases is still anisotropic due to its layered nature and the different chemical properties between the A- and B-cations.

As for the perovskite structure, a large variety of compounds takes the RP-type structure, accompanied by a broad range of functional properties. The most famous example is probably

superconductivity in cuprates. The perovskite related $YBa_2Cu_3O_{7-\delta}$ (YBCO) and the RP1 $La_{1.8}Sr_{0.2}CuO_4$ are famous for being high temperature superconductors with critical temperatures of 90 and 36 K, respectively.[13, 35]
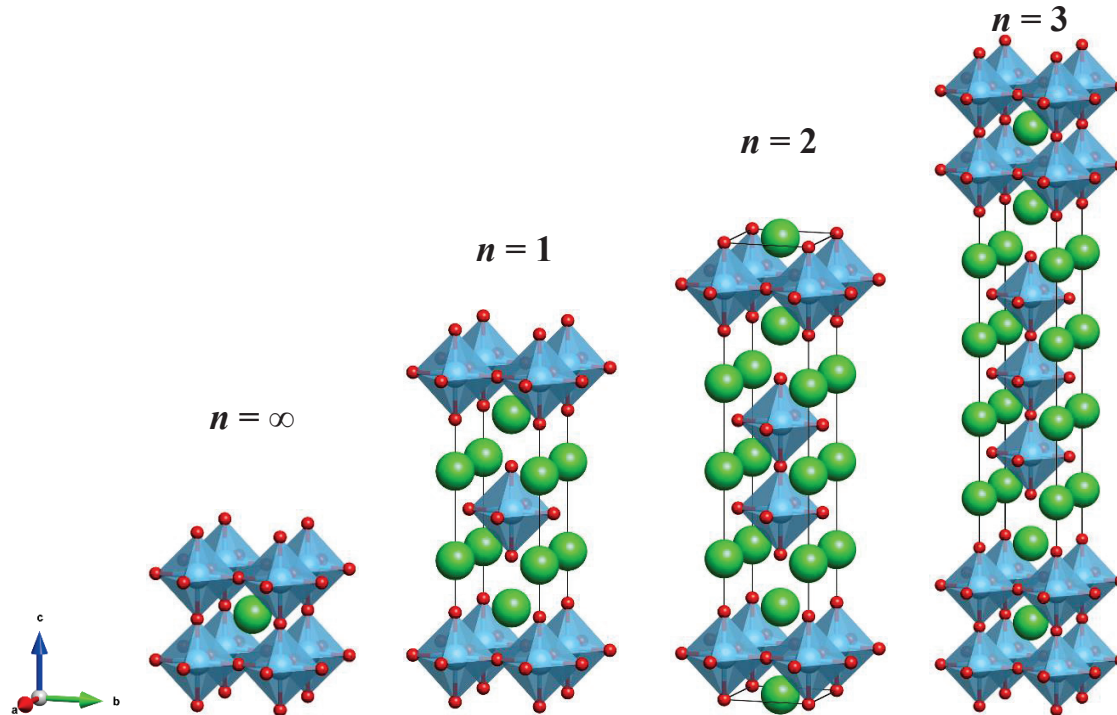

Figure 4: Illustration of the crystal structure of the Ruddlesden-Popper phases for $n = \infty$, 1, 2 and 3; exemplified by respectively $SrTiO_3$, Sr_2TiO_4, $Sr_3Ti_2O_7$ and $Sr_4Ti_3O_{10}$. $n = \infty$ correspond to the perovskite structure. Green atoms are strontium, blue atoms titanium and red oxygen.

Anion migration in perovskites is through the dominant anion defect, vacancies, as it is difficult to migrate by interstitial sites in the close-packed lattice. For PR-phases, both anion vacancies and interstitial oxygen in the empty tetrahedral sites in the rock salt layer are possible anion defects. Therefore, migration in RP-phases can either occur by migration between vacancies in the perovskite block, or as interstitial anions in the rock salt layer.[36-37] For this reason RP-phases are 2-dimensional ion conductors, showing strong anisotropy in conductivity. The RP1 phases $La_2NiO_{4+\delta}$ and $La_2CuO_{4+\delta}$ are examples of popular oxide anion conductors.[38-39] These two compounds contain an excess of oxygen situated on interstitial sites in the rock salt layer. The interstitial anion in the rock salt layer give rise to the anion conductivity in these compounds.

As for the perovskite family, a wide number of vacancies containing phases are reported. The $La_4Ni_3O_{10-\delta}$ system is one example. $La_4Ni_3O_{10}$ takes a tetragonal RP3 structure, Figure 5.[40] The related compound $La_4Ni_3O_8$ is prepared through reduction of $La_4Ni_3O_{10}$ in hydrogen atmosphere

or by reduction with zirconium.[41-42] Here, the perovskite blocks are exchanged with square-planar coordinated nickel, similarly as seen for $SrFeO_2$, though square-planar coordination is more common for nickel than for iron compounds.[31] The reduction to $La_4Ni_3O_8$ is associated with a contraction of the unit cell along the *c*-axis.

(a)   **(b)**
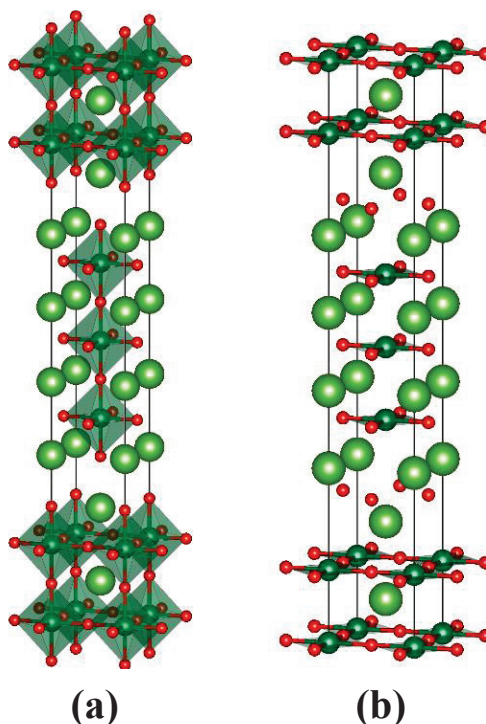
Figure 5: (a) Illustration of the crystal structure of $La_4Ni_3O_{10}$.[40] (b) Illustration of the crystal structure of $La_4Ni_3O_8$.[42-43] Green spheres correspond to lanthanum, dark green to nickel and red to oxygen.

Similarly, $LaSr_3Fe_3O_{10}$ takes a tetragonal RP3 structure.[44] When reduced to $LaSr_3Fe_3O_9$, the compound is capable to take up water to form $LaSr_3Fe_3O_8(OH)_2 \cdot xH_2O$, Figure 6.[45] The crystal structure of $LaSr_3Fe_3O_9$ is not reported in detail, although Øygarden *et al*. indexed the crystal structure to the orthorhombic space group *Bbmm* (a = 5.5479 Å, b = 5.4846, and c = 28.8846 ; standard settings, *Cmcm*, a = 28.8846 Å, b = 5.5479 Å, and c = 5.4846 Å).[45] The hydrated compound release water above 100 °C and form $LaSr_3Fe_3O_8(OH)_2$. In the hydrated and hydroxide containing compounds, crystal water and hydroxide groups are situated in the rock salt layer.
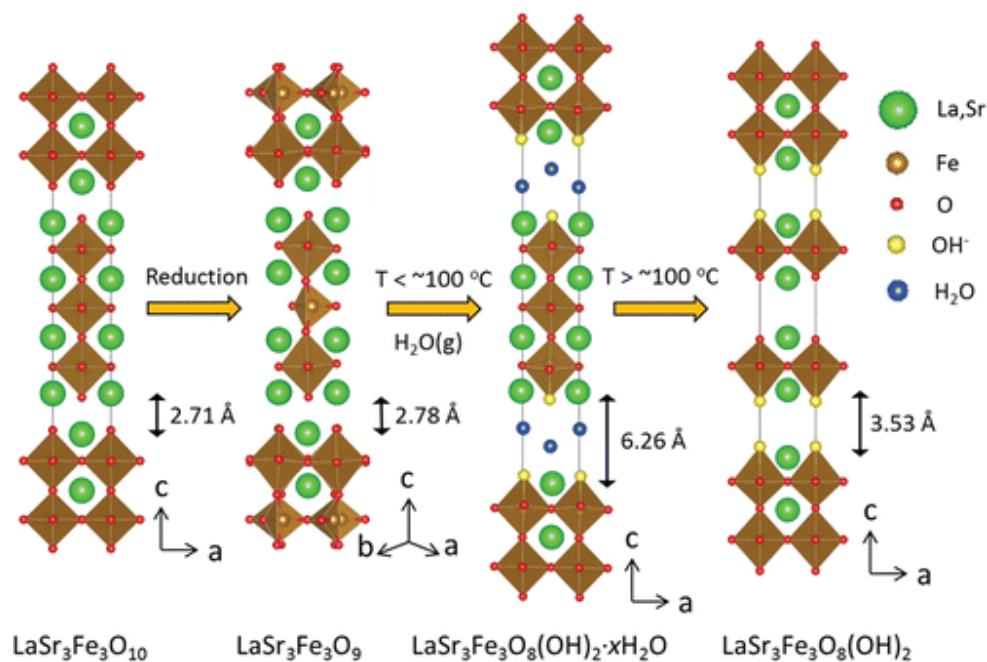
Figure 6: Schematic illustration of the different reduced and hydrated phases in the LaSr$_3$Fe$_3$O$_{10}$-system. Reused with permission from the American Chemical Society.[45]

2.4 Mixed-anion compounds

In the search for new compounds with surprising and enhanced properties, research has expanded beyond the traditional single-anion compounds, such as oxides. Compounds with multiple types of anions, such as oxynitrides (O^{2-} and N^{3-}), oxysulphides (O^{2-} and S^{2-}), oxychlorides (O^{2-} and Cl^-) and oxyfluorides (O^{2-} and F^-), supply a platform of materials where new and improved functional properties can be found.[46] The use of different anions offer various characteristics in terms of size, ionic radii, electronegativity, charge and polarizability. These characteristics influences the chemical bonding, crystal structure, electronic and magnetic interaction, which in terms give a new dimension with respect to controlling and changing the functional properties of materials. Hence, the mixed-anion compounds are a new arena to explore in contrast to more traditional single-anion compounds. Although the number of mixed-anion compounds are limited compared to *i.e.* oxides, recently they have received growing attention in the scientific community.

2.5 Oxyhydrides

Solid materials are known to contain hydrogen in the oxidation states +1, 0 and −1.[47] Most commonly, we find hydrogen as protons, H^+, *i.e.* as proton defects in ionic oxides as the proton conductors as SrZrO$_3$, and in hydroxides as NaOH. Stoichiometric and non-stoichiometric metallic hydrides are formed by all the f-block metals and the group 3, 4 and 5 from the d-block, such as TiH$_2$ and UH$_3$. These metals contain hydrogen in oxidation state zero. In addition, ionic

hydrides form when hydrogen react chemically with the most electropositive elements in compounds like LiH and CaH_2. Hydrogen in these compounds are in oxidation state -1, H^-. The hydride anion is a strong reducing agent, which limits the number of elements that can form metal hydrides. Furthermore, the combination of oxide and hydride anions in the same compound give rise to oxyhydrides.

Focus in this work is primarily on oxyhydrides. The literature within this field is limited, and even within the solid-state materials chemistry community awareness of this class of materials is modest. Therefore, we shortly review oxyhydrides in this section. Beforehand, two aspects regarding the oxyhydride nomenclature must be enlightened. Firstly, the order of the elements in the chemical formula. According to the nomenclature rules, the chemical formula starts with the cations sorted alphabetically, followed by the anions, also sorted alphabetically.[48] The latter statement imply that hydrogen should be listed prior to oxygen. However, some publications have chosen to list hydrogen after oxygen in the chemical formula, *i.e.* $BaTiO_{3-x}H_x$. In this work, such chemical formulas are modified to follow the recommended nomenclature, *i.e.* $BaTiH_xO_{3-x}$.

Secondly, we must clarify on how to write the compound names. In this thesis the term oxyhydride is used to refer to compounds containing both oxide and hydride anions. We follow this convention as this is the established term used by the community. According to the nomenclature rules, the class of compounds in question should be denoted hydride oxides to express that two anions are present, as well as the first letter in hydride ("H") is listed before first letter in oxide ("O") in the alphabet.[48]

As discussed in section 1.2, in the perovskite- and perovskite related compounds, we distinguish between the A- and the B-site cations within the formula ABX_3 as these have different chemical properties. To ensure that we recognize the A- and B-atoms from the chemical formula, in this work the order of the cations will be listed after their respective site in the perovskite ABX_3, and not alphabetically, *i.e.* here is the nomenclature based on the compound formula.

2.5.1 Overview of oxyhydrides

In this section, the literature of oxyhydrides will be shortly reviewed. Emphasis will be put on the Ln_2LiHO_3 compounds (Ln = La, Ce, Pr, Nd), which are treated in more detail at the end of this section. The number of reported oxyhydrides is limited, and in Table 1 (transition metal containing) and Table 2 (non-transition metal containing) an overview of reported oxyhydrides are listed together with key information on crystal structure, adopted synthesis routes and their potential functional properties.

2. Background

Table 1: Summary of reported transition metal oxyhydrides and their properties. Table adapted by ref.[49]

Compound	Crystal structure[a]	Synthesis[a]	Properties[a]	Hydride arrangement	Reference
$LaSrCoH_{0.7}O_3$	RP1	CaH_2	I; AFM ($T_N > 350$ K); H^- diffusion	Equatorial, ordered	50-52
$NdSrCoH_{0.80}O_{3.08}$	RP1	CaH_2	AFM ($T_N = 410$ K)	Equatorial, ordered	53
$LaSrCoH_{0.58}O_{3.21}$			AFM ($T_N = 375$ K)		
$PrSrCoH_{0.68}O_{3.16}$	RP1	CaH_2	AFM ($T_N = 445$ K)	Equatorial, ordered	53
$Sr_3Co_2H_{0.84}O_{4.33}$	RP2	CaH_2	PM	Equatorial, random	54
$ATiH_xO_{3-x}$ (A = Ca, Sr, Ba)	P	CaH_2	S-M; PM	Random	55-56
$EuTiH_xO_{3-x}$	P	CaH_2	M; FM (from Eu moments) ($T_C = 12$ K)	Random	57
$Sr_2TiD_{0.14}O_{3.91}$	RP1	CaD_2		Axial	58
$Sr_3Ti_2H_{0.12}O_{6.20}$	RP2	CaH_2		Axial [b]	58
$SrVHO_2$	P	CaH_2	I; AFM ($T_N > 300$ K)	Ordered	59
$SrV_{1-x}Ti_xH_{1.5}O_{1.5}$	P	CaH_2	I; PM	Disordered	
Sr_2VHO_3	P	CaH_2	I; AFM ($T_N = 170$ K)	Equatorial, ordered	59
$Sr_2VH_xO_{3-x}$ ($x < 0.25$)	RP1	HP		Equatorial, random	60
$Sr_2VH_xO_{3-x}$ ($x > 0.25$)				Equatorial, ordered	
$Sr_3V_2H_2O_5$	RP2	CaH_2	I; AFM ($T_N = 240$ K)	Equatorial, ordered	59
$BaVH_xO_{3-x}$ ($x = 0.3$)	P [c]	HP	M; AFM	Ordered, face-shared	61
$BaVH_xO_{3-x}$ ($x = 0.8$)	P [c]	HP	S	Random	61
$BaVH_xO_{3-x}$ ($x = 0.9$)	P	HP	S	Random	61
$SrCrHO_2$	P	HP	I; AFM ($T_N = 380$ K)	Random	
$SrCoH_yO_x$ [d]	P	CaH_2	I	Axial + equatorial, ordered	62
$NdNiH_yO_x$ [d]	CaF_2	CaH_2			63
$LaSrMnH_{0.7}O_{3.3}$	RP1	HP	I; SG ($T_N = 24$ K)	Equatorial, random	64
$BaScHO_2$	P	HP	I	Random	65
Ba_2ScHO_3	RP1	HP	H^- diffusion	Axial	66
$LaSr_3NiRuH_4O_4$	RP1	CaH_2	PM	Equatorial	67

[a] CaH_2 = topotactic anion-exchange with CaH_2, HP = high pressure, AFM = antiferromagnetism, FM = ferromagnetism, PM = paramagnetism, SG = spin glass, I = insulating, M = metallic, S = semiconducting, P = perovskite, RP1 = Ruddlesden-Popper $n = 1$, RP2 = Ruddlesden-Popper $n = 2$

[b] Only the axial position in-between (bridging) the two perovskite blocks in the RP2-type structure.

[c] 6H type perovskite

[d] Thin film

Table 2: Table of reported non-transition metal containing oxyhydrides.

Compound	Crystal structure[a]	Synthesis[a]	Properties[a]	Hydride arrangement	Reference
LaHO	CaF_2	SS		Ordered	[68]
CeHO, PrHO	CaF_2	SS		Ordered	[69]
NdHO	CaF_2	SS, CaH_2		Ordered	[70-71]
SmHO	CaF_2	SS		Random	[71-72]
GdHO GdHO:Tb^{3+}	CaF_2	SS	Luminesce	Random	[71, 73]
TbHO	CaF_2	SS		Random	[71]
DyHO	CaF_2	SS		Random	[71]
HoHO	CaF_2	SS		Random	[72]
ErHO	CaF_2	SS		Random	[71]
Ln_2LiHO_3 (Ln = La, Ce, Pr, Nd)	RP1	Flux		Equatorial, ordered	[74]
Ln_2LiHO_3 (Ln = La, Pr, Nd)	RP1	HP	H^- diffusion	Equatorial, ordered	[75]
$La_{2-x-y}Sr_{x+y}LiH_{1-x+y}O_{3-y}$	RP1	HP	H^- diffusion	Equatorial, ordered/random	[19]
$LaSrLiH_2O_2$	RP1	SS	H^- diffusion	Equatorial	[76]
Ba_3AlHO_4	aP	SS			[77]
$Ba_{21}Ge_2H_{24}O_5$ [c]	Z	SS	M		[78]
$Sr_{21}Si_2O_5H_{12+x}$ [c]	Z	SS			[79]
$Ba_{21}M_2O_5H_{12+x}$ [b, c]	Z	SS			[79]

[a] CaH_2 = topotactic anion-exchange with CaH_2, HP = high pressure, SS = solid state reaction, I = insulating, RP1 = Ruddlesden-Popper n = 1, CaF_2 = fluorite structure, aP = antiperovskite, Z = Zintl phase

[b] M = Zn, Cd, Hg, In, Tl, Si, Ge, Sn, Pb, As, Sb, Bi

[c] As these oxyhydrides do not take a perovskite or perovskite related structure they are not further discussed in this work.

Brice and co-workers reported the first oxyhydride, LaHO, in 1982.[68-69] LaHO is a typical example of an oxyhydride with respect to chemical composition. In addition to the mandatory hydrogen and oxygen anions, the compound contains lanthanum, which is a large basic redox-inactive cation. Commonly, oxyhydrides contain a lanthanide or an alkali/alkali earth element, possibly a transition metal in combination with the oxide- and hydride anions; see Table 1 and Table 2. The crystal structure of LaHO is derived from the cubic CaF_2-structure. Due to ordering of the anionic lattice the compound is described as a tetragonal CaF_2 superstructure crystallizing in space group *P4/nmm*. Lanthanum has three different coordination environments depending on the ordering of the anions in the cube coordination polyhedra, Figure 7.
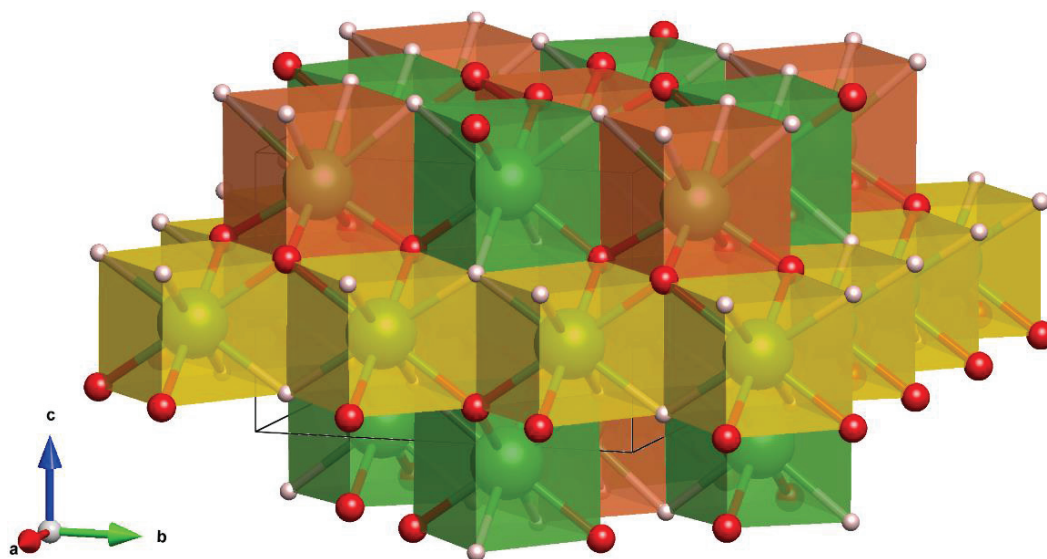
Figure 7: Schematic illustration of the crystal structure of LaHO (space group *P4/nmm*). The green, red and white atoms are lanthanum, oxygen and hydrogen, respectively. The different colors of the cube coordination polyhedra of lanthanum represent the three different surroundings of lanthanum dependent on the ordering of the oxygen and hydrogen atoms.

*Ln*HO oxyhydrides have also been prepared for cerium (Ce), praseodymium (Pr), neodymium (Nd), samarium (Sm), gadolinium (Gd), terbium (Tb), dysprosium (Dy), holmium (Ho) and erbium (Er).[68-71, 73] Lanthanides smaller than neodymium adopts a cubic crystal structure with space group *Fm-3m*, in contrast to the other reported lanthanide oxyhydrides. The reason for this is that the oxide- and hydride anions create a disordered anionic lattice, while in the tetragonal crystal structure the anions are ordered. The driving force for the anion order-disorder transition is attributed to the oxide anions being "under-bonded" (to little positive charge surrounding the anions) for large lanthanides, thus the anions order to form shorter lanthanide-oxygen bonds and longer lanthanide-hydrogen bonds, as illustrated in Figure 8.[71]
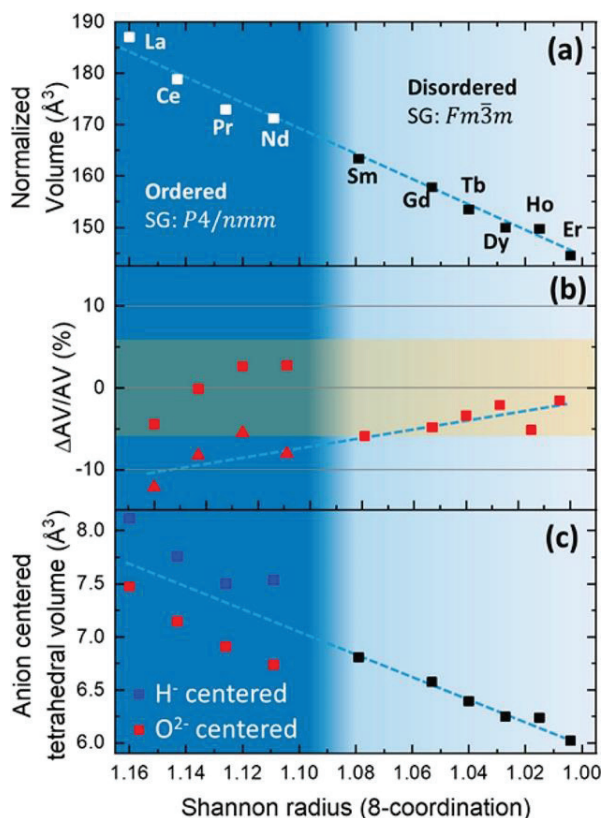
Figure 8: (a) Normalized unit cell volume for the *Ln*HO oxyhydrides as a function of the Shannon radii of the lanthanide cation.[80] (b) Deviation from the ideal valance illustrated as ΔAV/AV (AV refers to apparent valence from bond valence sum calculations) for the oxide anions. The symbols (■) and (▲) illustrate values obtained from the refined structural model and a hypothetical disordered model, respectively. (c) Anion-centered tetrahedral volume around the oxide and hydride anions for the disordered model (black symbols), red and blue symbols refer to oxide and hydride respectively, in the ordered phase. Reused with permission from American Chemical Society.[71]

According to Table 1 and Table 2, a majority of the reported oxyhydrides adopts a perovskite or a RP-type crystal structure. The large compositional flexibility of the perovskite and perovskite related crystal structures are evident. Seemingly, in the perovskites the hydride anions are randomly distributed in the BX_6-octahedra as illustrated by $SrCrHO_2$ in Figure 9 a. In the RP-type structures, the hydride anions prefer to occupy the equatorial sites (basal-plane), Figure 9 b. This observation be attributed bonding situation for the two sites. As seen in Figure 9 b, the axial position in the octahedra in the RP-type structures are bonded to five A atoms and one B atoms, while the equatorial position is bonded to four A atoms and two B atoms. As the A-site cations are more basic, the oxide anions prefer this site due to their higher charge compared to the hydride anions. Ordering of oxide- and hydride anions between the equatorial positions in the RP-type structures is also common, this can be assigned to size effects or the presence of vacancies.
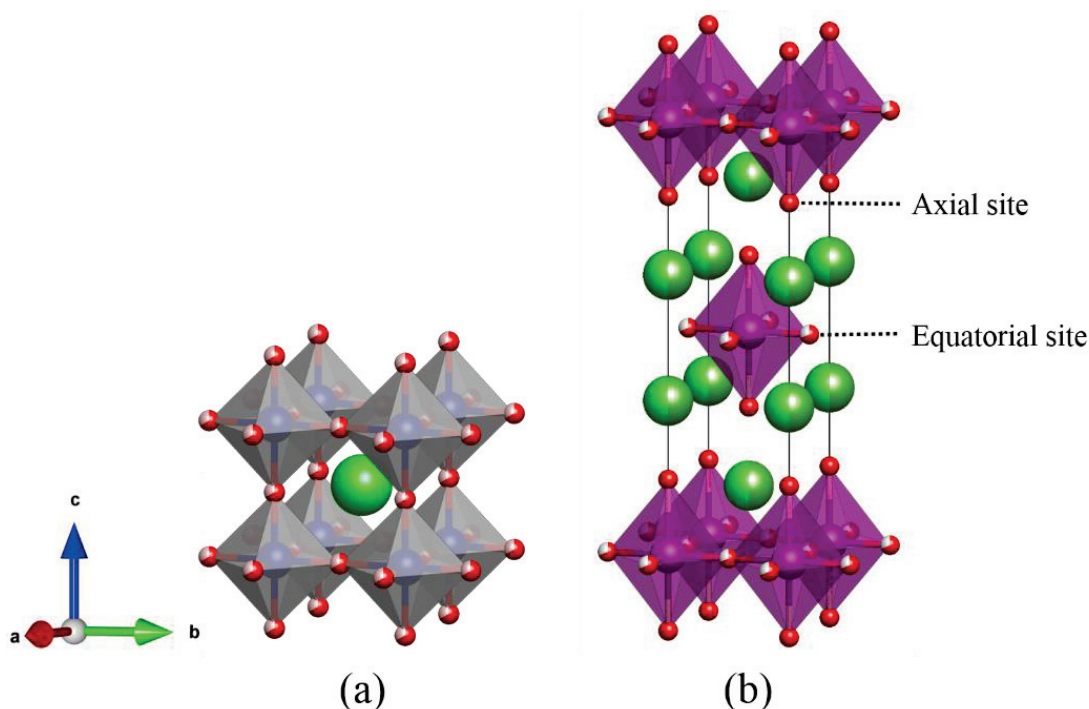
17

Figure 9: Crystal structure of cubic (*Pm-3m*) SrCrHO$_2$ (a) and tetragonal (*I4/mmm*) LaSrCrH$_{0.7}$O$_{3.3}$ (b).[64, 81] In SrCrHO$_2$ (a) the oxide and hydride anions are randomly distributed, while in LaSrCrH$_{0.7}$O$_{3.3}$ (b), the oxide and hydride anions are randomly distributed in the equatorial plane of the octahedra. The axial position in the octahedra is occupied by oxygen. Green atoms correspond to strontium in (a), and strontium and lanthanum in (b) and (c), blue to chromium, purple to manganese, white to hydrogen and red to oxygen.

The majority of the transition metal containing oxyhydrides, Table 1, display antiferromagnetic properties. This is not surprising as most oxides also are antiferromagnetic, and the bonding situation in oxyhydrides and oxides are similar. The RP1-type oxyhydride LaSrMnH$_{0.7}$O$_{3.3}$ demonstrate spin-glass behavior, assigned to competing ferro- and antiferromagnetic interaction due to the mixed valance state of manganese.[64] The only ferromagnetic oxyhydride is EuTiH$_x$O$_{3-x}$. However, in this case it is the europium cations that order ferromagnetic, and not the transition metal.[57]

LaSrCoH$_{0.7}$O$_3$, first reported by Hayward *et al*. in 2002 is an oxyhydride adopting the RP1-type crystal structure.[50-51, 82] The oxide and hydride anions in the transition metal oxyhydride is ordered, making arrays of oxide and hydride anions in the equatorial plane of the coordination polyhedra of cobalt.[50] The compound is antiferromagnetic ordered to at least 350 K. The high Neel temperature (T$_N$) demonstrates that the hydride anions and transition metal cations can have strong

electronic coupling. Seemingly, the *1s* orbital of the hydride anions give unusual bonding and electronic/magnetic interactions, which can be used to influence their functional properties.

In addition to the interesting chemistry and magnetic properties of $LaSrCoH_{0.7}O_3$, hydride anion diffusion was also observed in this material.[52] Diffusion was proved by Quasi-Elastic Neutron Scattering (QENS), see section 3.2.3.1. As hydrogen is a strong incoherent scatterer, QENS can probe the diffusion of the hydride anions in the crystal structure. The activation barrier for hydride migration was determined to be 0.23 ± 0.045 eV and the hydride anions where found to jump along the hydride anion arrays in the crystal structure. The onset of the hydride mobility was concluded to be at 675 K, which is the temperature where the broadening of the QENS signal take place, Figure 10.
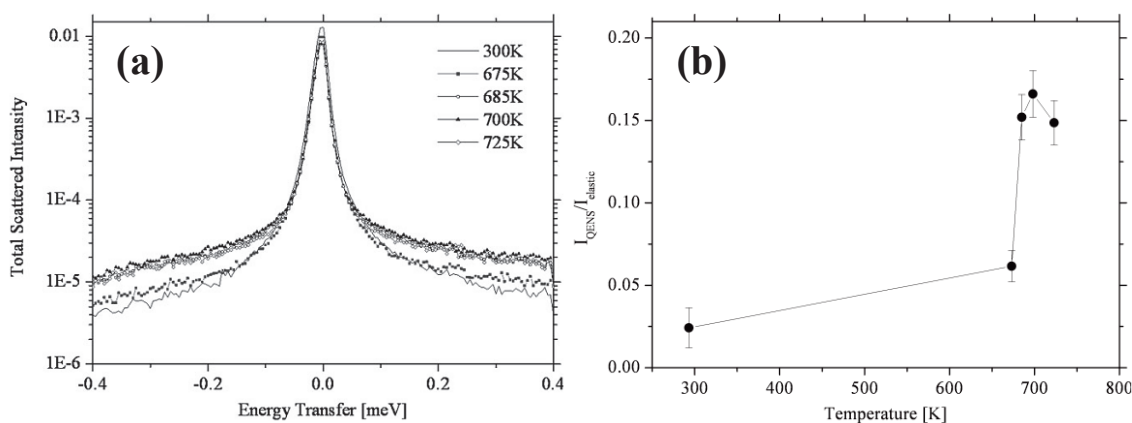

Figure 10: (a) Q-averaged QENS spectra as a function of sample temperature for $LaSrCoH_{0.7}O_3$. The increased broadening above 675 K indicates the onset of hydride mobility. (b) Ratio of the intensity of quasi-elastic scattering to elastic scattering ($I_{QENS}/I_{elastic}$) as a function of temperature. Reused with permission from John Wiley and Sons.[52]

$BaScHO_2$ and Ba_2ScHO_3 are hydride anion conducting oxyhydrides which takes a perovskite and RP1-type crystal structure, respectively.[65-66] Although the compositions are very similar, Ba_2ScHO_3 exhibit an ionic conductivity of 5.2×10^{-6} S cm^{-1} compared to $\sim 7 \times 10^{-8}$ S cm^{-1} for $BaScHO_2$. The difference is ascribed to the diffusion mechanism; in $BaScHO_2$ the hydride anions move in the perovskite layer, while in Ba_2ScHO_3, the hydride anions are situated on the axial site in the octahedral surrounding scandium. Therefore the hydride anion can migrate into and within the rock salt layer. There the hydride anion can move by empty tetrahedral sites which yields lower activation energy than migration in the perovskite layer.

The perovskite $BaTiH_xO_{3-x}$ oxyhydride is thoroughly investigated, after Kobayashi *et al.* demonstrated exchange of hydrogen/deuterium at 400 °C, indicating that the compound conduct hydride anions.[56] Crystal structure investigations by X-ray and neutron diffraction revealed that

the anion positions were fully occupied with oxide and hydride anion, not containing vacancies. The compound adopts a disordered perovskite crystal structure and show complete solid solution in the $ATiH_xO_{3-x}$ (A = Ca, Sr, Ba; $x = 0.1-0.3$) system.[55]

Nedumkandathil *et al*. further investigated aspects of synthesis of the $BaTiH_xO_{3-x}$ system.[83] They established by nuclear magnetic resonance (NMR), that the samples they had prepared contained vacancies. This observation is in contrast to the finding of Kobayashi *et al*. They also concluded that the reduction with different metal hydrides gave different amounts of hydride anions and vacancies in the crystal structure, Table 3.

Table 3: Composition of $BaTiH_yO_{3-x}\square_{x-y}$ ($\square$ symbolizes vacancies) oxyhydrides from reduction with different metal hydrides. x_H refers to the reaction $BaTiH_xO_{3-x} + 0.75xO_2 \rightarrow BaTiO_3 + 0.5xH_2O$, and $x_\square$ refers to the reaction $BaTiO_{3-x} + 0.5xO_2 \rightarrow BaTiO_3$. Reused with permission from American Chemical Society.[83]

Metal hydride	x_H from TG	$x_\square$ from TG	y from NMR	Composition
CaH_2	0.24	0.23	0.16	$BaTiH_{0.16}O_{3.76}\square_{0.08}$
MgH_2	0.41	0.39	0.14	$BaTiH_{0.14}O_{3.60}\square_{0.26}$
$NaAlH_4$	0.39	0.37	0.15	$BaTiH_{0.15}O_{3.62}\square_{0.23}$
$NaBH_4$	0.36	0.34	0.04	$BaTiH_{0.04}O_{3.65}\square_{0.31}$

The $BaTiH_xO_{3-x}$ oxyhydride has also been investigated by computational methods. It is demonstrated by density functional theory (DFT) that hydride ions are solely stabilized at vacant oxygen sites in the perovskite structure in the form of hydride anions.[84-85] The diffusion mechanism is stated to be oxygen-vacancy mediated, thus the hydride anions migrate by the anion sites in the perovskite structure. The activation energy for migration along this path was calculated to be 0.28 eV.[85]

QENS also gave experimental insight to the migration pathways of hydride anions in the $BaTiH_xO_{3-x}$ system.[86] At low temperatures ($\leq$ 250 K) the hydride anion were found to move by the nearest neighbor anion sites as found by DFT, while at higher temperatures (> 400 K) the anions moved by the next-nearest neighbor sites, Figure 11. The diffusion constant D was about 0.4×10^{-6} cm^{-2} s^{-1} at 225 K, and between 20×10^{-6} and 100×10^{-6} cm^{-2} s^{-1} at temperatures between 400 and 700 K. An activation energy of about 0.1 eV was determined from the QENS analysis.

These observations are further supported by Tang *et al*., which by deuterium exchange investigated the hydride diffusion in $BaTiH_xO_{3-x}$ and $LaSrCoH_{0.7}O_3$.[87] For low hydride content ($x < 0.4$), the hydride diffusion is by the nearest neighbor sites. Thus, oxygen is limiting the diffusion. For higher hydride content, the hydride anions migrate by the next-nearest neighbor sites as Bridges *et al*. reported that this the case for $LaSrCoH_{0.7}O_3$.[52] Tang *et al*. observed the same behavior for $LaSrCoH_{0.7}O_3$.[87]
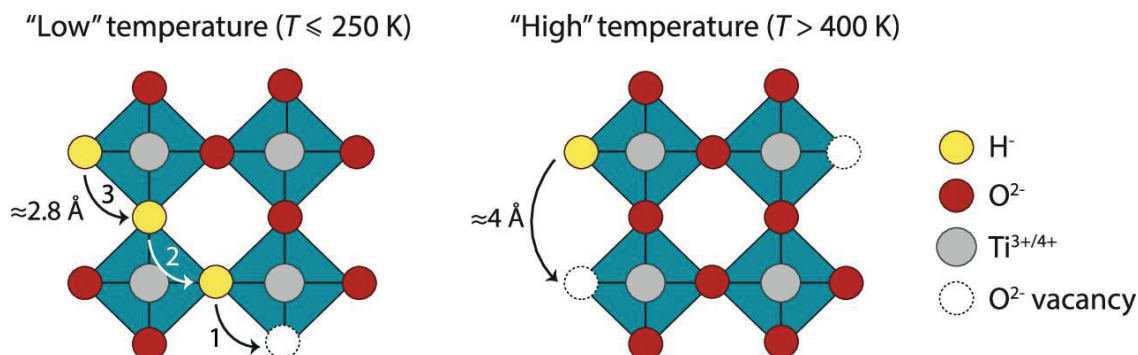
Figure 11: Schematic illustration of the observed migration paths from the hydride anion at low (≤ 250 K) and high (> 400 K) temperatures by QENS. Reused with permission from American Chemical Society.[86]

Takeiri *et al*. observed that scandium substitution in $SrTiH_xO_{3-x}$ improved the diffusion properties of the compound.[88] Aliovalent substitution on the B-site intrude vacancies in the anionic lattice. As oxygen diffusion is limiting the migration of hydride anions by the nearest neighbor site, this approach promote diffusion of both oxide and hydride anions.

Liu *et al*. used isotope-exchange and depth profiling combined with computational methods to investigate the correlation between diffusion of oxide and hydride anions in $BaTiH_xO_{3-x}$ thin films.[89] They developed methodology for calculating the correlation factors, showing that that migration of hydride anions to neighboring vacant sites is fast, however, long-range transport is impeded by the slow reorganization of the oxygen sublattice. Thus, to achieve high hydride anion conductivity in oxyhydrides, fast oxygen dynamics is a necessity, or systems where hydrogen can migrate without obstacles must be chosen.

The electronic conductivity is influenced by hydride anion incorporation in $BaTiH_xO_{3-x}$ oxyhydrides.[56] $BaTiO_3$ is an insulator, while $BaTiH_xO_{3-x}$ exhibit semiconducting and metallic conductivity depending on the hydride anion content.[56] This can be attributed to the fact that the hydride anions are positive defects in the oxide anion lattice. The positive hydride anion defects are charge compensated by electrons, thus reducing some of the Ti^{+4} cations to Ti^{+3}, giving rise to the electronic conductivity. The redox chemistry of $BaTiH_xO_{3-x}$ might also be the reason the oxyhydride recently have received attention as catalyst for production of ammonia and CO_2 methanation.[71, 90-91]

2.5.1.1 The *Ln*₂LiHO₃ oxyhydrides (*Ln* = La, Ce, Pr, Nd)

Schwarz is the first to report on the Ln_2LiHO_3 (*Ln* = La, Ce, Pr and Nd) oxyhydrides in his PhD thesis in 1991.[74] By the means of neutron diffraction, he describes the La_2LiHO_3 oxyhydride to take an orthorhombic (*Immm*) RP1-type crystal structure, Figure 12. Lithium occupy the B-site in the perovskite block and has an octahedral coordination of oxide and hydride anions. The oxide

and hydride anions are ordered so that the hydride anions occupy the equatorial positions along the a-axis in the octahedra, while the oxide anions occupy the equatorial positions along the b-axis and the axial positions. He prepared the compounds from a lithium chloride halide-flux. La_2LiHO_3 was only prepared phase pure by synthesis at 750 °C for 2 days with a 1:4 ratio of La_2O_3:LiH. Ce_2LiHO_3 was only prepared phase pure at 700°C, while the other investigated lanthanides gave a mixture between the oxyhydride and the corresponding oxide, Ln_2O_3.
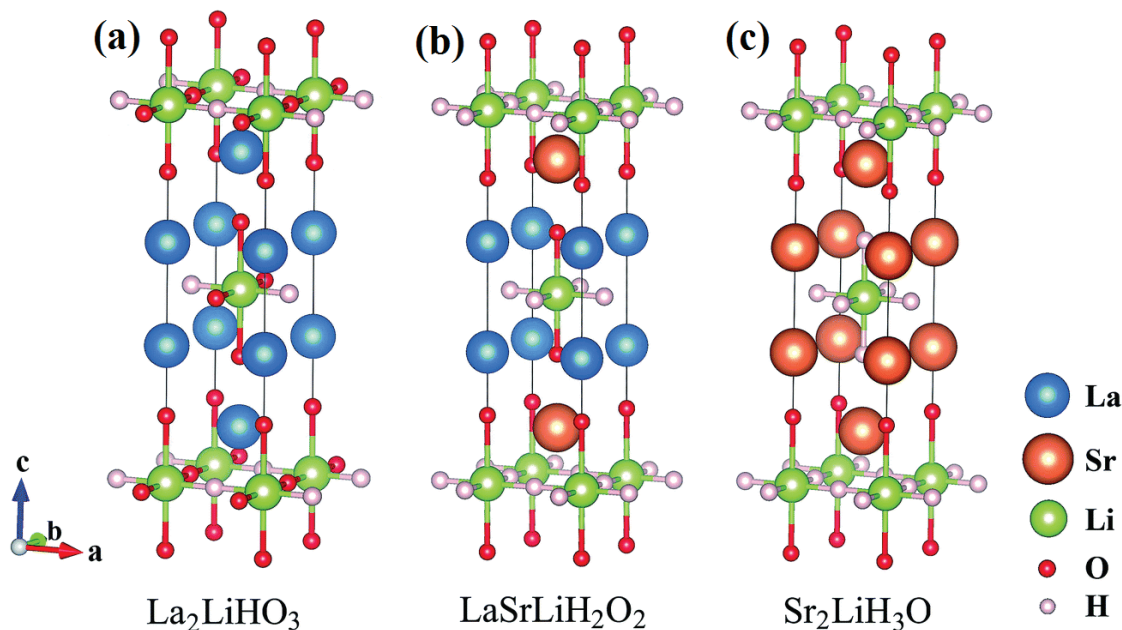

Figure 12: Schematic illustration of the relaxed RP1-type crystal structure of orthorhombic (*Immm*) La_2LiHO_3 (a), tetragonal (*I4/mmm*) $LaSrLiH_2O_2$ and tetragonal (*I4/mmm*) Sr_2LiH_3O from DFT calculations.[92] Lanthanum, lithium, oxygen and hydrogen atoms are drawn with blue, green, red and white spheres, respectively. Reused with permission from Royal Society of Chemistry.[92]

More recently, Kobayashi *et al*. reported two polymorphs of La_2LiHO_3, one orthorhombic (space group *Immm*) and one tetragonal (space group *I4/mmm*) in the $La_{2-x-y}Sr_{x+y}LiH_{1-x+y}O_{3-y}$ oxyhydride system.[19] However, the tetragonal variant contained anion vacancies, giving the formula $La_2Li(H_{0.53}O_{1.21}\square_{0.26})O_2$ ($\square$ symbolizes vacancies). The orthorhombic compound is reported to be stoichiometric based on Rietveld refinements of neutron diffraction data. Compositions of the different investigated compounds in $La_{2-x-y}Sr_{x+y}LiH_{1-x+y}O_{3-y}$ system are given in Table 4. An excess of 100 molar % lithium hydride was used in the synthesis to compensate for loss of light elements (lithium and hydrogen) during synthesis. The crystal structure of $La_{2-y}Sr_yLiH_{1+y}O_{3-y}$ ($y = 0, 1, 2$) are shown in Figure 12.

Table 4: Reported compositions for $La_{2-x-y}Sr_{x+y}LiH_{1-x+y}O_{3-y}$ synthesized by the high pressure and solid-state reaction at ambient pressure (marked with an asterisk).[19, 76] o-La_2LiHO_3 denotes the orthorhombic crystal structure and t-La_2LiHO_3 denotes the tetragonal crystal structure.

o-La_2LiHO_3	t-La_2LiHO_3	$LaSrLiH_2O_2$	Sr_2LiH_3O
La_2LiHO_3	$La_2Li_{0.999}H_{0.5256}O_{3.2056}$	$LaSrLi_{0.96}H_{1.9}O_2$	$Sr_{1.994}LiH_{2.9416}O_{1.0585}$
	Vacancies = 0.2688	$La_{1.138}Sr_{0.862}LiH_{1.864}O_{2.136}$*	

The $La_{2-x-y}Sr_{x+y}LiH_{1-x+y}O_{3-y}$ oxyhydride system further received massive attention due to the observation of pure hydride anion conductivity in the compound.[19] This finding emphasizes the possible technological applications of oxyhydrides. To provide conclusive evidence of pure hydride anion conductivity, they assembled a solid-state battery with metallic titanium and titanium hydride as electrodes, separated by an electrolyte of La_2LiHO_3, Figure 13. When discharged, formation of titanium hydride at titanium electrode was observed, thus proving that the compound conduct hydride anions. The tetragonal variant show slightly higher hydride anion conductivity, 3.6×10^{-6} S cm^{-1}, than for the orthorhombic polymorph, 5.2×10^{-6} S cm^{-1}, at 300 °C.
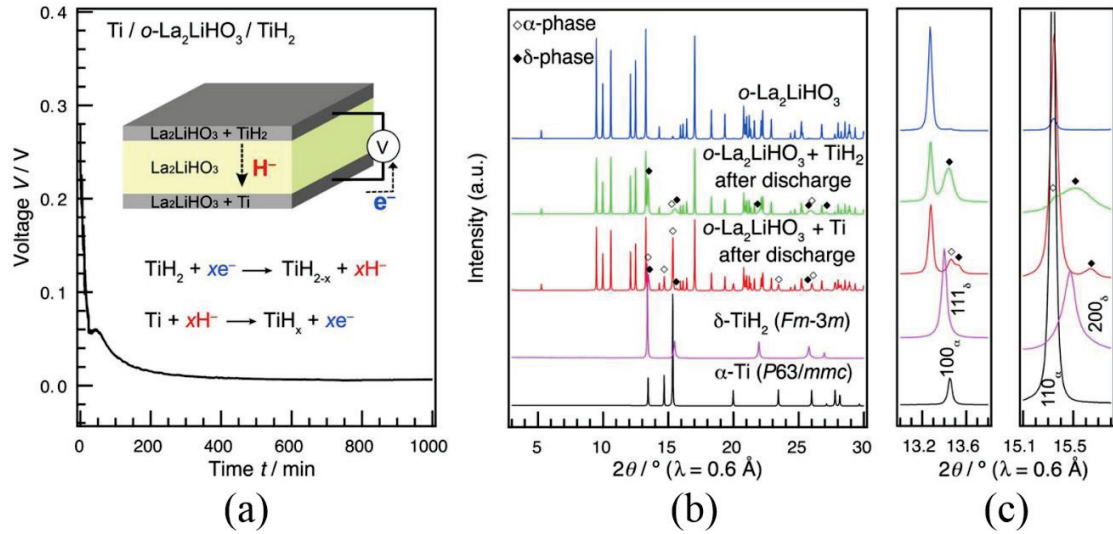
Figure 13: (a) Discharge curve for a solid-state battery with the Ti/o-La_2LiHO_3/TiH$_2$. The inset illustrates the arrangement of the cell and the proposed electrochemical reaction. (b) X-ray diffraction patterns for the electrolyte (o-La_2LiHO_3), cathode (TiH$_2$ + o-La_2LiHO_3), and anode (Ti + o-La_2LiHO_3) after the reaction. (c) Magnifications for ranges 13° to 13.8° and 15.1° to 15.8°. Reused with permission from The American Association for the Advancement of Science.[19]

Ln_2LiHO_3 (Ln = La, Pr, Nd) was also synthesized by Iwasaki *et al*. by high-pressures at 650 °C and 2 GPa.[75] Preparation of the corresponding samarium oxyhydride was unsuccessfully attempted. A small fraction (3−5 %) of mixing between the equatorial oxide and hydride anions

for the praseodymium and neodymium oxyhydrides were observed and from refinements of neutron diffraction the composition was determined to be $Pr_{1.99}LiH_{1.01}O_{2.99}$ and $Nd_{1.98}LiH_{1.04}O_{2.95}$. The neodymium oxyhydride showed highest conductivity, 2.2×10^{-5} S cm^{-1} at 280 °C and suggest that the mixed-anion situation in the compound facilitate diffusion.

Watanabe *et al.* synthesized the similar oxyhydride $LaSrLiH_2O_2$ by a solid-state reaction at 650 °C in H$_2$-atmosphere.[76] Also in this case a lithium hydride excess of 100 mass % was needed to circumvent impurities in the product. The compound was reported to have a composition of $La_{1.138}Sr_{0.862}LiH_{1.864}O_{2.136}$ from Rietveld refinements of neutron diffraction data and an ionic conductivity of 3.2×10^{-6} S cm^{-1} at 300 °C was measured.

Liu *et al.* investigated the migration of hydride anions in La_2LiHO_3, $LaSrLiH_2O_2$ and Sr_2LiH_3O by DFT. They found that anion vacancies was most likely to be found at the equatorial anion positions in the LiX$_6$ octahedra (X = O^{2-} and H$^-$).[92] The hydride anions were concluded to migrate by the equatorial sites and the migration enthalpies varied from 0.21 to 0.45 eV depending on the composition. Furthermore, they reported the hydride anion diffusion in La_2LiHO_3 to be limited by the slow oxide anion migration.

Bai *et al.* also investigated the $La_{2-x-y}Sr_{x+y}LiH_{1-x+y}O_{3-y}$ system by DFT and *ab initio* molecular dynamics simulations (AIMD).[93] They observed the presence of covalent bonding in La_2LiHO_3 and $LaSrLiH_2O_2$ without commenting it further. Only negligible diffusion of hydride anions was observed in the calculations in absence of hydride anion vacancies for La_2LiHO_3, $LaSrLiH_2O_2$, and Sr_2LiH_3O. Further, hydride anion diffusion, mediated by vacancies, in La_2LiHO_3 was not observed within the time scale of the AIMD calculations, being blocked by the oxide anions. Oxyhydrides with hydride anions in the equatorial plane stated to show 2D hydride anion migration. In oxyhydrides with hydride anion on the axial position, *i.e.* oxyhydrides with higher hydride anion content than $LaSrLiH_2O_2$ as Sr_2LiH_3O, may show 3D hydride anion migration. However, the migration along the *c*-axis show one order of magnitude lower conductivity than hydride migration in the *ab*-plane.

2.5.2 Synthesis of oxyhydrides

To this point, several oxyhydrides is described, and several approaches is used to prepare these compounds. Either ceramic methods (with or without high pressure), topotactic anion-exchange with a metal hydride or a halide salt flux method. In this section, the different synthesis methods will be discussed in light of synthesis of oxyhydrides.

The ceramic method is a well-known synthesis route in solid-state chemistry.[94] By this approach, solid components reacts at high temperatures to form a product. The method has two main challenges, nucleation and diffusion. Nucleation refers to the initial formation of the desired product having correct chemical composition and atomic arrangement. This may be a limiting

factor for formation process. This step can be facilitated if there is a structural similarity between the product and one of the reactants. Diffusion can also be a challenge, as in a solid-state reaction the components must diffuse into each other to form the product. To overcome the challenges associated with diffusion, the diffusion path lengths can be reduced by reducing the particle size of the components. Further, high temperatures facilitate mobility and is therefore commonly used in ceramic synthesis. For oxyhydride synthesis, high temperatures is a possible issue as metal hydride components are often unstable at high temperatures, and only a few oxyhydrides is reported by this method.

High pressures synthesis (1–5 GPa) have become increasingly popular to prepare oxyhydrides and are widely used to stabilize the oxyhydride.[19, 64, 81] Similar to the ceramic method, the high-pressure method is a solid-solid reaction, but with high mechanical pressure applied (typical 1–10 GPa). High pressures may significantly affect the equilibria for reactions, allowing formation of metastable phases.[95] The method stabilize the densest atomic arrangement and prevent the metal hydrides and oxyhydrides phases from decomposing, allowing the oxyhydrides to be formed by a solid-solid reaction. For this reason, high pressures are much used for preparation of novel oxyhydrides. Typical reaction temperatures are 650-1000 °C.[19, 64, 81] Drawbacks with this method is that only small sample quantities (typically a few hundred mg) are produced in each batch, and the need for high-pressure instrumentation. Typical a surplus of metal hydride is used due to loss through evaporation of light elements (hydrogen, lithium, *etc.*) in synthesis.

In terms of oxyhydride synthesis, a solid-state reaction is here exemplified by the reaction between SrH_2, SrO and Cr_2O_3, to form the oxyhydride $SrCrHO_2$.[81] A balanced equation for the reaction is given below.

$$SrH_2(s) + SrO(s) + Cr_2O_3(s) \rightarrow 2\, SrCrHO_2(s)$$
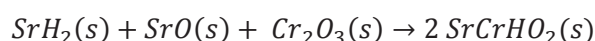
The reaction was carried out at 5 GPa at 1000 °C. Thus, this reaction emphasizes the importance of high pressures to stabilize the components during synthesis. The decomposition temperature of strontium hydride is around 1000 °C, and metal hydrides commonly release some hydrogen during heating.[96] Additionally, oxyhydrides typically have low decomposition temperatures. Without high pressures, it is likely that strontium hydride or the oxyhydride $SrCrHO_2$ would decompose.

Topotactic anion-exchange is another common method for preparation of oxyhydrides. This method is another variant of the ceramic method, where a metal hydride is used to exchange oxide anions with hydride anions in a precursor compound. As the precursor have similar atomic arrangement as the oxyhydride product, the nucleation step is circumvented. Synthesis with the topotactic anion-exchange method is typically carried out at 400–600 °C, lower than temperatures used in high-pressure synthesis.[50, 56, 67] For this reason, the method is considered quite mild. By

keeping the temperature sufficiently low, "over-reduction" to binary oxides and metals is avoided. A drawback with the topotactic anion-exchange method is that this method also is limited by diffusion to form oxyhydrides. Additionally, CaO and surplus of CaH_2 must be washed away after synthesis. Further, redox active cations must typically be present in the sample to form oxyhydrides as reduction is a reaction step in the topotactic anion-exchange method (see below).

The reaction path for formation of $LaSrCoH_{0.7}O_3$ is studied in detail and serve well as an example for the topotactic anion-exchange method.[51] The proposed reaction steps are given below. First (step a in the equation), the precursor compound is reduced to a vacancy-containing compound. This enhances anion diffusion through the lattice due to presence of anion vacancies. In step b, both oxide and hydride anions diffuse through the lattice. As the precursor compound $LaSrCoO_4$ is tetragonal, while the product is orthorhombic, both a tetragonal ($LaSrCoH_yO_{3.38-x}$) 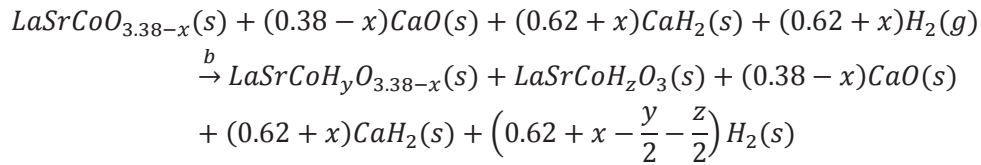and an orthorhombic ($LaSrCoH_zO_3$) phase is present in this step. In the last step, c, the desired oxyhydride is formed.

Step a:

$$LaSrCoO_4(s) + CaH_2(s) \xrightarrow{a} LaSrCoO_{3.38-x}(s) + (0.38 - x)CaO(s) + (0.62 + x)CaH_2(s)$$
$$+ (0.62 + x)H_2(g)$$

Step b:

$$LaSrCoO_{3.38-x}(s) + (0.38 - x)CaO(s) + (0.62 + x)CaH_2(s) + (0.62 + x)H_2(g)$$
$$\xrightarrow{b} LaSrCoH_yO_{3.38-x}(s) + LaSrCoH_zO_3(s) + (0.38 - x)CaO(s)$$
$$+ (0.62 + x)CaH_2(s) + \left(0.62 + x - \frac{y}{2} - \frac{z}{2}\right)H_2(s)$$

Step c:

$$LaSrCoH_yO_{3.38-x}(s) + LaSrCoH_zO_3(s) + (0.38 - x)CaO(s) + (0.62 + x)CaH_2(s)$$
$$+ \left(0.62 + x - \frac{y}{2} - \frac{z}{2}\right)H_2(g) \xrightarrow{c} LaSrCoH_{0.7}O_3(s) + CaO(s) + 0.65H_2(g)$$
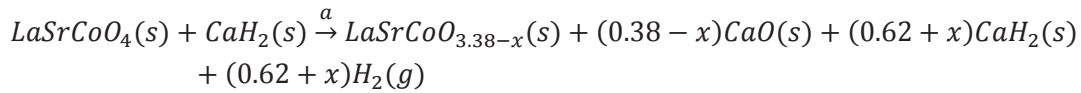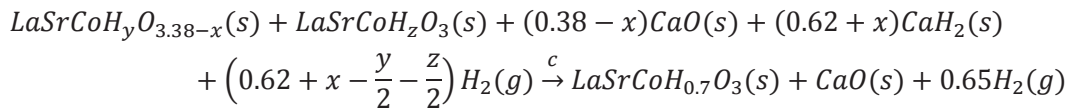
The general aspects of the reaction path outlined for $LaSrCoH_{0.7}O_3$ is considered valid for other compounds such as $BaTiH_xO_{3-x}$, $SrVHO_2$ and $LaSr_3NiRuH_4O_4$ as well. It is worth to note that the hydrogen content in the product is dependent on the partial pressure of H_2. This is because the hydride anions in the product is in equilibrium with hydrogen in gas-phase, thus a high partial pressure of H_2 is needed to achieve high hydride content in the product.[53] From the proposed reaction mechanism, it is evident that direct substitution coupled with reduction is excluded.

For the perovskite oxyhydride $EuTiH_xO_3$, the precursor material is the pyrochlore $Eu_2Ti_2O_7$.[57] Still the reaction is a topotactic anion-exchange process as the pyrochlore is first reduced to the

corresponding EuTiO$_3$ perovskite. Subsequently, the perovskite is anion-exchanged into an oxyhydride through a topotactic reaction.

LnHO (Ln = La, Ce, Pr, Nd, Sm, Gd, Tb, Dy, Ho, Er) can also be prepared by reaction with CaH$_2$.[68-71, 73] In this case, there exists no structural relation between Ln$_2$O$_3$ and LnHO, thus it is not a topotactic anion-exchange reaction. For this reason, nucleation and crystal growth are steps encountered in the reaction. The reaction can be described by the following equation:

$$La_2O_3(s) + CaH_2(s) \rightarrow 2LaHO(s) + CaO(s)$$
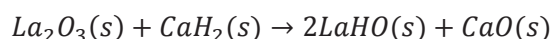
The flux method (or molten salt method) refer to a synthesis route where the components to make a product is dissolved in a molted medium (flux or solvent).[97] The molten salt serve as a reaction medium for the components.[98] The high mobility in the molten salt give a high reaction rate and the reaction can be carried out at moderate temperatures. Nucleation and crystal growth occur either in the melt or during cooling. The change of state promotes formation of single crystals in contrast to methods as solid-state reaction where the components does not change state. After synthesis, the flux is removed by washing in a solvent to obtain the pure product as for topotactic anion-exchange with a metal hydride. This procedure also removes excess metal hydride, which is commonly used.

La$_2$LiHO$_3$ is the only oxyhydride obtained by the flux method without impurities.[74] Attempts with heavier lanthanides gave impurities in the product. As the flux method only need moderate temperatures, it is suited for oxyhydride synthesis. Currently, no details on the formation mechanism of Ln$_2$LiHO$_3$ is at hand, and we therefore summarize the overall reaction by the following equation.

$$La_2O_3(solv) + LiH(solv) \xrightarrow{LiCl} La_2LiHO_3(s)$$

The last method used to prepare oxyhydrides is the self-flux method.[99] The approach is similar to the ceramic method, however a surplus of lithium hydride is used (100−300 mass %). When the reaction is carried out close to the melting point of lithium hydride, the mobility in lithium hydride increases and it serve as a self-flux. The high mobility in the flux assists diffusion and highly crystalline samples may be obtained by this approach. As the halide-flux method, the self-flux method opens for preparation of large sample quantities, but the product must be washed after synthesis. A disadvantage is the safety aspect of using large amount of lithium hydride for synthesis.

Comparing the pros and cons of the methods discussed above, all methods are suited for oxyhydride synthesis with their advantages and drawbacks. All methods typically use a surplus of metal hydride. However, this is only removed by washing in the topotactic anion-exchange method and the flux methods. In the ceramic method, surplus of components is not removed as a

part of the procedure, *i.e.* oxyhydrides obtained by the high-pressure method may contain impurities.

Further, it is noteworthy that all transition metal containing oxyhydrides are prepared by either high pressures or topotactic anion-exchange. $La_{2-x-y}Sr_{x+y}LiH_{1-x+y}O_{3-y}$ is prepared by four methods, ceramic methods with and without high pressures, and the halide- and self-flux method. The fact that the compound is prepared by three different methods suggest that the compound can be one of the easier oxyhydrides to prepare.

3. Theory and characterization methods

This work cover the oxyhydride series $La_{2-x}Nd_xLiHO_3$ and $LaSr_3Fe_3H_yO_{10-x}$. The studied compounds are obtained by means of the halide salt flux, topotactic anion-exchange by CaH_2 and the sol-gel methods, respectively. All synthesized samples are on routine basis characterized in terms of phase purity, crystal structure, chemical composition, morphology and thermal stability using X-ray diffraction (XRD) and Rietveld refinements, thermogravimetry (TGA) with differential scanning calorimetry (DSC) and integrated gas effluent analysis by mass spectroscopy (MS), cerimetric titration and scanning electron microscopy (SEM), see Table 5.

Selected samples were examined in more detailed investigations with the purpose to correlate structural aspects and chemical bonding, to hydride anion mobility and thermal stability. Methods applied in these efforts are neutron diffraction, inelastic neutron spectroscopy (INS), quasi-elastic neutron spectroscopy (QENS), pair distribution function (PDF) analysis and density functional theory (DFT) calculations. In addition, an attempt to perform precession electron diffraction tomography (PEDT) was carried out on La_2LiHO_3. Finally, from combined X-ray and neutron diffraction, we described the nuclear and magnetic structure of $LaSr_3Fe_3O_9$, and by treating multiple data sets simultaneously we benefitted from surface Rietveld refinements to study the oxidation of $LaSr_3Fe_3O_9$ to $LaSr_3Fe_3O_{10}$.

In the following, we present more details and how experiments and calculations have been performed on the more advanced characterization methods, with focus on those less utilized in our research group. In the overview (Table 5) these methods are written in *italic*. In particular, we will highlight the important role of neutrons relative to X-rays and electrons for the systems under investigation. For this reason, the text on scattering will be built up around neutron scattering. With respect to theoretical aspects connected to basic experiments and standard characterization techniques common for our research group, we refer the reader to the literature (diffraction and crystal structure refinements,[100-104] SEM,[105] materials synthesis,[94] and magnetism[106-107]). Thermal analysis and cerimetric titration is briefly discussed in section 3.3.

Table 5: Overview of used characterization methods in this work. Characterization methods are separated in general methods and techniques for material characterization, and more special and advanced methods and techniques. Techniques and methods in italic indicate that it is more advanced. [a] in this work diffraction refers to powder diffraction unless otherwise is specified. Thus, all diffraction experiment presented in this thesis is carried out on powders.

Methods and techniques for general materials characterization	$La_{2-x}Nd_xLiHO_3$	$LaSr_3Fe_3O_{10-x}$
Phase identification and structure refinements (home lab XRD, Rietveld refinements) [a]	x	x
Thermal stability and oxygen content (TGA, DSC, MS)	x	x
Titration for oxygen content analysis (Cerimetric titration)		x
SEM for morphology	x	x
Magnetic property investigations		x
Raman spectroscopy	x	x
Methods and techniques for dedicated investigations of selected samples		
Crystal structure analysis for location of light elements (H, Li, O) and *magnetic structures* [a]	x	x
Local structure analysis (PDF)	x	
Crystal structure determination by *PEDT*	x	
Hydride anion bonding and mobility (*INS, QENS*, DFT)	x	
Surface and combined Rietveld refinement of multiple data sets	x	x

3.1   Fundamentals of scattering techniques

The neutron is a subatomic particle. It is stable when bound in the nucleus of an atom, while a free neutron has a lifetime of about 15 minutes. As the neutron has zero charge, it can interact with matter through short-ranged nuclear interaction. The ½ spin of the neutron means that the neutron may also interact magnetically. The probability (or cross section) for nuclear and magnetic interaction is small, meaning that the neutron can penetrate deeply into the bulk of a specimen before being scattered. For this reason, large sample quantities are needed for neutron scattering experiments. The unique properties of neutrons make them a powerful probe to study matter, and neutron scattering techniques have been and are of great importance in research. The most important properties of the neutron are summarized in Table 6.

Table 6: Fundamental properties of a free neutron.

Mass, m_n	1.0087 atomic units
Charge	0
Spin, S	½
Magnetic moment, μ_n	$\mu_n = \gamma\mu_N, (\mu_N = \frac{e\hbar}{2m_p}, \gamma = -1.913)^a$
Mean lifetime, τ	886 ± 1 s

^a e is the elementary charge, $\hbar$ is the reduced Planck constant, m_p is the mass of a proton (same as neutron), and γ is a constant.

For neutron scattering experiments, neutron beams with a flux suitable for neutron scattering experiments are produced by two means: fission and spallation.[100] Traditionally, fission-based reactor sources are more common, but today spallation sources are most frequently built due to higher neutron brightness and more neutrons per unit heat. Additionally, reactor sources need highly enriched uranium, which is frowned upon in today's society. In a fission reaction, a high continuous flux of neutrons is produced in the core of the reactor, typically from uranium. In a spallation reactor, pulses of neutrons are produced by bombarding a target made of a heavy element with high-energy particles, typically protons. The target then undergo nuclear decay and releases neutrons.[100]

Examples of reactor sources are Institut Laue-Langevin (ILL) in Grenoble, France; Helmholtz-Zentrum Berlin (HZB) in Germany and Institute for Energy Technology (IFE) at Kjeller, Norway. Well-known spallation sources are ISIS pulsed neutron and muon source in Oxfordshire, United Kingdoms; J-Parc in Tocai, Japan; and European Spallation Source (ESS) in Lund; Sweden (under construction). IFE and ISIS are the facilities used in this work.

When neutrons are produced, they have high energy. To be utilized in scattering experiments, neutron with lower energy may be needed. Thus, the neutrons are slowed down, cooled or "moderated". This is done in a moderating medium like liquid H_2, methane or water, where the

temperature of the medium dictates the energy of the neutrons. To get an idea of the effect the moderation has on the neutron, we can consider the wave-particle nature of the neutron, which is given by the de Broglie wavelength. The following expression is then valid for a neutron with a given kinetic energy, E_n:

$$E_n = \frac{m_n v_n^2}{2} = \frac{h^2}{2 m_n \lambda_n^2} = k_B T$$

Where h is Planck's constant, m_n is the neutron mass, v_n is the neutron velocity, λ_n is the de Broglie wavelength associated with the neutron and k_B is Boltzmann constant. For T ~ 300 K, this corresponds to a wavelength around 2 Å. This distance is comparable to interatomic distances in solids and neutrons and are therefore well suited for studies of the atomic arrangement of condensed matter through diffraction (elastic scattering). Further, the kinetic energies associated with such neutrons are in the order of meV (25 meV at 330 K). This energy range is similar to that of the vibrational modes in matter, thus, neutrons are also well suited to study atomic dynamics by spectroscopy (inelastic scattering). X-rays on the other hand have energies in the order of keV and are therefore not well suited to probe atomic dynamics in matter. A summary of the relation between different properties associated with a neutron is given in Table 7.

Table 7: Relationships of different properties associated with a neutron. Adapted from ref.[100]

	E (meV)	v (km/sec)	λ (Å)	T (K)
Energy E of 1 meV	1	0.437	9.045	11.60
Velocity v of 1 km/sec	5.227	1	3.956	60.66
Wavelength λ of 1 Å	81.81	3.956	1	949.3
Temperature T of 1 K	0.086	0.128	30.81	1

As neutrons are particles, the time-of-flight principle can be used to separate neutrons by energy.[101] By this approach, high resolution can be achieved in diffraction and spectroscopy experiments. X-rays on the other hand are photons and cannot be separated by time-of-flight. Thus, X-rays are suited for different spectroscopy experiments than neutrons, *e.g.* absorption spectroscopy (XAS).

In contrast to neutrons, X-rays can be produced with extremely high brilliance at synchrotron facilities (synchrotron radiation, SR) and in reasonable brilliance by X-ray tubes in a home laboratory. In an X-ray tube, X-rays are generated by applying a high voltage over two electrodes in vacuum. The high voltage causes the cathode to emit electrons that are accelerated towards the anode, which typical are metals like copper, chromium, molybdenum and silver. The electrons stop in the anode and the de-acceleration of the electrons releases a white X-ray spectrum. This is known as bremsstrahlung. Additionally, the electrons might knock out core electrons in the anode. The following relaxation of the outer electrons give rise to sharp lines in the emission spectra,

with an energy depending on the involved electrons and element of the anode. An X-ray wavelength can then be chosen with a monochromator to use in an experiment.

Similarly, in a synchrotron, electrons are accelerated around a storage ring. The path of the electrons is controlled by bending magnets and as the direction of the electrons are changed in the bending magnet, X-rays are released. At modern synchrotron facilities, undulators are used to generate extremely intense X-rays. An undulator consists of several magnets, forcing the course of the electrons to be wiggled back and forth, thus generating much more intense X-rays than a bending magnet. The beam can then be focused and monochomatized to achieve a beam with high brilliance. Synchrotrons allow advanced diffraction experiments with extremely high resolution, time-resolution, spatial resolution with nano-sized beam, large Q-range (section 3.2.2), and surface and interface diffraction. Although high brilliance is useful in many experiments, radiation damage can be an issue when samples are exposed to large X-ray doses, *e.g.* for (metallo-) proteins.[104, 108]

3.2 Elastic and inelastic scattering

We distinguish diffraction from spectroscopy by the type of scattering. In a diffraction experiment, the scattering is elastic (*i.e.* there is no transfer of energy from the diffracted neutron to the sample), while in spectroscopy, the scattering is inelastic. This means that neutron spectroscopy involves energy transfer between the neutron and the sample. By studying the energy associated with dynamics, insight to the interactions and origin of physical phenomena can be gained.

The energy range that can be probed with neutrons is illustrated in Figure 14. For zero energy transfer (elastic scattering), we have sharp peak. This peak corresponds to diffraction. In a diffraction experiment we measure the intensity of the zero-energy transfer peak at several momentum transfers. This yields information about interatomic distances and atomic arrangement. Several peaks associated with energy transfer are also shown in the illustration (Figure 14). These peaks arise from interactions between neutrons and dynamics in the sample. This can be *e.g.* diffusion, vibrations, phonons, magnons and molecular rotations.[101] Thus, neutrons are an ideal probe to gain insight to physical phenomena in matter.
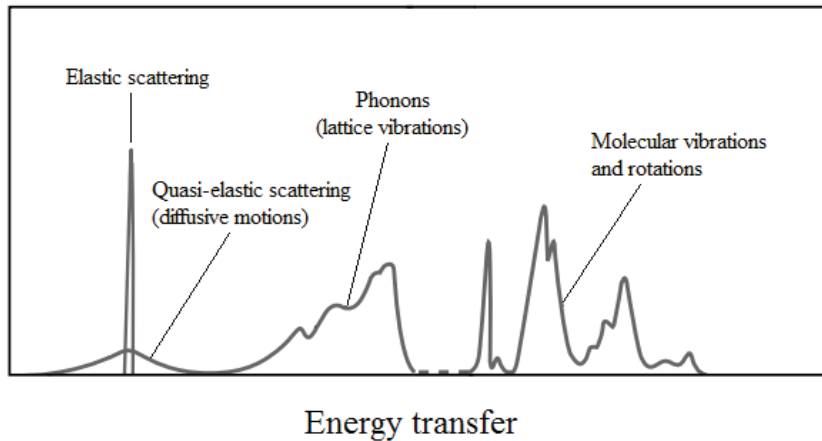
Energy transfer

Figure 14: Illustration of the inelastic scattering (dynamics) from a material accessible with neutron scattering. The elastic peak corresponds to zero energy transfer and thus diffraction. Figure adapted and reused with permission from Elsevier.[109]

3.2.1 Diffraction

Diffraction is the most widespread method used to study the atomic arrangement of solids. The general theory is extensively described in literature and will not be discussed in detail here.[100-104] However, some important aspects of diffraction need to be illuminated in order for the reader to fully understand this work.

Diffraction is associated with coherent elastic scattering. Thus, in a diffraction experiment, it is the coherent scattering cross section that measure the probability of a scattering event to occur. Coherent and incoherent scattering will be further discussed in section 3.2.3. The scattering cross section (σ) is related to the scattering length by the equation below.

$$\sigma = 4\pi b^2$$

where b is the scattering length. The scattering length of a neutron refer to the strength of the interaction between a neutron and an atom in a scattering event. This is analogous to the form factor for X-rays. Note that the neutron scattering length may be negative, *e.g.* as for hydrogen.

While X-rays are scattered by the electrons, neutrons are scattered by the nuclei of the atoms. For this reason, the X-ray scattering cross section of the elements increases with the square of the atomic number (*i.e.* the number of electrons). The neutron scattering cross section on the other hand, shows little systematic variation with respect to the atomic number, Figure 15. Further, different isotopes of the same element have different neutron scattering cross sections. Thus, neutrons have the potential to be well suited to study samples with elements that are near neighbors in the periodic table or mixtures of light and heavy elements.

In addition to the diffraction signal from coherent scattering, incoherent scattering from atoms will be imposed in a measured diffraction pattern in the background. The high incoherent scattering cross section of hydrogen (section 3.2.3) yields significant background in diffraction experiments of materials with high hydrogen content, *e.g.* as metal hydrides, proteins, polymers and organic compounds.[103] In cases the incoherent background from hydrogen (^{1}H) is severe, an isotope exchange from natural abundant hydrogen to deuterium is a solution as deuterium has a significantly lower incoherent scattering cross section than hydrogen. For organic materials, deuteration can be very challenging. In this work, both hydrogen and deuterium containing samples have been investigated by neutron diffraction. With low atomic concentration of hydrogen, as for La_2LiHO_3 (1/7 = ~14.3 %), the incoherent scattering from hydrogen yields manageable background levels. However, deuterated samples were measured for PDF experiments (section 3.2.2.2) to reduce the background at high Q-values.

On the other hand, with X-rays it can be difficult to distinguish neighboring elements in the periodic table and light elements are difficult to detect. Additionally, the X-ray form factors *f(Q)* fall off rapidly with increasing momentum transfer. Whereas the neutron scattering lengths show no dependence of the momentum transfer, Q. Some elements have very high absorbing neutron cross section and are thus not suited for neutron scattering experiments. Similarly, X-rays are strongly absorbing at low photon energies.[104]
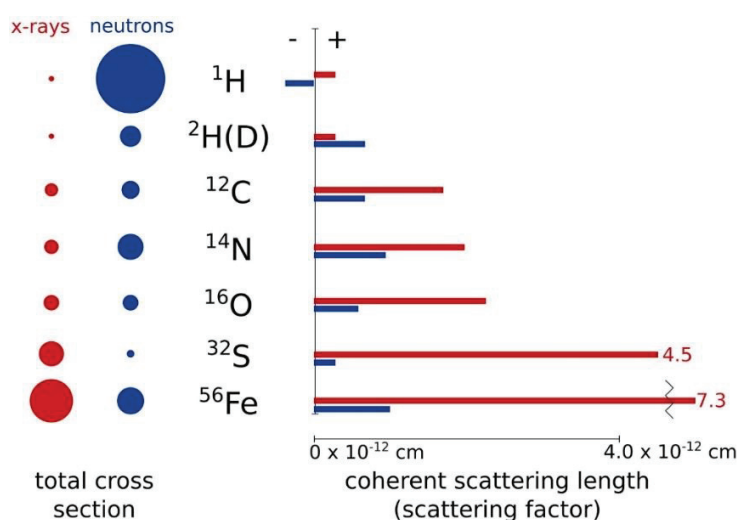
Figure 15: Comparison between X-ray and neutron scattering cross section (left) and coherent scattering length/factor, showing how X-ray scattering factor increases with atomic number, while neutron scattering cross section is independent of atomic number and is isotope sensitive. Reused with permission from Elsevier.[110]

Atoms with unpaired electrons possess a magnetic moment. In a solid, the magnetic moments are either disordered (paramagnetic) or ordered (ferro-, ferri- or antiferromagnetic). For the ordered magnetic states, a magnetic structure is present in the solid. The magnetic structure does not

necessarily share the same unit cell as the nuclear cell. In the case of $LaSr_3Fe_3O_9$ which is investigated in this work, the unit cell is found to be the same, but the symmetry is different due to the ordered magnetic moments of the iron atoms. The spin of the neutron allows us to probe the magnetic structure and quantify the magnetic moment of the atoms. It should be noted that this case, the neutrons are scattered by the electrons, hence magnetic scattering lengths show the same dependence on momentum transfer as the X-ray form factors, *i.e.* in neutron diffraction, the intensity of the diffraction peaks from the magnetic structure will decay with increasing scattering angle and are therefore mainly observed at low scattering angles.

The main drawback of neutron scattering techniques are the difficulty of producing a high flux beam of neutrons. For this reason, large facilities like reactor sources or spallation sources, together with large sample quantities, are needed for experiments. The resolution of neutron diffraction instrumentation is generally inferior to the X-ray analogs.

In this work, neutron diffraction has been vital due to the composition of the investigated samples. Combinations of light and heavy elements, such as in La_2LiHO_3, is difficult to investigate with only x-ray diffraction where the scattering from lanthanum would dominate over the lighter elements. Further, neutron diffraction is needed to achieve the elemental contrast to accurately describe the oxygen positions, and the complete crystal and magnetic structure of $LaSr_3Fe_3O_9$. Because of these reasons, neutron diffraction was essential for structural study of oxyhydrides.

3.2.1.1 Electron diffraction

Electron diffraction has proven itself as a useful alternative to X-ray and neutron diffraction.[111] Unlike X-rays and neutrons, electrons interact strongly with matter through Coulomb forces. This include that the electrons interact with both the nuclei and the electron cloud of an atom. X-ray and neutron diffraction are typically considered within the kinematical theory of diffraction which consider the position of Bragg reflection is reciprocal space. As the interaction between electrons and matter is strong, the electron scattering cross sections are very large, which leads to strong multiple scattering.[112] This is known as dynamical effects and have made structure determination and refinements of electron diffraction challenging.[113] Thus, unlike for X-ray and neutron diffraction dynamical theory must be considered, which corrects for multiple scattering, refraction, shape and width of the reflections in reciprocal space, when analyzing electron diffraction. It must be noted that to minimize dynamical effects, very thin samples must be measured. Radiation damage can also be an issue in electron diffraction.

During the last ten years, electron diffraction tomography has proven itself as a useful technique for solving crystal structures and developing reliable crystal structure models.[114-115] Unfortunately, dynamic effects make accurate structural refinements difficult, even if precession electron diffraction is used to limit the dynamic diffraction effects.[116] However, Palatinus *et al.*, recently

reported "proof of concept" structural refinements of precession electron diffraction tomography (PEDT) data using Bloch-wave formalism for the calculation of diffracted intensities.

In PEDT, a large area of reciprocal space is measured and thus many reflections, yielding much information about the crystal structure. Refinements where dynamical effects are taken into account, then allows for high quality structural refinements.[111, 117] Further, parameters like site occupancy of oxygen can also be refined accurately. A guide to dynamical refinements is given by Palatinus *et al*.[111] Palatinus *et al*. further showed that this method even is suited to observe hydrogen in a crystalline compound, exemplified by paracetamol and cobalt aluminophosphate.[118] In paracetamol, only light elements as carbon, nitrogen and oxygen are combined with hydrogen, and for the latter compound hydrogen is in a matrix composed of oxygen, aluminum and cobalt.

3.2.2 Data analysis – Diffraction

3.2.2.1 (Surface) Rietveld refinements

Rietveld refinements is the most widespread method used to extract crystal structure data from powder diffraction patterns.[119] The method is based on the least square approach to refine a calculated diffraction pattern, and minimize its difference to a measured diffraction pattern by varying the parameters applicable for the crystal structure. The intensity of all the Bragg reflections are calculated from the crystal structure and by applying corrections, an experimental pattern is simulated. In this manner, the position, intensity and broadening of the Bragg peaks are used to quantify the crystal structure of the measured sample. In the refinement, the difference between the observed and calculated diffraction pattern is minimized, as in the following expression:

$$M = \sum_i w_i (Y_{iO} - Y_{iC})^2$$

where w_i is the weight, Y_{iO} is the observed and Y_{iC} is the calculated intensity in point i.[102] Y_C is calculated based on a model of a crystal structure and other parameters, the expression for Y_C is given below:[120]

$$Y_{iC} = S \sum_K (m_K \, L_K \, |F_K|^2 \, \varphi(2\theta_i - 2\theta_K) P_K A + y_{ib})$$

where S is the scale factor, K represent the Miller indices (h, k, l) of a Bragg reflection, F_K is the structure factor, m_K is the multiplicity, L_K is the Lorentz factor, φ is the peak profile function, $2\theta_i$ is the scattering angle of at point i, $2\theta_K$ is the scattering angle of reflection K, P_K is the preferred orientation function, A is an absorption factor and y_{ib} is the background at point i. The structure factor gives the scattering contribution to a reflection for an atom and is given by:

$$F_K = F_{hkl} = \sum_j s_j o_j e^{2\pi i(hx_j + ky_j + lz_j)} e^{-\frac{B_j^2 \sin^2 \theta}{\lambda^2}}$$

Where s_j is the scattering length or form factor, o_j is the occupancy, B_j is the Debye-Waller factor and x_j, y_j, z_j is the coordinates of atom j. λ is the wavelength in the diffraction experiment. The Debye-Waller factor describe the attenuation of scattering as a function of scattering angle or Q, where Q is a vector that describes the scattering momentum transfer and is given by:

$$Q = \frac{4\pi \sin \theta}{\lambda} = \frac{2\pi}{d}$$

Where d refers to interatomic distances. Q-range is typically referred to as the accessed region of momentum transfer. The quality of the refinement can be evaluated based on the following residual functions:

$$R_p = \sqrt{\frac{\sum_i |Y_{iO} - Y_{iC}|}{\sum_i Y_{iO}}}$$

and:

$$R_{exp} = \sqrt{\frac{\sum_i N_{obs} - N_{var}}{\sum_i w_i Y_{iO}^2}}$$

and:

$$R_{wp} = \sqrt{\frac{\sum_i w_i |Y_{iO} - Y_{iC}|^2}{\sum_i w_i Y_{iO}^2}}$$

and:

$$gof = \chi^2 = \frac{R_{wp}}{R_{exp}} = \sqrt{\frac{\sum_i w_i |Y_{iO} - Y_{iC}|^2}{N_{obs} - N_{var}}}$$

Where N_{obs} is the number of data point, N_{var} is the number of refined parameters and gof refers to "goodness of fit".

From a Rietveld refinement of one single diffraction pattern, parameters such as unit cell parameters, atomic positions, occupancies of atoms and fractions of different phases can be determined. With the high flux provided by modern X-ray sources such as synchrotrons, in combination with fast 2D detectors, it is possible to measure many diffraction patterns in a short

period of time. By performing diffraction studies as a function of an external variable, *i.e.* temperature or time, more insight into a system can be gained than through one single diffraction experiment. This makes it possible to follow chemical reactions *in situ* (following crystal structure changes during reaction) or study devices *operando* (following crystal structure changes during operation of device while also measuring device output). Studies of these types will generate large datasets, possibly several hundred diffraction patterns. To analyze this amount of data one could use a sequential approach, as it would take too long to refine the diffraction patterns one by one. By this approach, the diffraction patterns are refined individually. However, this results in the refinement of more parameters than are necessary.

Surface Rietveld refinement is an approach where all datasets from an experiment are simultaneously refined and one or more parameters are restricted to be the same for all diffraction patterns.[121] Thus, several patterns are used to determine a few parameters. The number of free parameters is then reduced compared to a sequential refinement, and the precision of the shared parameters can be improved. For example, zero-point error and instrumental peak shape are typically the same for all diffraction patterns, and hence should be restricted to be the same for all powder patterns in the dataset. Depending on the nature of the system, atomic positions, thermal parameters and unit cell parameters might also be restricted.

Another approach is parametric Rietveld refinements. Here, some selected parameters are chosen to be a function of a variable, *i.e.* a function of temperature or time. Thus, one can apply physical models during data analysis and refinement of "non-crystallographic" variables, such as temperature for each dataset.

In this work, the surface Rietveld refinement approach has been adopted to study the phase relations in the $LaSr_3Fe_3O_{10-x}$ and $La_{2-x}Nd_xLiHO_3$-systems. The TOPAS V5 software has been used, which is a fast and robust software that can handle large number of free parameters.[122-123] The software runs from input files written in a user-friendly C++ based language and supports user-defined equations. In TOPAS a parameter is defined using the "prm" or "local" keywords as follows:

prm some_parameter = 1.0 ;

Surface Rietveld refinements were carried out by first preparing an initial input file. In the initial input file, two types of parameters are defined:

prm parameter_a = 4.0 ;

and:

prm parameter_a_XXXX = 4.0 ;

or:

local parameter_a = 4.0 ;

In a chosen range (number of diffraction patterns), a string (here XXXX) is exchanged with a series of numbers relating to the relevant powder patterns in the dataset using a Python script and a file is written composed of the initial input file with the replaced string, repeated within the selected range. A parameter followed by _XXXX will then be refined for each individual diffraction pattern, while a parameter without _XXXX will be restricted to be the same for all diffraction patterns. Similarly, a parameter defined by the local keyword will be refined individual, although the parameters is defined for several diffraction patterns.

3.2.2.2 Total scattering – Pair distribution function (PDF)

In diffraction we probe the periodicity of atoms, thus we study the average atomic arrangement of a compound. This information will manifest itself in the Bragg peaks in a diffraction experiment. To this point, crystal structures have been considered as a rigid unit without discrepancies. Although it is pleasing to consider crystal structures as perfectly arranged, it does not reflect the real atomic arrangement. All crystals have some degree of disorder. In some cases, it is vacancies and/or interstitial atoms. In other cases, there are severe degree of disorder and the local structure deviate from the average crystal structure. Disorder like stacking faults and deviations from the average crystal structure will give rise to diffuse scattering.[124-125] Total scattering methods treat both the Bragg diffraction and the diffuse scattering to derive structural information about a material and will be briefly discussed in this chapter.[126-127]

The difficulty in total scattering is to quantify the diffuse scattering. Unlike in Rietveld refinements of diffraction patterns, the diffraction pattern itself is not used for the analysis. To treat total scattering data, experimental artifacts and background are subtracted from the measured data, and the data is converted into the pair distribution function $G(r)$ by a Fourier transform. Alternative real-space scattering functions can also be used, and an overview is given by Keen for single phase systems and by Sławiński for multi-component systems.[128-129] $G(r)$ represents real space in contrast to a diffraction pattern, which is measured in reciprocal space. This means that peaks in $G(r)$ give interatomic distances in the atomic structure directly. Total scattering is typically referred to as PDF (pair distribution function) analysis, as it is $G(r)$ that is used in the data analysis. The fact that the diffraction pattern is Fourier transformed, makes it important to collect data to high Q and with good counting statistics to achieve a high-quality $G(r)$.

If we consider a normal diffraction experiment, a nanoparticle will give broad peaks due to the small crystallite size. In $G(r)$ the nanoparticle will give a strong signal at low r as the interatomic distances are well defined at short distances. A structural model can be refined to $G(r)$, using a least squares method similar to a Rietveld refinement and structural can be extracted. The

difference from a Rietveld refinement is that the local structure is being refined, giving information on short-range atomic correlations. This method is also referred to as a small-box approach, as only one unit cell is considered. The signal from the nanoparticle in $G(r)$ will decay and vanish dependent on the crystallite size. In other words, crystallite size is also refined.

This is nicely exemplified by CdSe nanoparticles, Figure 16.[130] The diffraction pattern of bulk CdSe show well defined and sharp reflections in the diffraction pattern. The three different sizes of nanoparticles show broader and less defined peaks. For the smallest nanoparticles, the reflections are almost blurred out, thus illustrating the effect small crystallite size. As Rietveld refinements use the Bragg reflections for quantifying the crystal structure, the nanoparticles are not well suited for this kind of analysis. The $G(r)$ on the other hand, which show well define features for both the nanoparticles and the bulk sample. At higher r, no signal is observed for the nanoparticles due to the small crystallite size. This is because $G(r)$ is in real-space, thus the signal does not expand beyond the crystallite size. For refinements of $G(r)$ by the small-box approach, software as *PDFgui* can be used.[131]
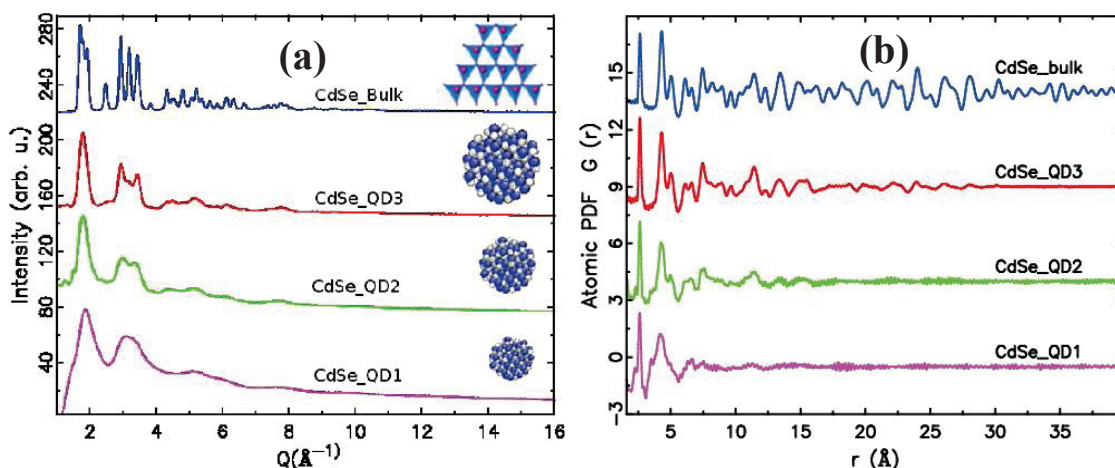

Figure 16: (a) X-ray diffraction patterns of bulk CdSe and CdSe quantum dots. (b) Obtained *G(r)* **from the diffraction data. The quantum dots where refined to a particle size of 3.7(1), 2.2(2) and 1.3(2) nm for QD3, QD2 and QD1 respectively. Reused with permission from Taylor & Francis.[130]**

Another method for refinement of a crystal structure against $G(r)$ is the reversed Monte-Carlo (RMC) approach.[102] This approach is referred to as a large-box approach and software as *RMCprofile* can be used for data analysis.[132] The reason for this is that a large box derived from several unit cells containing a large number of atoms without the symmetry constraints of a crystal structure model is used in the refinement. The atoms are allowed to randomly arrange themselves within the constraints set by the user. The basic constraints are the boundaries of the box and hard sphere repulsion (which prevents two atoms from occupying the same space), though other constraints may also be applied on the basis of chemical or physical knowledge. The method then

gives structural information on an intermediate length scale and is typically used to study disordered materials. As the obtained solution is not prejudiced, but consistent with the data, the method is considered to be unbiased.

The displacive phase transition in the perovskite $SrTiO_3$ nicely illustrate the utilization of the RMC method.[133] The high temperature cubic crystal structure of $SrTiO_3$ transform into a tetragonal crystal structure below 105 K, Figure 17 a and b. As a large-box approach was used for this analysis, correlations as interatomic distances to nearest and next-nearest neighboring atoms, and rotations of octahedra can be extracted from the large box of atoms used in the refinement. The single layer of TiO_6-octahedra shown in Figure 17 e illustrates the number of atoms used in a large box refinement, compared the single unit cell, Figure 17 a and b, which is used in a small-box or Rietveld refinement. In this case we see that above 105 K, the distribution of the TiO_6-octahedra rotation is centered as a single peak around 0°, while below 105 K the rotation around the *z*-axis is split into two components, Figure 17 c and d.[133] This behavior is agreement with a frozen phonon driven displacive phase transition and illustrates how the RMC approach can be used to find correlations on an intermediate length scale.[133]
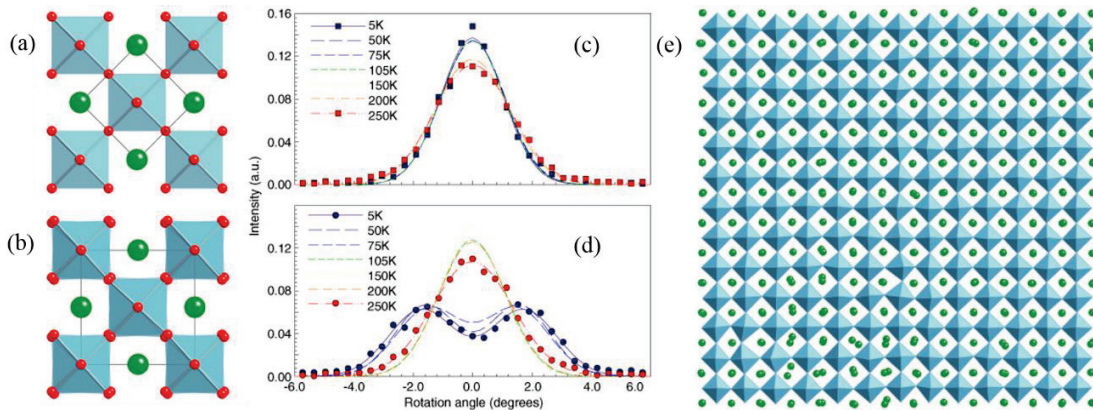

Figure 17: Crystal structure of the cubic (*Pm-3m*) high temperature (a) and tetragonal (*I4/mcm*) low temperature (b) phases of SrTiO₃. Distribution of the TiO₆-octahedra rotation around the *x*- and *y*- (c), and *z*-axis (d). (e) Single layer of TiO₆-octahedra (blue) from the RMC refinement at 298 K, strontium atoms in green. Reused with permission from IOP Publishing.[133]

3.2.3 Neutron spectroscopy

Neutron spectroscopy refers to inelastic neutron scattering. Thus, there is an energy transfer between the neutron and the sample. In neutron spectroscopy both the coherent and incoherent scattering contribute to the scattering. Coherent scattering arises from interference effects and gives information on space and time relations between different atoms, *i.e.* the relative arrangement of atoms (crystal structure) or the collective vibration/motion of atoms (phonons).

Incoherent scattering yields information of an atoms position at time *0* and the same atoms position at time *t*. This means that the incoherent scattering gives information about the properties of individual atoms. The different scattering cross sections of some selected elements are visualized in Figure 18. The different elements show completely individual size of the different cross section. Most obvious is the large incoherent cross section of hydrogen, which allow us to almost specifically probe hydrogen with neutron spectroscopy. For this reason, neutron spectroscopy is the ideal technique to probe the dynamics of hydrogen in oxyhydrides.
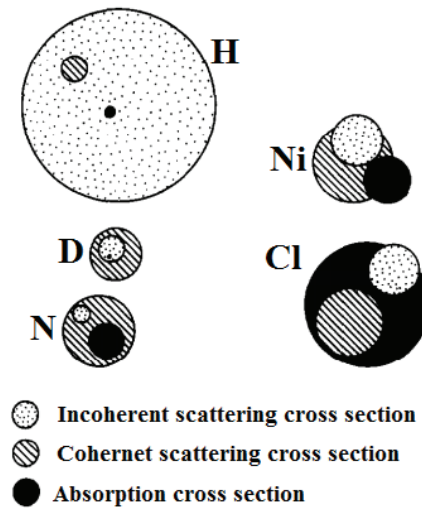

Figure 18: Visualization of the different neutron scattering cross sections. Reused with permission from Elsevier.[109]

3.2.3.1 Small energy transfers – Quasi-elastic neutron scattering (QENS)

Quasi-elastic neutron scattering (QENS) refers to energy transfers between the neutron and the sample which are very small or almost elastic, hence, quasi-elastic. Further, in a QENS experiment, the energy resolution is in the order of μeV. The IRIS instrument at ISIS pulsed neutron and muon source used in this work has a resolution of 17.5 μeV, which is typical for QENS experiments. A typical experimental energy range is then around 1−4 meV.

If an atom undergoes stochastic motion (diffusion) during the scattering event between the atom and a neutron, then energy transfer to or from the neutron accompanies this single-particle scattering event. As the energies for this kind of motions are small and are not quantized, this will be observed as a broadening of the sharp peak arising from elastic scattering (zero energy transfer). The broadening of the elastic peak is dependent of the momentum transfer. By modelling and fitting the broadening as a function of the momentum transfer and temperature, insight into the jump rates, jump lengths and jump directions of the moving atoms can be obtained.

3.2.3.2 Intermediate energy transfers – Inelastic (vibrational) neutron spectroscopy (INS)

Vibrational neutron spectroscopy, INS, probes vibration in a similar energy range to Raman and infrared spectroscopy. However, unlike Raman and infrared spectroscopy, there are no selection rules for allowed vibrations (all active vibrations are, in principle, measurable) and INS observations are not limited to the center of the Brillouin zone (gamma point). Further, in INS both coherent and incoherent scattering is included. Hence, the intensity of the vibrations is weighted by the neutron scattering cross sections of the elements in the sample, *i.e.* as hydrogen is a very strong incoherent scatterer, the vibration originating from hydrogen will be dominant in an INS spectrum. For this reason, typical topics investigated by INS include catalysts, hydrogen storage materials, hydrogen bonded systems, biological samples and organic compounds such as drugs. The typical energy range investigated in an INS experiment is $0-500$ meV ($0-4000$ cm^{-1}) with a resolution around 1 % of the energy in picture.

3.2.3.3 Large energy transfers – Neutron Compton scattering (NCS)

Neutron Compton scattering, NCS, or Deep inelastic neutron spectroscopy (DINS), uses high energy neutrons and thus, large energy transfers between the neutrons and the sample.[134] Due to the large energy of the incident neutrons, the impulse approximation is used to describe the scattering process. The scattering function under the impulse approximation consist of a series of peaks, one for each mass percent in the sample. Each peak is due to the fulfillment of the conservations laws of energy and momentum transfer for the neutron-nuclei system, thus is associated with the recoil energy of the nuclei. Accordingly, we get a relation between the momentum and energy transfer of the scattered neutron. As the peaks are separated by mass, NCS give distinct information for the different atom types, and NCS probes the momentum distribution of an atom, giving information on the bonding and local potential of the atom.

3.3 Other methods

3.3.1 Thermal analysis

Thermal analysis refers to methods where the properties of a sample is monitored over time and temperature variations.[135] The sample can be investigated over a range of different heating and cooling sequences, and different atmospheres can be applied. The most common thermal analysis methods are given in Table 8. In thermogravimetry (TGA) the mass is monitored by a very accurate balance, and mass changes indicate that the sample undergoes chemical reactions as decomposition, dehydration or oxidation. Due to the high accuracy in mass changes, *e.g.* the amount of oxygen picked up by the sample can be accurately monitored, and the associated change in oxygen content can be calculated. In TGA, the buoyancy is the upward force on the sample

produced by the surrounding atmosphere, which will affect the apparent mass during TGA experiment. The buoyancy effect occurs as the density of the atmosphere in the balance decreases with increasing temperature, resulting in an apparent mass gain. This is typically corrected for by running an experiment without sample in the instrument, *i.e.* a blank experiment. In addition, to monitoring the mass changes, the gas released can be monitored by mass spectroscopy (MS) or Fourier-transform infrared spectroscopy. This adds further possibilities to determine and understand chemical reactions.

Table 8: Overview of thermal analysis methods and their applications. The table is adaped from ref.[135]

Method	Abbreviation	Property	Application
Thermogravimetry	TG / TGA	Mass	Decomposition Dehydration Oxidation
Differential thermal analysis	DTA	Temperature changes	Phase transitions Reactions
Differential scanning calorimetry	DSC	Power difference (heat flow)	Heat capacity Phase transitions Reactions Calorimetry
Evolved gas analysis	EGA	Gases	Decompositions, Catalyst and surface reactions

Differential thermal analysis (DTA) and differential scanning calorimetry (DSC) are techniques that monitor the exothermic/endothermic effects in a sample. Differential implies that the effect is monitored versus a reference material which not undergo any heat effects in the temperature range and/or atmosphere conditions used in the experiment. Typical effects that can be studied by DTA and DSC is melting, crystallization, phase transitions, chemical reactions and electronic transitions. As DSC instruments can be calibrated, heat capacity and calorimetry can also be measured by DSC. In this work, $La_{2-x}Nd_xLiHO_3$ and $LaSr_3Fe_3O_{10-x}$ have been investigated with respect to thermal properties. In the case of the oxyhydrides, $La_{2-x}Nd_xLiHO_3$, the oxidation process was studied by combining TGA, DSC and MS, while in the case of $LaSr_3Fe_3O_{10-x}$, the oxygen non-stoichiometry at was studied by TGA.

3.3.2 Cerimetric titration

In this work, cerimetric titration was used to determine the oxidation state of iron and oxygen content in reduced samples of $LaSr_3Fe_3O_{10-x}$. Compared to TGA, moles are measured rather than mass, and correspondingly titration is less sensitive to small levels of impurities in metal oxides.[136] For titration based on oxidation of Fe^{2+}, an known quantity of Mohrs salt $[(NH_4)_2SO_4 \cdot FeSO_4 \cdot 6H_2O]$ is used in excess amount relative to the higher valent cation in the

sample ($Fe^{3+,4+}$) together with ferroin (Fe(II) 1,10-phenanthroline) as indicator in aqueous HCl solution.[136] Before titration, the solution contains a mixture of Fe^{2+} and Fe^{3+}. By adding a controlled amount of Ce^{4+} (cerium(IV) sulfate) solution, all remaining Fe^{2+} from the Mohr salt is oxidized to Fe^{3+}. The aqueous solution will be colored yellow by the ferroin indicator as long as Fe^{2+} is present in the solution. At the equivalent point, where the solution changes color, only Fe^{3+} is present, and the oxidation state/oxygen content can be calculated from the equation below.

$$x = \frac{M_{red} \cdot \left[\frac{m_{ms}}{M_{ms}} - C_{Ce^{4+}} \cdot V_{Ce^{4+}}\right]}{\left(n_B \cdot m_s - \frac{n_B}{2} \cdot M_O \left[\frac{m_{ms}}{M_{ms}} - C_{Ce^{4+}} \cdot V_{Ce^{4+}}\right]\right)}$$

where x is the excess oxidation state of the reduced derivative of the titrated compound with molar mass, M_{red}. In the case of $LaSr_3Fe_3O_{10-x}$, $LaSr_3Fe_3O_9$ was used as this derivative and the oxidation state of iron is then $3 + x$. Further, m refers to mass and M to molar mass of Mohr salt (ms), sample (s) and oxygen (O); $C_{Ce^{4+}}$ and $V_{Ce^{4+}}$ are the concentration and volume of the cerium solution respectively, and n_B is the number of B-cations in the titrated compound ($n_B = 3$ for $LaSr_3Fe_3O_{10-x}$).

4. Results and discussion

The current chapter presents the main findings obtained in this work. In part one (4.1), main results on the synthesis, crystal structure and thermal stability of $La_{2-x}Nd_xLiHO_3$ are described, which are published in **Paper I** and **Paper II**. Further, as the halide salt flux approach gave the opportunity to prepare large sample quantities, neutron spectroscopy was employed together with DFT to understand the chemical bonding and diffusion in La_2LiHO_3, which is published in **Paper III**. In addition, key results obtained during the preliminary work on utilizing PEDT for determination of hydride anion positions in La_2LiHO_3, local structure investigations by neutron PDF, and investigations of chemical bonding and momentum distribution by NCS in La_2LiHO_3 is included.

In part two (4.2) key findings on the crystal and magnetic structure of $LaSr_3Fe_3O_9$ is given together with investigations of the oxygen non-stoichiometry of $LaSr_3Fe_3O_{10-x}$, which is published in **Paper IV**. In addition, preliminary results of the investigations of the potential $LaSr_3Fe_3H_{1.1}O_{8.9}$-oxyhydride is included, emphasizing the connection between the two sections. Finally, note that the most important findings of this work are summarized and put into a broader context in section 5.

4.1   The $La_{2-x}Nd_xLiHO_3$-system

In the beginning of this PhD-work (August 2014) very few oxyhydrides had been discovered and explored; which is emphasized by the overview in Figure 19. Notably, at an early stage of this project we rediscovered the PhD work by Schwartz on the synthesis of Ln_2LiHO_3 (Ln = La, Ce, Pr and Nd) by a halide salt flux approach. As no further work on these compounds had been communicated until that point, our goal became to explore them and the halide salt flux method in more detail. However, already in 2016, Kobayashi *et al.* published on hydride anion conductivity and synthesis of $La_{2-x-y}Sr_{x+y}LiH_{1-x+y}O_{3-y}$ by a high-pressure approach.[19] Per today (March 2019), more than nine studies on this specific system, both experimental and computational, are reported whereof three are from this work.
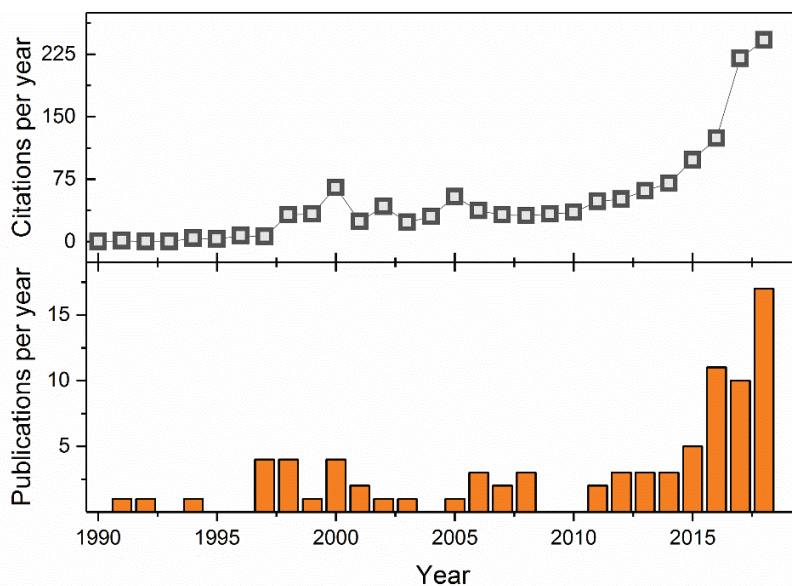
Figure 19: Number of citations per year (top) and publications per year (bottom) found by searching for "oxyhydride" as topic on Web of Science (February 2019, publications from 2019 is not included). Harald Schwartz thesis from 1991 is included in addition.

4.1.1 Synthesis of La$_{2-x}$Nd$_x$LiHO$_3$ by the halide salt flux approach

4.1.1.1 Practical consideration of the halide salt flux method

Using a halide salt flux to grow and stabilize the oxyhydrides, as reported by Schwarz back in 1991, is superior to the high-pressure method with respect to obtained sample quantity, and the reduced complexity of the method (section 2.5.2). Schwarz used stainless-steel crucibles in his experiments. The crucibles were loaded with the precursors (Ln_2O_3, LiH and LiCl) in an argon filled glove box and closed by hammering a conical plug into the opening. The closed crucibles were subsequently put into a protective steel tube, again inserted to a glass tube and closed under vacuum, before heat treatment for 15–48 hours in the temperature interval 690–800 °C.[74]

Initially, in this work we constructed a re-usable stainless-steel ampoule for synthesis of oxyhydrides, Figure 20. The ampoule was long with a copper washer for sealing and designed for use in a vertical tube furnace. The treads on the ampoule were kept outside the hot zone to ensure smooth opening and unloading after ended heat treatment. The first ampoules were contained in evacuated quartz tubes as a safety precaution. At a later stage in the work, it was concluded that the heating could be done directly in air below 700 °C. Inspection of the ampoules after heating at 750 °C and higher showed that we operated close to the limit of the ampoules due to the wear on the ampoule. Additionally, copper melts at 1085 °C, thus at 800 °C we operate close to temperatures where the copper washer becomes ductile.

Figure 20: Stainless-steel ampoules after use (left), unused (middle and right) and a niobium crucible to be inserted in the ampoules.

After ended synthesis, Schwarz used a 1:1 water:methanol mixture to remove the halide salt flux. Due to the high solubility of lithium chloride in methanol, we disregarded the use of the mixture and instead carried out the washing in pure methanol. The sample, a hard lump, was frequently stuck inside the crucible, and therefore methanol was added to the crucibles to dissolve lithium chloride. Then the sample would detach and could be transferred to a beaker. The reaction between methanol and the sample was an exothermic reaction where the excess lithium hydride reacted with methanol, releasing hydrogen gas. However, the reaction was not very vigorous, and the procedure could be carried out in a safe manner in a fume hood. After the washing, the methanol was decanted, and the washing procedure was repeated two more times before the product was dried and transferred to the glovebox for storage. The washing was conducted outside the glovebox as the compounds were found to be sufficiently stable in air.

The first batches of La_2LiHO_3 were synthesized directly in the stainless-steel ampoule. However, to reduce the risk of impurities from the stainless-steel ampoule, we implemented tantalum and niobium inserts to the stainless-steel bodies (10 mm in diameter, 50–70 mm tall) to contain the salt flux. Still this method only allowed for synthesis of about 1 g La_2LiHO_3. As the project at this stage started to go into neutron scattering experiments, large sample quantities were needed and hence the synthesis method needed to be scaled up.

A large stainless-steel ampoule, capable of containing eleven tantalum or niobium crucibles (same size as in previous ampoule), were developed to be heated directly in air in larger muffle furnaces, Figure 21. Alternatively, we used a larger crucible instead of the small ones. The set-up then allows for screening of oxyhydrides in different crucibles simultaneously, or large-scale synthesis.

At most, 25 g La_2LiHO_3 was prepared in one batch with this ampoule, and larger quantities is considered as feasible.

Figure 21: The large stainless-steel ampoule used for synthesis of larger quantities of oxyhydride. Top form left: The ampoule (before use), inset to contain small crucibles with one niobium crucible, large and medium sized tantalum crucibles. Bottom: Lid (left) and copper seal (right) for the ampoule.

4.1.1.2 Ratio between reactants and flux in the halide salt flux method

One of the first subjects addressed in this work was the effect of the ratio between the reactants La_2O_3, LiH and the flux, LiCl, to obtain La_2LiHO_3. In line with the work of Schwarz, LiCl was used as flux, while the La_2O_3:LiH ratio was varied. A La_2O_3:LiH molar ratio of 1:1 resulted in a mixture between La_2LiHO_3 (orthorhombic variant) and La_2O_3 at 750 °C, while the ratios 1:2−1:8, gave only the desired phase, orthorhombic La_2LiHO_3. For standard synthesis 1:4 molar ratio of La_2O_3:LiH was chosen. The quantity of flux used relative to the reactants was also evaluated. No change in the product was observed for 60, 100 and 200 mass % (mass % of the weighed precursors, Ln_2O_3 and LiH). 60 mass % was used for all experiments in the La_2LiHO_3 system, while for the $La_{2−x}Nd_xLiHO_3$ system, 100 mass % was used to ensure mixture when two different oxides was used.

4.1.1.3 Effect of halide salt flux temperature for oxyhydride synthesis

Within the capabilities of the halide salt flux method as reported by Schwartz, La_2LiHO_3 was prepared without impurities, whereas Nd_2LiHO_3, Ce_2LiHO_3 and Pr_2LiHO_3 were never obtained as single-phase products.[74] For these reasons, we set out to synthesize selected samples with nominal composition $La_{2-x}Nd_xLiHO_3$ ($0 \leq x \leq 2$), with the purpose to improve on our understanding of the phase stability of these compounds.

Selected $La_{2-x}Nd_xLiHO_3$ ($0 \leq x \leq 2$) compositions were synthesized between 600 and 800 °C, following the standard experimental conditions with respect to reactant ratio and flux quantity (section 4.1.1.2). The lower temperature limit was set by the melting temperature of lithium chloride (605 °C).[137] Obtained samples were analyzed by means of Rietveld refinements of XRD and mass percent of targeted product was plotted versus flux temperature, Figure 22. Similarly as Schwarz, we only obtain La_2LiHO_3 without impurities up to 750 °C, while all other compositions contain impurities of LnHO and/or Ln_2O_3 at all explored reaction temperatures (600, 650, 700, 750 °C). From our experiments, two trends are clear, the amount of impurities increases with (1) increasing neodymium content and (2) increasing flux temperature.
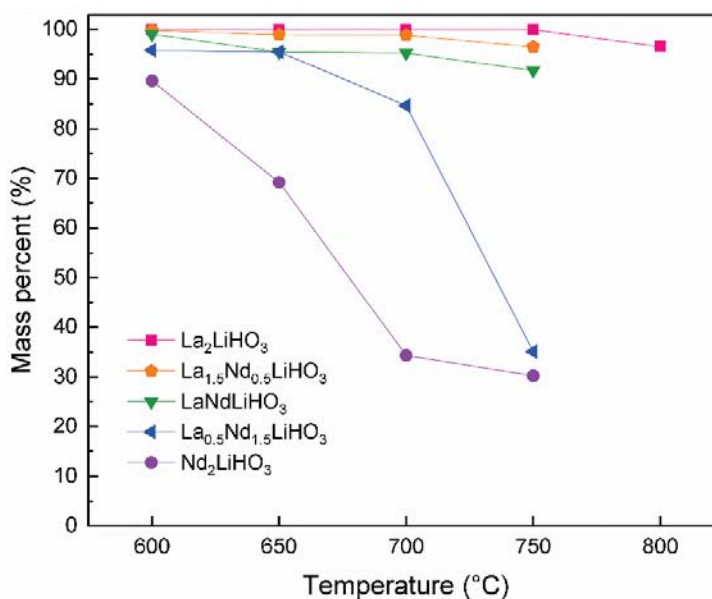

Figure 22: Quantity (mass %) of desired phase $La_{2-x}Nd_xLiHO_3$ ($0 \leq x \leq 2$) versus flux temperature during synthesis. Reused with premission from The Royal Society of Chemistry.[138]

By considering these two trends, we hypothesize that the oxyhydrides are formed at lower temperatures than the used flux temperature during synthesis; consequently, upon cooling of the flux. While at the reaction temperature other phases such as LnHO may be formed and reactants

may undergo crystal growth. These factors may explain the trends reported in Figure 22. Based on these considerations, we decided to conduct a new series of experiments to verify or reject our theory, based on Nd_2LiHO_3 as this compound had shown to be most challenging to prepare.

To verify whether the oxyhydrides mainly are formed during cooling, we decided to cool a synthesis batch aimed to become Nd_2LiHO_3 very slowly from 650 °C, Table 9. From previous experiments we expect about 30 mass % of impurities at 650 °C (Figure 22). In contrast to our expectations, we find no sign of impurities. This indicate that the oxyhydrides are not formed at high temperatures, rather at lower temperatures during cooling.

Table 9: Conditions for conducted experiments and the products from the synthesis. The quantities are obtained from Rietveld refinements. The quenched sample was taken directly from the furnace at 650 °C into cold water. Reused with premission from The Royal Society of Chemistry.[138]

Temperature	Flux	Hold	Cooling	Products
650 °C	LiCl	48 h	96 h	100 mass % Nd_2LiHO_3
650 °C	LiCl	48 h	Quenched	77.4 mass % Nd_2O_3
				22.6 mass % NdHO
700 → 550 °C	LiCl	48 h, 48 h	2 h, 3 h	70.5 mass % Nd_2LiHO_3
				29.5 mass % Nd_2O_3
550 °C	LiCl	48 h	5 h	96.3 mass % Nd_2LiHO_3
				2.7 mass % NdHO
				1.0 mass % Nd_2O_3
500 °C	LiCl	48 h	5 h	100 mass % Nd_2LiHO_3
500 °C	LiCl-KCl	48 h	5 h	100 mass % Nd_2LiHO_3
				+ KCl
400 °C	LiCl-KCl	48 h	5 h	55.9 mass % Nd_2O_3
				35.6 mass % Nd_2LiHO_3
				8.5 mass % NdHO

To get a clearer understanding of which phases that are present at 650 °C, we quenched a synthesis batch, targeted to become Nd_2LiHO_3, by taking the stainless-steel ampoule directly out of the furnace at 650 °C and into cold water. Strikingly, we observe no Nd_2LiHO_3 in the sample, only Nd_2O_3 and NdHO. The experiment gives a clear indication of the phases present in the flux at 650 °C and is a clear sign that the oxyhydride indeed is formed during cooling.

To this point we had restricted the lower temperature limit by the melting temperature of lithium chloride of 605 °C. As our experiments to this point suggest that the oxyhydride is formed during cooling, *i.e.* below the melting temperature of lithium chloride, we attempted to synthesize Nd_2LiHO_3 at 500 and 550 °C. In accordance with Figure 22 and our theory, we observe a decreasing amount of impurities at 550 °C, and at 500 °C we obtained Nd_2LiHO_3 completely without impurities for the first time by the halide salt flux method. Thus, these experiments illustrate that low temperatures are needed to synthesize oxyhydrides. Additionally, it is obviously that lithium chloride serves as a flux and provides sufficiently high ionic mobility of the reactants even as a solid.

To investigate another part of our theory, possible crystallite growth of the reactants, we exposed the reactants needed to form a Nd_2LiHO_3 sample to the LiCl flux first at 700 °C for 48 hours, then then cooled it to 550 °C and held it there for 48 hours. From the previous experiments, we know Nd_2LiHO_3 synthesized at 700 °C contains 70 mass % impurities. While for a sample synthesized at 550 °C, we expect almost no impurities. What we observe in the current experiment is something in between. We interpret this as an indication of particle growth of the reactants at high temperatures. At lower temperatures, the crystallites are converted to Nd_2LiHO_3, but as the reactant crystallites are large, they are not fully converted within the 48 hours duration of the experiment.

4.1.2 Revisiting the crystal structure of $La_{2-x}Nd_xLiHO_3$

4.1.2.1 Crystal structure investigations by neutron diffraction

Knowledge of crystal structure and crystal structural analysis are a crucial tool in the development and understanding of functional materials. Although the crystal structure of Ln_2LiHO_3 (Ln = La, Ce, Pr, Nd) has been reported previously, some selected aspects of the atomic arrangement are considered in detail in this work.[74] For phase identification for all samples prepared in this work XRD in the home laboratory was used. However, describing the accurate relative atomic positions of the light atoms, hydrogen and lithium, is not possible with X-rays due to the heavy lanthanide element and the low scattering power of the light elements (section 3.2.1).

In this work, neutron diffraction has been used to address accurate crystal structure determination of oxyhydrides. Four samples have been measured by neutron diffraction at the POLARIS instrument at ISIS pulsed neutron and muon source; one hydrogen containing sample and three deuterated samples.[139] The first deuterated sample prepared during this work was not completely deuterated (~75 %), but the two others were deuterated above 90 %. In addition, $LaNdLiHO_3$ was measured at the PUS instrument at Institute for Energy Technology.[140]

Based on Rietveld refinements of diffraction experiments we describe the crystal structure of $La_{2-x}Nd_xLiHO_3$ (illustrated in Figure 23), and structural details for La_2LiDO_3 (deuterium variant of La_2LiHO_3) is given in Table 10. The crystal structure of La_2LiHO_3 is a RP1-type crystal structure with an orthorhombic distortion due to the ordering of oxide and hydride anions. The crystal structure consists of layers of single perovskite slabs, separated by one half rock salt layer. The perovskite slab is built up by corner-connected lithium octahedra with oxide anions on the axial positions, and oxide and hydride anions ordered on the equatorial positions.

The orthorhombic crystal structure of La_2LiHO_3 reported by Kobayashi *et al.* was without vacancies and anion mixing, *i.e.* hydrogen on oxygen position and *vice versa*.[19] On the other hand Iwasaki *et al.* observed mixing of oxygen and hydrogen for Pr_2LiHO_3 and Nd_2LiHO_3 (section 2.5.1.1).[75] Kobayashi *et al.* also reported that La_2LiHO_3 is an anion conductor. Diffusion

of anions in the ordered crystal structure of La_2LiHO_3 could manifest itself as mixing of oxide and hydride anions. This option was therefore considered for La_2LiHO_3 when analyzing the neutron diffraction data.

Table 10: Crystallographic data of $La_2LiD_{0.745}H_{0.255}O_3$ in space group _Immm_ [$a =$ 3.571521(41) Å, $b =$ 3.763532(44) Å, and $c =$ 12.97854(15) Å] from PND. U_{iso} is the isotropic thermal displacement factor. Reused with premission from American Chemical Society.[141]

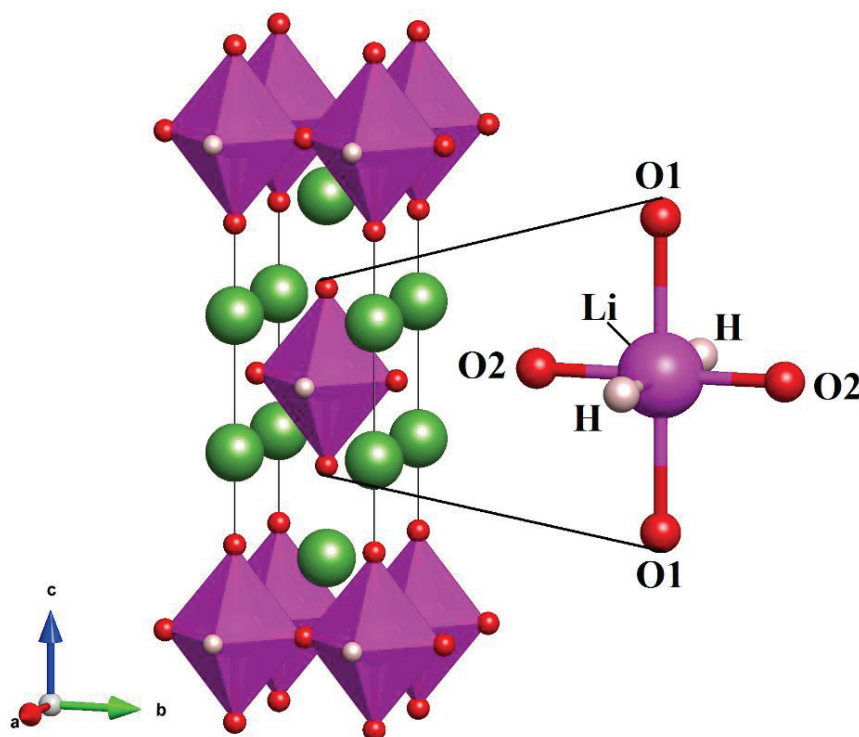| Atom	Wyckoff	x	y	y	Occupancy	U_{iso} (Å²)
La	4i	0	0	0.363344(21)	1	0.00903(7)
Li	2a	0	0	0	1	0.01553(34)
D	2b	0.5	0	0	0.745(1)	0.02343(28)
H	2b	0.5	0	0	0.255(1)	0.02343(28)
O1	4i	0	0	0.176738(31)	1	0.01216(9)
O2	2d	0.5	0	0.5	1	0.01216(9)

Figure 23: Crystal structure of $La_{2-x}Nd_xLiHO_3$. The compounds take an orthorhombic crystal structure with space group _Immm_. The purple octahedral corresponds to the perovskite slab, while the region between the perovskite slabs along the _c_-axis corresponds to the rock salt layer. Green atoms are lanthanide, purple atoms are lithium, red atoms are oxygen and white are hydrogen. The coordination polyhedra illustrates the octahedral coordination of lithium.

Careful analysis show that all occupancies are very close to unity. If anion mixing is present, the fraction is 1−4 % at most, and only present at the equatorial positions. No sign of mixing for the

axial oxygen was observed. In addition, the deuterated samples measured at the POLARIS instrument were investigated from room temperature to 400 °C and no variation with temperature of the occupancies/anion mixing was observed.

4.1.2.2 Observing hydride anions by electron diffraction

As addressed in section 3.2.1.1, PEDT is an alternative technique for structural determination to X-ray and neutron diffraction which circumvent many of the disadvantages with neutron diffraction (sample quantity, isotope considerations, access to neutron source), and still allows refinement of fine structural details such as oxygen occupancies and positions of light elements like hydrogen.[111, 117-118] For these reasons, we aimed to evaluate the feasibility of PEDT as an alternative probe to determine hydride anion positions and for structural determination of oxyhydrides in collaboration with the CRISMAT institute in Caen.

The motivation for these experiments is two-fold. First, it would be valuable to have an alternative technique to neutron diffraction allowing complete structural determination of oxyhydrides. Second, determination of hydrogen has not been done in the presence of elements heavier than cobalt. This experiment involving the heavy element lanthanum in combination with hydrogen, would be the first of its kind and could extend the capabilities of PEDT.

Three crystallites of La_2LiHO_3 were measured with a precession angle of 1.5°. However, the analysis in this section will deal with one of the crystallites as all showed the same features. An image of the crystallite described here is presented in Figure 24 while experimental details are given in Table 11. The three-dimensional diffraction intensities obtained from PEDT were indexed to the same unit cell as reported and found by other methods in this work.[19, 74] Based on Fourier maps, all atomic positions were identified, including the hydride anion position, and a crystal structure identical to that found by neutron diffraction was refined by a kinematical approach to the PEDT data in Jana2006.[142]

Although we had solved the crystal structure at this stage, accurate atomic position, occupancy and thermal displacement parameters, cannot be extracted accurately from kinematical refinements of PEDT (section 3.2.1.1). To achieve a trustworthy refinement, dynamical refinements were carried out in Jana2006 following the guidelines given by Palatinus *et al*.[111, 142] In the refinements, negative thermal displacement parameters were encountered for the hydrogen position, Table 12. Further, the thermal displacement parameter of the equatorial oxygen position was higher than expected. In addition, high residual scattering density was observed in Fourier maps. Although all reasonable parameters were refined, a satisfactory refinement was not possible to achieve with the collected data. This is emphasized by the R_{wp} values that is about a factor two larger than expected, Table 11.[111] All these observations indicate that there is a problem with the model.
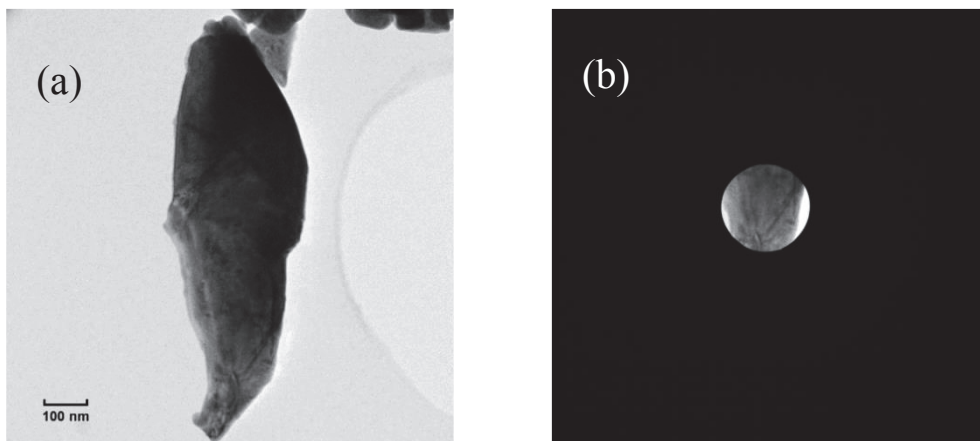
4. Results and discussion

Figure 24: (a) One of three crystallites measured by PEDT. (b) Area of the crystallite measured for diffraction.

Table 11: Experimental details for collection of PEDT with Nanomegas Digistar precession module and a Gatan Orius 200D CCD camera with an 80 cm camera distance on one crystallite.

	PEDT
Microscope	JEOL 2010
Temperature	96 K
λ	0.0251 Å
Acceleration voltage	200 keV
Precession angle (φ)	1.5°
Number of frames	91
Angular domain (min$-$max)	-51$-$45.5
Limiting indices	$-6 \leq h \leq 6$
	$-5 \leq k \leq 5$
	$-23 \leq l \leq 23$
Completeness considering a resolution of 0.7 $sin(\theta)/\lambda$	74.9 %
Number of measured reflections	4012
Number of independent reflections (I > 3σ)	2027
Number of independent observed reflections (I > 3σ)	1407
g^{max} (Å^{-1}), S_g^{max} (matrix), S_g^{max} (refine), R_{SG},	2; 0.01; 0.1; 0.4
Refined parameters	99
R_{wp}	23.26 %

Table 12: Crystallographic data of La$_2$LiHO$_3$ in space group *Immm* [*a* = 3.6745 Å, *b* = 3.7209 Å and *c* = 13.2968 Å] from PEDT of one crystallite. U_{iso} corresponds to the isotropic thermal displacement parameter.

Atom	Wyckoff	x	y	y	U_{iso} (Å^2)
La	4i	0	0	0.36290(11)	0.0135(5)
Li	2a	0	0	0	0.043(13)
H	2b	0.5	0	0	-0.012(6)
O1	4i	0	0	0.1777(7)	0.0195(18)
O2	2d	0.5	0	0.5	0.049(5)

Based on this, we believe that twin crystals, with domains rotated by 90° with respect to each other were measured. Given this scenario, taking in to account the poor resolution of electron diffraction and the close match of the a- and b-unit cell parameters, may $e.g.$ the (101)- and (011)-reflection overlap without it being possible to observe a splitting. As shown in Figure 25, no direct sign of split reflections is detected in the diffraction patterns. The twinning then mixes the intensity between overlapping reflections during integration and this is most likely the origin of the encountered issues with the refinements.
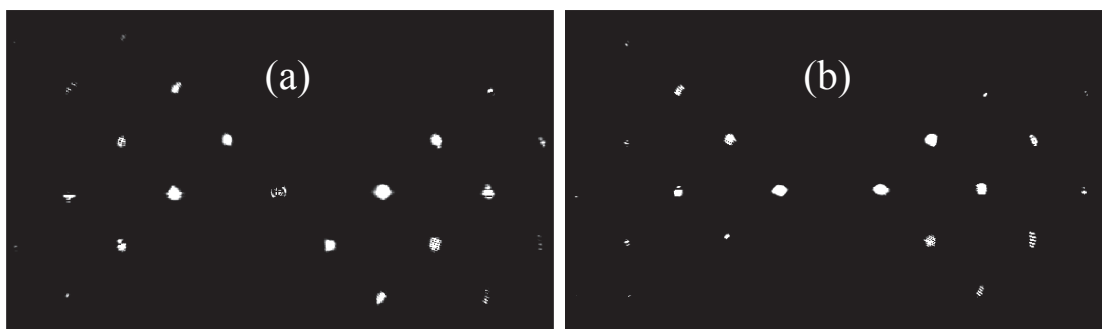

Figure 25: Reconstructed map of the *hk0*-reflections (a) and *hk1*-reflections (b) from PEDT measurements on La$_2$LiHO$_3$. If twinning by two crystal is present, it is not possible to observe as we do not observe any split reflections.

For this reason, we cannot state that our attempt to observe hydride anions by PEDT was successful. Although a satisfactory dynamic refinement was unsuccessful, it must be noted that within the kinematical approach, the crystal structure was solved from the data giving structural parameters in line with those extracted from neutron diffraction. However, this is by a biased approach as we were aware of the solution we searched for, and therefore not trustworthy with respect to the presence of hydride anions in the system. Still, we have demonstrated that crystal structure solution of oxyhydrides by PEDT is feasible, and in systems that don't display twinning, dynamical refinements may be carried out to validate the presence of hydride anions.

4.1.2.3 Local structure by neutron PDF

The crystal structure of La$_2$LiHO$_3$ has been investigated thoroughly, yet there are no reports on the local structure. As discussed in section 4.1.2.1, La$_2$LiHO$_3$ is an anion conductor and diffusion of anions may lead mixing of anions on the anion sites in the crystal structure, and thus lead to disorder. We therefore addressed this by neutron PDF measurements at the POLARIS instrument at ISIS pulsed neutron and muon source between room temperature and 400 °C. Large-box RMC refinements (section 3.2.2.2) allow us to detect ordering of atoms at long and intermediate length scales, even in cases where there is no crystallographic order.[124, 126] To reduce the incoherent background, we investigated the deuterated variant La$_2$LiDO$_3$, which Rietveld refinements showed to have a deuterium content of 95 %.

4. Results and discussion

Although Rietveld refinements (section 4.1.2.1) suggested that mixing between oxide and hydride anions was not present in the system, we performed RMC refinements both with and without allowing swaps between anions of the room temperature data set. The two fits gave comparable results and analysis of the accepted number of swaps tells us that no preference for the site is there. It means that atoms keep swapping and it does not improve the fit. The option of swapping was therefore disregarded in the further analysis.

Considering the structure obtained from RMC refinements at room temperature, no significant deviation from the average crystal structure and the atom clouds are in correspondence with the values for the thermal displacement parameters, Figure 26. At 200 °C, we observe a change in the atomic clouds of the collapsed cell. The atomic clouds form circular shapes without atoms in the centre, Figure 26. This change is clearer at 400 °C, where the circles increase in size. The behaviour suggest a change in the local structure, while the average crystal structure is intact. As PDF is an unbiased method and the behaviour is in accordance with the experimental data, we believe the behaviour is real and not an artefact of the data.
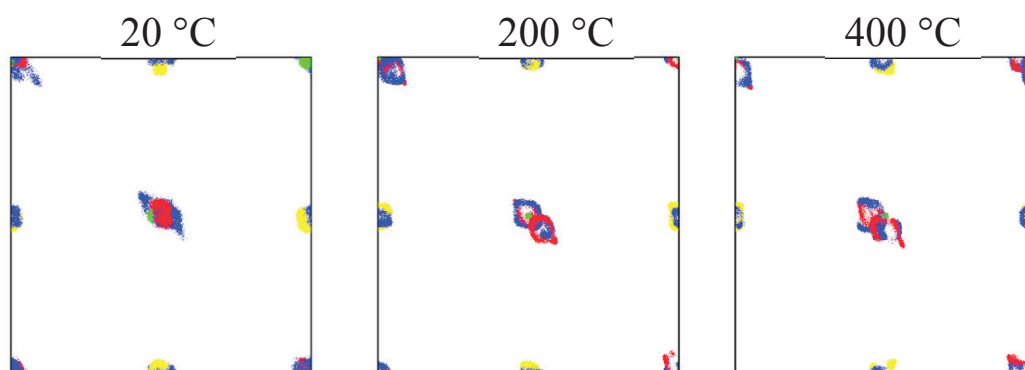

Figure 26: Visualization of the collapsed cell at room temperature, 200 and 400 °C. The atoms correspond to lanthanum (red), lithium (green), hydrogen (yellow) and oxygen (blue). At 200 and 400 °C, lanthanum, hydrogen and oxygen display circular shaped atomic clouds.

The behaviour is observed for all atoms except lithium. The lithium position seemingly becomes more localized and is smaller at 200 and 400 °C than at room temperature. This is not in accordance with the behaviour of the other elements or the extracted thermal displacement factors from Rietveld refinements. In addition, the lithium position from neutron PDF violates the I-centring (body centring) of the space group (*Immm*). If this was the case, additional reflections should have been observed by electron diffraction or neutron diffraction, which is not the case.

However, considering the neutron scattering cross sections of the constituent atoms in the compound, lithium has the smallest scattering cross section by a factor of 10 (0.454 barn compared to 8.53, 5.592 and 4.232 barn for lanthanum, deuterium and oxygen, respectively).[143] Based on these facts, we suggest that the deviating behaviour of lithium is due to reduced contrast in the

experiment and we therefore suggest that lithium actually displays similar behaviour to the other atoms and the lack of contrast stops us from observing it.

4.1.3 Thermal stability of La$_{2-x}$Nd$_x$LiHO$_3$

4.1.3.1 Thermal stability and unit cell dimensions

The thermal stability and unit cell dimension variations of La$_{2-x}$Nd$_x$LiHO$_3$ versus neodymium substitution were addressed by combined TGA, DSC, and MS, as well as XRD, SR-XRD and DFT. Upon heating in oxygen atmosphere an oxidation of the oxyhydride occur. For La$_2$LiHO$_3$ the oxidation process is according to TGA-DSC determined to be initiated at about 450 °C, Figure 27. The mass increase corresponds well with the hydride anion in La$_2$LiHO$_3$ being replaced by one half oxide anion. Further, MS data recorded simultaneously with TGA-DSC, shows that the oxidation process is accompanied with a release of water, Figure 27. This observation is directly supporting the existence of hydride anions in the compound, and in combination with XRD analysis, which show that La$_2$LiO$_{3.5}$ (discussed in section 4.1.3.2) is formed during the oxidation process, we suggest the flowing reaction for the oxidation:

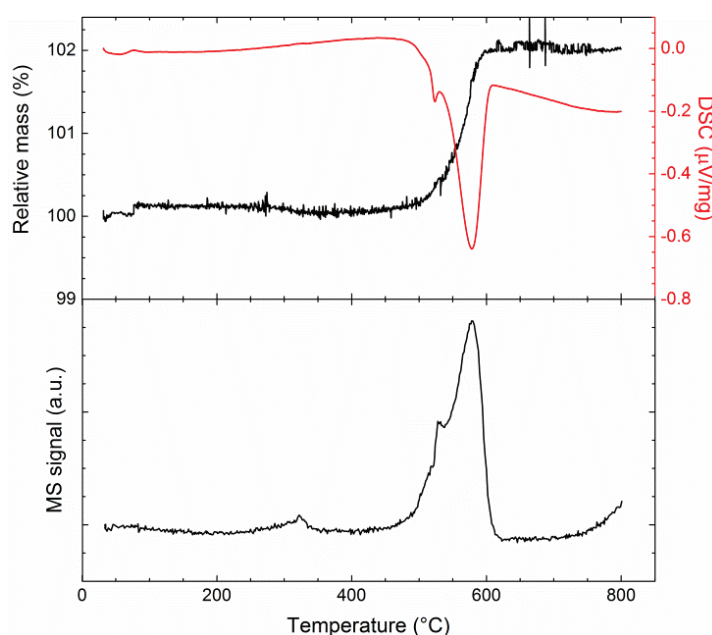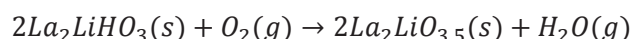$$2La_2LiHO_3(s) + O_2(g) \rightarrow 2La_2LiO_{3.5}(s) + H_2O(g)$$

Figure 27: Combined TGA, DSC (top) and MS of mass 18 (bottom) of La$_2$LiHO$_3$ heated in O$_2$-atmosphere (5 °C min^{-1}). A significant mass increase is observed at ~450 °C, corresponding to the oxidation of La$_2$LiHO$_3$ to La$_2$LiO$_{3.5}$. The MS signal identifies the water release associated with the oxidation. Reused with premission from American Chemical Society.[141]

It should be noted that we typically observed a mixture of $La_2LiO_{3.5}$ and La_2O_3 after oxidation. In this case we assume that the unaccounted lithium form lithium oxide or lithium hydroxide, which is not detected by XRD due to the lithium compound's low scattering power or poor crystallinity.

SR-XRD was used to gain additional insight to the decomposition and oxidation of the oxyhydride. La_2LiHO_3 was packed in an open quartz capillary and heated from room temperature to 800 °C at the BM01 at ESRF. The development of the oxidation process was understood from analysis of the in-situ data by surface Rietveld refinements (section 3.2.2.1). The unit cell parameters are observed to evolve linearly, as expected from thermal lattice expansion, to about 350 °C, Figure 28. The unit cell parameters of La_2LiHO_3 evolve in a monotonic manner until 350 °C, Figure 28. Above 350 °C, the a- and b-unit cell parameters start to go towards each other, as illustrated by the a/b-ratio which starts to go towards unity. Although no symmetry change was observed, the change in a/b-ratio suggests that the crystal structure is propagating towards a more tetragonal unit cell.
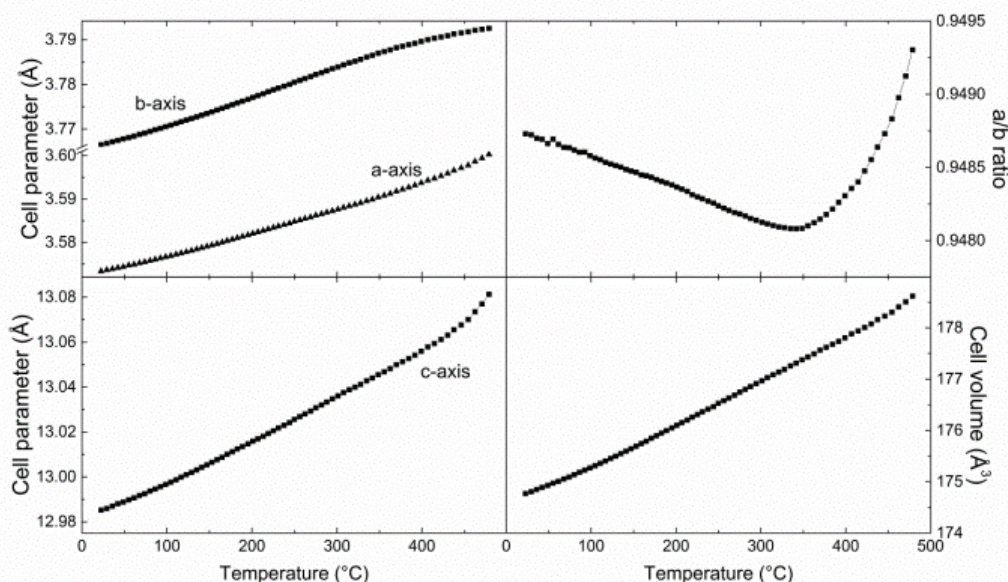

Figure 28: Evolution of the unit cell parameters of La_2LiHO_3 from surface Rietveld refinements during heating in an open quartz capillary with a heating rate of 2 °C min^{-1}. Reused with premission from American Chemical Society.[141]

Interestingly, combined TGA-DSC experiments reveal that the thermal stability of the oxyhydrides decreases with increasing neodymium content with an approximate decomposition temperature difference of ~80 °C between La_2LiHO_3 and Nd_2LiHO_3, Figure 29 a. Overall, this finding is consistent our earlier observations (section 4.1.1.3) regarding maximum flux temperature during synthesis; *i.e.* that La_2LiHO_3 can be synthesized at significantly higher temperature than Nd_2LiHO_3. Notably, there is no one-to-one correlation between the

decomposition temperatures obtained from TGA and those indicated from the flux experiments due to the very different nature of the two media (oxygen atmosphere versus a LiCl flux with excess lithium hydride). However, similar trends are observed independently of method and conditions.

The unit cell volume (V) of the orthorhombic RP1 $La_{2-x}Nd_xLiHO_3$ versus x is included to Figure 29 a. A steady contraction of the unit cell volume is observed with increasing neodymium substitution, in line with the lanthanide contraction and Vegard's law for a solid solution.[144-145] Furthermore, DFT calculations, Figure 29 b, shows the heat of formation (ΔH_f) of the oxyhydrides from its oxide (La_2O_3, Nd_2O_3) and hydride (LiH) components, to be less exothermic with increasing neodymium content. Based on these observations, it is tempting to anticipate or predict that the thermal stability of this oxyhydride family in general is decreasing with reduced size of the lanthanide-cation. To evaluate the stability of Ln_2LiHO_3 containing heavier lanthanides, we performed DFT calculations on Sm_2LiHO_3, assuming the compound would take a similar structure as the other Ln_2LiHO_3 oxyhydrides. As negative phonon frequencies was encountered, we state that the compound is unstable and that neodymium is the heaviest lanthanide to form Ln_2LiHO_3 oxyhydrides.
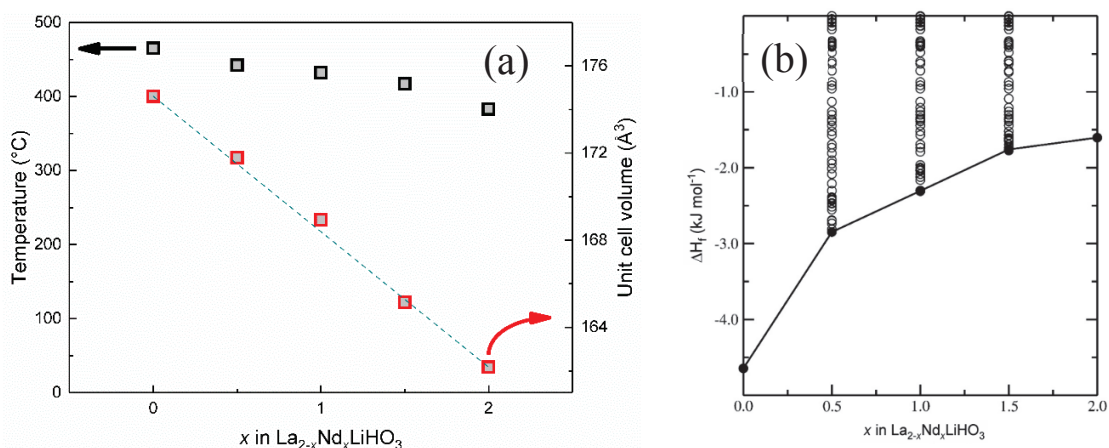

Figure 29: (a) Decomposition temperature (black) from TGA measurements in O₂ atmosphere and unit cell volume for selected neodymium substitutions (x) of La₂₋ₓNdₓLiHO₃ synthesized at 600 °C in LiCl salt flux. The green dotted line illustrates Vegard's law; a linear relationship in cell volume for intermediate compositions in a solid solution. (b) Calculated heat of formation (ΔH_f) of La₂₋ₓNdₓLiHO₃ ($x = 0, 0.5, 1.0, 1.5, 2$) from the binary constituents (La₂O₃, Nd₂O₃, LiH) as a function Nd concentration (x). The open circles are corresponding to the energetics of possible different atomic arrangements of La/Nd in the matrix; all the crystal structures are generated with random crystal structure generator approach. Reused with premission from American Chemical Society and The Royal Society of Chemistry.[138, 141]

4.1.3.2 Crystal structure of oxidized derivative – La$_2$LiO$_{3.5}$

In TGA experiments we observed La$_2$LiHO$_3$ to release water during oxidation. The main product from the oxidation was identified to be La$_2$LiO$_{3.5}$ by XRD analysis. La$_2$LiO$_{3.5}$ is reported by Attfield and Férey to take a tetragonal RP1-type crystal structure.[146] However, Rietveld refinements using the tetragonal crystal structure description gave unsatisfying results. The reflections indexed as (110), (112) and (114) in the tetragonal cell, were clearly split into two reflections in the measured diffraction pattern of the oxidized samples, thus the fit was not of acceptable quality. An orthorhombic supercell expanding along the diagonals of the tetragonal cell with the basis [(1,1,0), (1,−1,0), (0,0,1)] and with space group *Fmmm* was identified by ISODISTORT to describe the crystal structure satisfactory, Table 13 and Figure 30.[147] The distortion distinguishes the orthorhombic from the tetragonal La$_2$LiO$_{3.5}$ and we consider it as a new polymorph. The orthorhombic crystal structure of La$_2$LiO$_{3.5}$ is strongly related to both the tetragonal crystal structure reported by Attfield and Férey, and to the orthorhombic La$_2$LiHO$_3$ oxyhydride. As the RP1-framework of La$_2$LiHO$_3$ remains upon oxidation, we consider the process to be topotactic. Similar to the crystal structure model reported by Attfield and Férey, we found all vacancies to be on the equatorial sites.
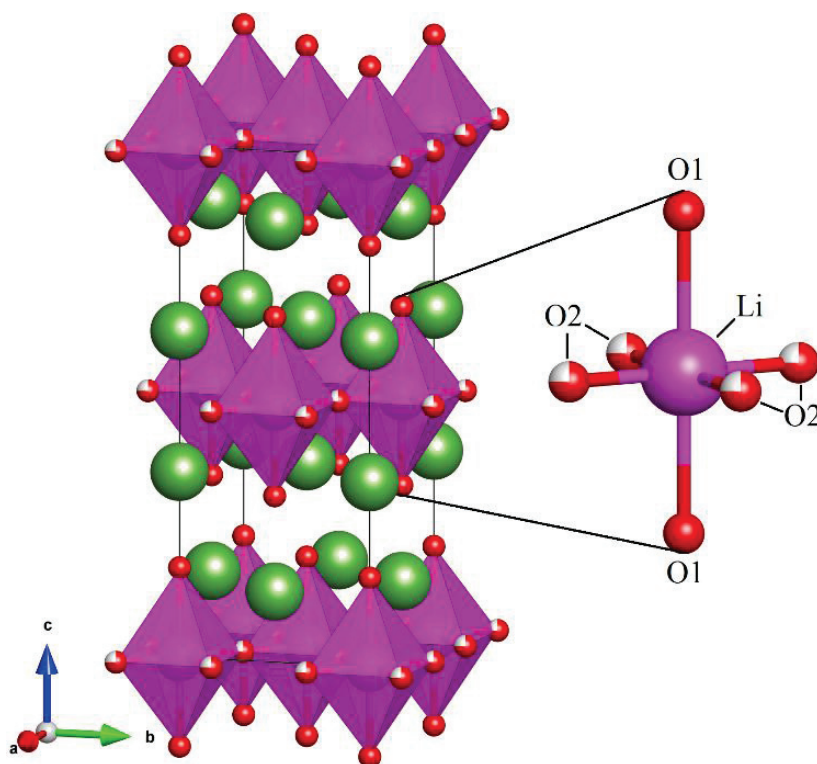

Figure 30: Illustration of the crystal structure of La$_2$LiO$_{3.5}$ (space group *Fmmm*). The atoms correspond to lanthanum (green), lithium (pink), hydrogen (white) and oxygen (red).

Table 13: Crystallographic information for La$_2$LiO$_{3.5}$ in space group *Fmmm* [*a* = 5.196(6) Å, *b* = 5.136(7) Å, *c* = 13.279(7) Å]. Same values for the atomic displacement parameters were used for lithium and oxygen atoms. *U$_{iso}$* refers to the thermal displacement parameter. Reused with premission from American Chemical Society.[141]

Atom	Wyckoff	*x*	*y*	*y*	Occupancy	*U$_{iso}$* (Å^2)
La	8i	0.5	0.5	0.637(7)	1	0.019(3)
Li	4a	0	0.5	0.5	1	0.02(2)
O1	8i	0.5	0.5	0.825(0)	1	0.02(2)
O2	8e	0.25	0.25	0.5	0.75	0.02(2)

4.1.3.3 Hydride anion diffusion in La$_2$LiHO$_3$ by QENS

After Kobayashi *et al*. observed hydride anion diffusion in La$_2$LiHO$_3$ in 2016, we were intrigued to pursue this further. In addition to computational efforts (section 4.1.5), we decided to conduct a QENS experiment (section 3.2.3.1) to directly observe and quantify hydride anion diffusion in La$_2$LiHO$_3$. As hydrogen is a strong incoherent scatterer, hydride anion diffusion would yield a strong QENS signal, thus QENS is ideal to study hydride anion diffusion in oxyhydrides.

Unfortunately, Kobayashi *et al*. do not give a lower temperature limit for hydride anion diffusion. However, they measure hydride anion conductivity between 200 and 300 °C, and their prototype battery with La$_2$LiHO$_3$ as hydride anion conducting electrolyte was tested at 300 °C.[19] Since we expected the hydride anion diffusion to show an onset at a low temperature we initiated our investigation by a QENS experiment at the OSIRIS instrument at ISIS pulsed neutron and muon source at low temperatures (13.5 to 500 K, experimental data from this experiment is not shown).[148] The instrument is well-known to supply high quality data suitable for diffusional analysis. However, the experiment showed no evolution or change in the QENS signal over the investigated temperature range. Thus, it was concluded that the diffusion behavior had an onset at higher temperatures.

To pursue the open question on the onset temperature of hydride anion diffusion, we conducted another experiment at the IRIS instrument (ISIS pulsed neutron and muon source), which yields similar resolution as the OSIRIS instrument.[149-150] The experiment at IRIS was conducted from room temperature to 527 °C and showed no further evolution in the QENS signal before 400 °C, where the signal increases strongly, Figure 31. Thus, above 400 °C La$_2$LiHO$_3$ show increased hydride anion mobility. Given the resolution of the IRIS instrument, a fitting of the obtained QENS spectra was not considered feasible, and the observed diffusional behavior could not be quantified.

Our studies show the onset of hydride anion diffusion to occur at higher temperatures than the temperature range where Kobayashi *et al*. displayed hydride anion diffusion. Therefore, we consider the hydride anion diffusion observed by QENS to not be the diffusional behavior that

give rise to the diffusional behavior observed by Kobayashi *et al*. We note that Kobayashi *et al*. observed hydride anion diffusion in both the tetragonal and orthorhombic variant of La_2LiHO_3. On the other hand, the temperature is in the range where we observe the oxyhydride to decompose in oxidizing atmosphere from TGA experiments (section 4.1.3.1). For the oxyhydride to be oxidized, transport of anions is a necessity. We therefore suggest that the increased QENS signal above 400 °C is most likely arising from increased hydride anion mobility associated with the decomposition and that we do not observe the diffusional phenomena described by Kobayashi.
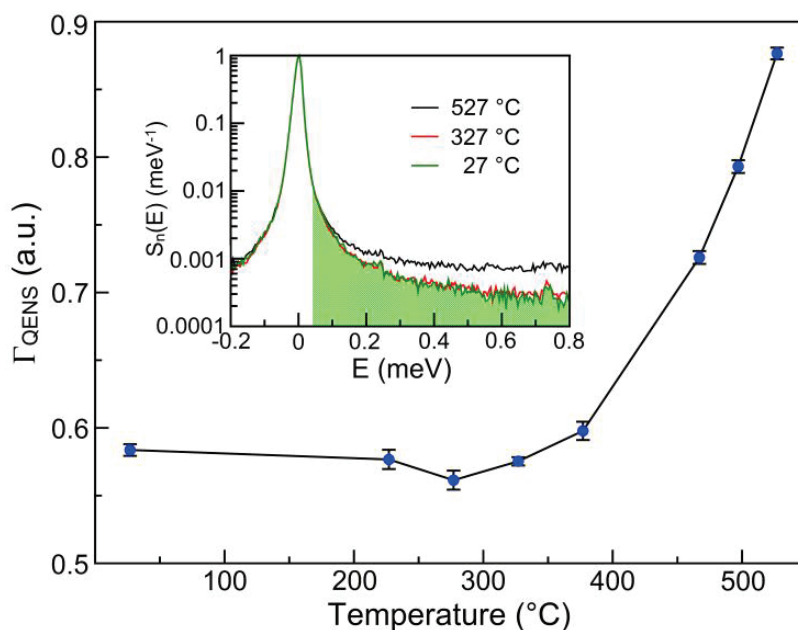

Figure 31: QENS spectra for La_2LiHO_3 measured at the IRIS instrument. An evolution of the broadening is observed above 400 °C. Γ_{QENS} refer to the integral (0.05−0.6 meV) beneth the QENS signal as illustrated by the green shaded region in the inset, and serves as a indication of the evolution of the QENS signal. Reused with premission from American Chemical Society.[141]

In summary, the QENS experiments gave no indications of diffusional behavior below the temperature associated with the decomposition of the compound. Thus, the diffusivity of hydride anions was assumed not to be in the timescales accessible with the OSIRIS and IRIS instruments due to inadequate resolution. Therefore, instruments with higher resolution or other techniques must be considered to quantify the diffusional behavior in La_2LiHO_3.

4.1.4 Crystal chemical considerations

With reference to section 2.5.1.1, La_2LiHO_3 is reported to crystallize both as an orthorhombic and a tetragonal variant.[19] By DFT calculations addressed their relative stability. Considering the total energy versus unit cell volume for the two crystal structures, Figure 32, the calculations state that

the orthorhombic crystal structure is most favorable. However, for higher unit cell volumes the calculations predict the tetragonal unit cell to become more favorable. Phonon calculation show that both polymorphs are dynamically stable.
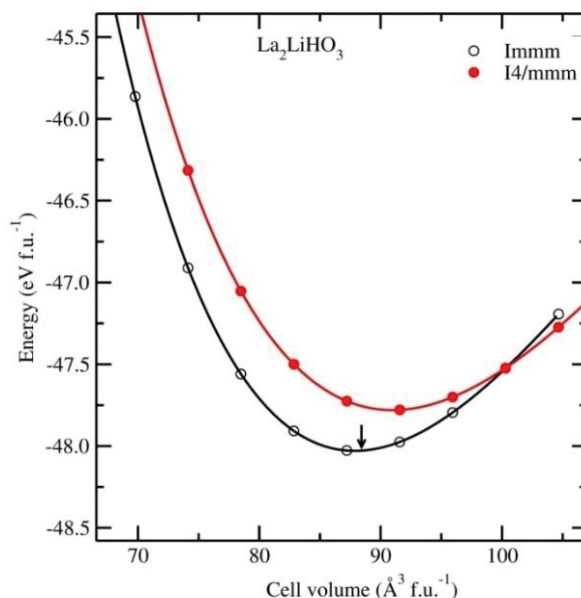

Figure 32: Calculated total energy (eV per formula unit) versus unit cell volume for the two different polymorphs of La_2LiHO_3 [orthorhombic (*Immm*) and tetragonal (*I4/mmm*)]. The arrow indicates the theoretical equilibrium at 88 Å³ f.u.⁻¹. Reused with premission from American Chemical Society.[151]

Atomic vibrations are amplified by increased temperature, and thus typically the unit cell volume of a compound expands with increasing temperature. As we observe from DFT calculations that the tetragonal crystal structure for La_2LiHO_3 is favorable at higher unit cell volumes, we can consider the possibility of a phase transition from the orthorhombic to the tetragonal crystal structure with increased temperature. This was experimentally carried out by SR-XRD (section 4.1.3.1). Before La_2LiHO_3 oxidized, we observed that the a/b-ratio started to go towards unity. However, no phase transition to a tetragonal symmetry was observed with increasing temperature. Thus, we conclude that temperature is not a parameter that may induce a phase transition.

Another parameter that may influence the unit cell volume is strain. This can be induced by substitution of atoms of different size or by introducing vacancies. Anion vacancies take more space in a crystal structure than anions. As tetragonal La_2LiHO_3 have a reported composition of $La_2LiH_{0.53}O_{3.21}\square_{0.26}$, the DFT calculations explain that this compound takes a tetragonal crystal structure as the vacancies increase the cell volume.[19] Further, this suggest that a possible explanation for the change in the a/b-ratio observed during oxidation by SR-XRD, could be

originated in partial oxidation of the oxyhydride as vacancies on the hydride position would elongate the unit cell along the a-axis (section 4.1.3.1).

If we consider a hypothetical solid-solution between the two end-members La_2LiHO_3 and $La_2LiO_{3.5}$, with a composition $La_2LiH_{1-x}O_{3+x/2}$, we would expect a linear change in cell volume with x according to Vegard's law, Figure 33.[144] This solid-solution is then considering partially oxidized La_2LiHO_3. As tetragonal La_2LiHO_3 has a larger cell volume than orthorhombic La_2LiHO_3, we can consider the tetragonal compound as part of this solid solution, thus it is partially oxidized. In other words, a formula of the type $La_2LiH_{1-x}O_{3+x/2}$ would be more appropriate for the tetragonal compound reported by Kobayashi et $al.$[19] We can now use Vegard's law to calculate the composition of tetragonal La_2LiHO_3. By assuming a linear relation in volume between orthorhombic La_2LiHO_3 and $La_2LiO_{3.5}$, we calculate a composition of $La_2LiH_{0.43}O_{3.28}\square_{0.28}$ for tetragonal La_2LiHO_3. This composition is close to the reported composition of $La_2LiH_{0.53}O_{3.21}\square_{0.26}$, thus our solid-solution model is consistent.
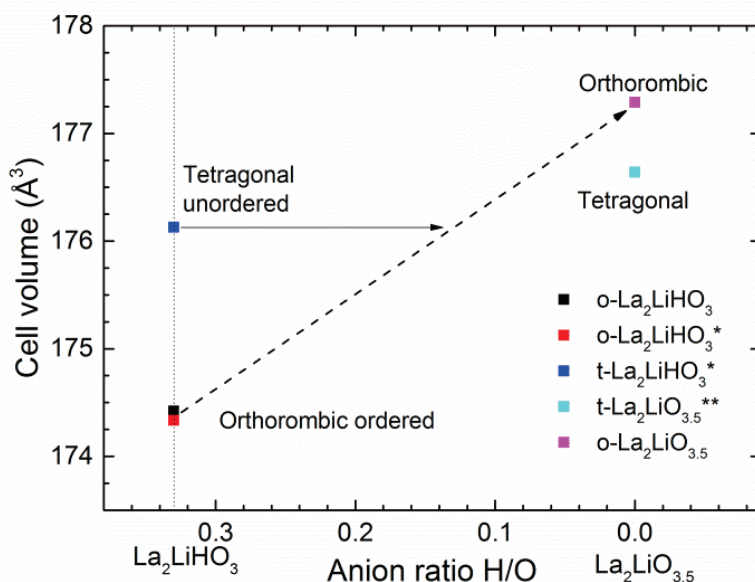

Figure 33: Illustration of Vegard's law for the solid solution $La_2LiH_{1-x}O_{3+x/2}$, with the end members La_2LiHO_3 and $La_2LiO_{3.5}$. Structural information from crystal structures marked by an asterisk is from ref [19], a double asterisk is from ref [146], and the others are from this work. "o" and "t" refer to orthorhombic and tetragonal crystal structures. Reused with premission from American Chemical Society.[141]

4.1.5 Vibrational properties and chemical bonding in La_2LiHO_3

As hydrogen has the largest incoherent scattering cross section in La_2LiHO_3, INS (section 3.2.3.2) is a well-suited method to study the vibrations and local surroundings of the hydride anions in

La_2LiHO_3. By the means of DFT we calculate the phonon dispersion and vibrational density of states, and by weighting with the neutron scattering cross sections we obtain an *in silico* INS spectrum of La_2LiHO_3, Figure 34. Based on this we identify the three high-energy vibrations to originate from the hydride anions vibrating in the *x*-, *y*- and *z*-direction in the crystal structure, Figure 34. The high energies of the vibrations imply that the hydride anions are tightly bonded, most tightly in the *x*-direction towards the lithium atoms. The good agreement between the INS spectra and the *in silico* spectrum again confirm the presence of hydride anions in the crystal structure.
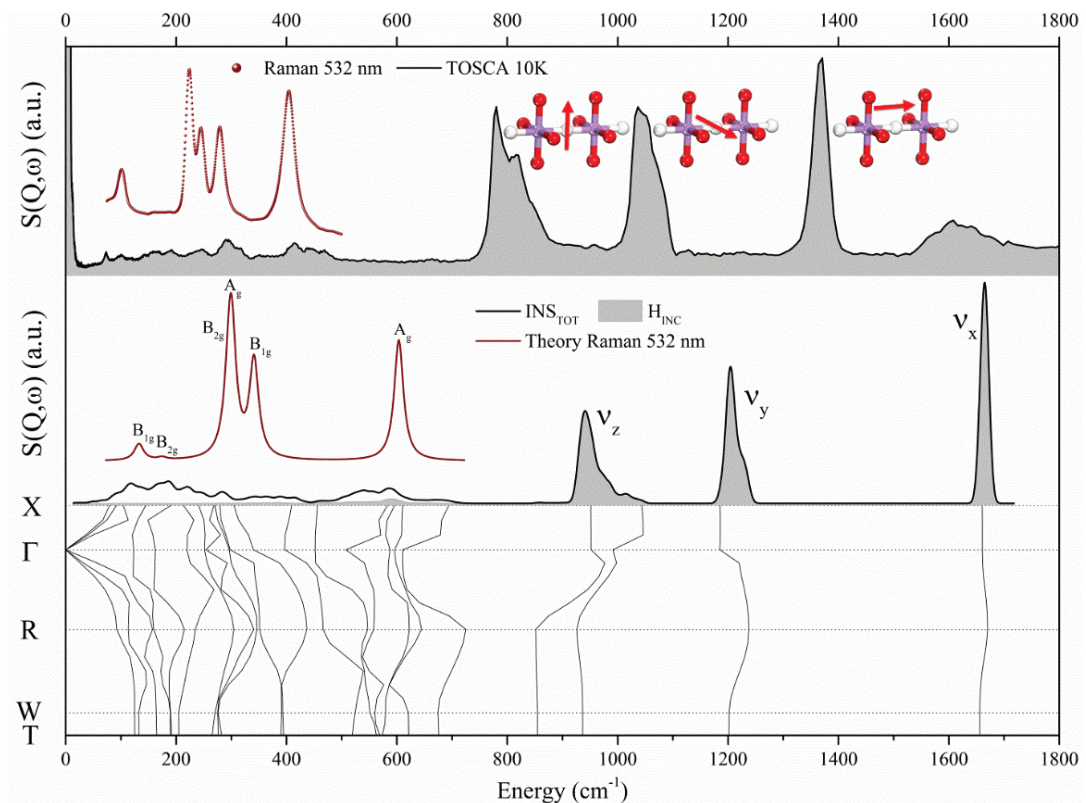

Figure 34: Top: INS spectra (black) of La_2LiHO_3 collected on TOSCA at 10 K and Raman spectra (dark red) collected with a laser wavelength of 532 nm. The atomic models [Li(O/H)$_6$, lithium (purple), oxygen (red) and hydrogen (white)] illustrate the direction of the hydride vibration. Middle: Raman spectra (dark red) calculated by DFT with the PBE functional. The peaks are assigned to the corresponding labeled modes. Total scattering contribution is calculated from DFT, weighted with the neutron cross section (black). The shaded gray region marks the incoherent scattering originating from hydrogen. Bottom: Phonon dispersion calculated by DFT. Reused with premission from American Chemical Society.[151]

The DFT model from the vibrational analysis can be further used, by the means of several methods: Born-Effective-Charge analysis, Bader analysis and Mulliken population analysis, to gain insight to the bonding in La_2LiHO_3.[152] Based on the chemical composition, we expect purely

ionic bonding as both lithium and lanthanum are ionic in nature. However, all computational methods show that we have deviations from an ionic bonding situation, Table 14. The charges are deviating from the ideal ionic charges and the charge distributions are non-spherical, thus indicating polarization of the electronic clouds and covalent bonding character.

The bond overlap population from Mulliken population analysis indicate the number of electrons transferred in a chemical bond. We note that the lanthanum-oxygen bonds show values corresponding to covalent character (values above 0.4 indicate significant covalent character). This is in contrast to our expectations, as lanthanum oxide is an ionic compound and we would expect the same bond character here. Further, Fajans' rules also suggest ionic bonding due to the large size of the lanthanum cation.[153-155] Thus the observed and expected bonding situation is not consistent. On the other hand, the bonding situation for lithium is clearly more ionic as the bonds to both the oxide and hydride anions have bond overlap population values around zero.

Table 14: Calculated Born-Effective-Charges, Bader Charges, Mulliken Population Analysis for La$_2$LiHO$_3$, and the Bond overlap population (BOP) between constituents of La$_2$LiHO$_3$. For the Born-Effective-Charges, *xx*, *yy* and *zz* correspond to charge distribution along the *x*-, *y*- and *z*-direction, respectively. Reused with premission from American Chemical Society.[151]

	Born−Effective−Charge			Bader	Mulliken population		
	xx	*yy*	*zz*	Charges (e)	Charges (e)	Bonds	BOP
La (4i)	4.18	3.56	3.70	1.92	1.2	La−O1/O2	0.9/0.52
Li (2a)	0.89	0.79	0.92	0.8	0.98	La−H	0.13
H (2b)	−0.95	−0.89	−0.53	−0.6	−0.59	Li−O1/O2	0.1/−0.25
O1(4i)	−2.89	−2.47	−2.5	−1.65	−0.86	Li−H	−0.2
O2(2d)	−2.5	−2.1	−2.81	−1.72	−0.93		

Altogether, unexpected deviations from the expected bonding situation, ionic bonding, was encountered when analyzing the bonding situation by DFT. Based on this, we conclude that the bonding in La$_2$LiHO$_3$ is anisotropic. In the rock salt layer, the lanthanum-oxygen bonding is covalent, while in the perovskite layer, the bonding, lithium-oxygen/hydrogen, is of ionic character.

4.1.6 Evaluation of diffusion paths in La$_2$LiHO$_3$ by DFT

From DFT calculations, we have described the vibrations and bonding in La$_2$LiHO$_3$ (section 4.1.5). Aspects of the migration at an atomic scale in the material can also be understood in terms of DFT calculations. The minimal energy migration pathways were calculated by the climbing nudged elastic band method (cNEB) for migration between different sites in the crystal structure; see Table 15 and Figure 35.[152] The lowest energy migration pathway for migration of hydride anions was found to be 0.68 eV for in-plane migration in the perovskite layer, between the O2 and H position (see Figure 23). Similarly, the lowest energy migration pathway for oxide

anions was found to be 1.2 eV for migration between the same positions. Therefore the best approach to promote hydride anion diffusion in La_2LiHO_3 is to introduce vacancies so the hydride anions may migrate in the perovskite layer.

Table 15: Considered migration pathways in DFT calculations. Migration distances, involved sites, and calculated migration barrier heights (in eV) for migration in the La_2LiHO_3 lattice are given. The path number corresponds to the paths illustrated in Figure 35. RS refers to the rock salt layer. Reused with premission from American Chemical Society.[151]

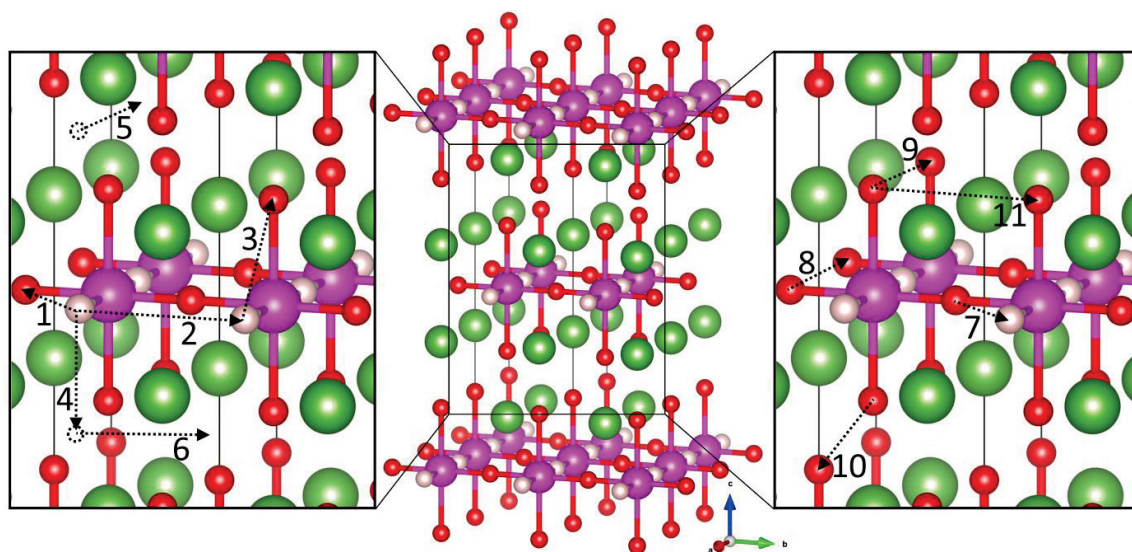| Path number	Distance (Å)	Migration ion	Transport sites	Barrier height (eV)
1	2.593	H	H−O2	0.68
2	3.764	H	H−H	8.1
3	2.927	H	H−O1	8.52
4	2.202	H	H−H_i into RS layer	2.9
5	3.575	H	H_i−H_i (along x in RS)	2.0
6	3.781	H	H_i−H_i (along y in RS)	1.93
7	2.593	O	O2−H	1.2
8	3.568	O	O2−O2	5.95
9	3.568	O	O1−O1	4.8
10	3.764	O	O1−O1	3.1
11	3.211	O	O1−O1	4.06

Figure 35: Illustration of considered migration pathways in La_2LiHO_3. The atoms correspond to lanthanum (green), lithium (purple), hydrogen (white), and oxygen (red). Calculated migration barrier height and distances are given in Table 15. Reused with premission from American Chemical Society.[151]

In the rock salt layer in the crystal structure of La_2LiHO_3, there are empty tetrahedral sites. Anion migration via these sites are reported to be favorable for the similar compounds $La_2CoO_{4+\delta}$, $La_2NiO_{4+\delta}$ and $La_4Co_3O_{10}$.[38-40] In addition, in Ba_2ScHO_3 the hydride anions migrate in the rock salt layer, giving rise to higher ionic conductivity than in $BaScHO_2$, where the hydride anions migrate in a perovskite framework (section 2.5.1).[65-66] We therefore expected migration into and within the rock salt layer to be favorable. It is striking, that migration into the rock salt layer have migration barriers of 2.9 eV, and migration within the rock salt layer have migration energies of 1.93 and 2.0 eV. These are large migration barriers and migration by these paths are not favorable. Considering our findings on the bonding situation in La_2LIHO_3 in section 4.1.5, we assign the unexpected high migration barriers to the covalent bonding in the system. The covalent bonding in the rock salt layer creates channels of electron density in the rock salt layer, hindering the hydride anions to migrate into and within the rock salt layer.

4.1.7 Momentum distribution of the hydride anions in La_2LiHO_3

QENS experiments gave no evidences of hydride anion diffusion in La_2LiHO_3 below its decomposition temperature (section 4.1.3.3), and the DFT calculations gave useful insight to the bonding and diffusion mechanisms in the system (section 4.1.5). To further investigate the abovementioned topics, we set out to perform an NCS experiment (section 3.2.3.3) at the VESUVIO spectrometer at ISIS pulsed neutron and muon source.[156-157]

The mass-resolved nature of NCS allows us to independently probe changes in the momentum distribution of hydrogen atoms as a function of temperature, with no concerns of the time-scale of dynamics in the system that may influence the momentum distribution. Considering that we concluded that the diffusion of hydride anions was outside the timescales accessible at the OSIRIS and IRIS instruments (section 4.1.3.3), a technique not limited by timescales is an advance.

In NCS, one benefits from that one can isolate the part of a spectrum and directly compare it with the kinetic energy of a particular recoiling nuclear isotope calculated based on a model predicting its partial vibrational density of states.[134, 158-161] This important distinctive feature of the NCS technique allowed us to selectively measure the hydrogen momentum distribution in La_2LiHO_3 at a series of temperatures from low temperature to 227 °C (30 K to 500 K). Each collected data set was fitted with an ideal Gaussian distribution, and the Gaussian width (σ – the standard deviation, hereinafter referred to as width) was recorded for each temperature, as shown in Figure 36.

From careful inspection of the data presented in Figure 36, it is clearly no marked change of the width (within one standard deviation error of the width) of the recoil peak corresponding to hydrogen across the investigated temperature range, stating that there is no change in the local effective potential of the hydride anion. Moreover, capitalizing on the methodology, we used a simulation of partial hydrogen-projected vibrational density of states (section 4.1.5) to calculate the width via the first moment of the distribution.[134, 158-161] The result of this calculation is reported

as thick blue line in Figure 36. It is clear that the result of the *ab initio* calculation agrees very well with the experimental values. The DFT calculation has been performed within the harmonic lattice limit. Hence, this very good agreement signifies no marked departures from harmonicity in the entire range of temperatures.

The same degree of agreement between the experiment and theory across such a large range of temperatures clearly signifies that no marked changes in the shape of the local effective potential felt by the hydride anions is observed over the entire investigated temperature range (30 to 500 K). However, this observation does not mean that the hydride anions exhibit the same magnitude of binding or strength of chemical bonding in the lattice in the whole temperature range.
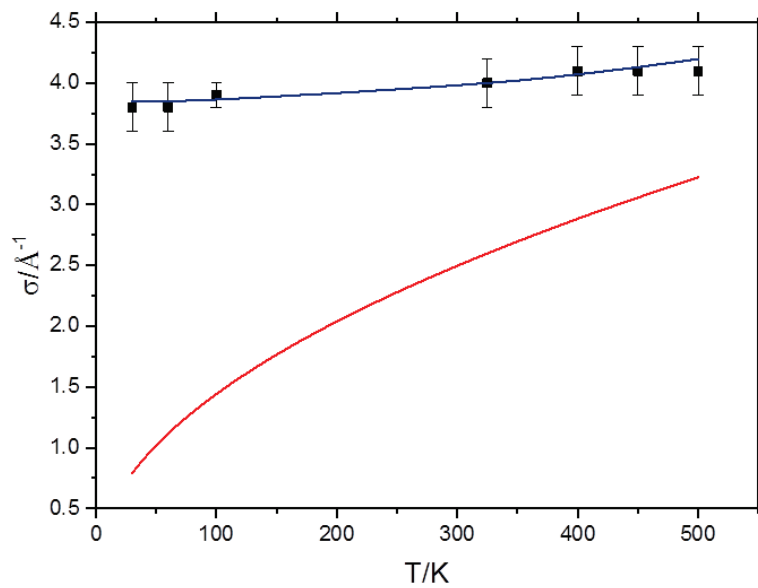

Figure 36: Gaussian width of the hydride anion momentum distribution measured by NCS in La$_2$LiHO$_3$, as a function of temperature. Black squares: experimental data; solid red line: the width of the hydride anion momentum distribution calculated from the Maxwell-Boltzmann distribution; solid blue line: the hydride anion momentum distribution calculated from the DFT calculation result for the hydride anion vibrational density of states (see text for details).

By calculating the nuclear momentum distribution from the classical Maxwell-Boltzmann approximation of free, not interacting particles (shown as red solid line in Figure 36), we derive the expected kinetic energy of the nucleus. We can compare the measured nuclear momentum distribution widths in a NCS experiment with the calculated values from the classical Maxwell-Boltzmann approximation. The measured excess nuclear momentum distribution widths correspond to the local effective binding potential felt by the nucleus in the lattice, *i.e.* we obtain the binding energy of the hydride anions in the lattice.

In the case of La_2LiHO_3, the constancy of the values of the hydride anion momentum distribution widths across the whole temperature range compared to the increasing momentum distribution calculated form the classical Maxwell-Boltzmann distribution means that: (1) there is no change in the curvature of the local binding potential felt by the hydride anions upon heating, but (2) a significant weakening of the effective binding energy of the hydride anions in the lattice of La_2LiHO_3 occurs with increasing temperature.

The NCS result described here has important ramification for the question of the hydride anion diffusion in La_2LiHO_3. Namely, in the event that hydride anions began diffusing with increased temperature, the curvature of the local potential felt by the hydride anions should substantially change owing to the change in their local environment. This in turn would have changed the values of the hydride anion momentum distribution widths, which is not observed. On the whole, this NCS experiment therefore does not support the hypothesis that hydride anions exhibit diffusive motion within the measured temperature range, as we can explain the momentum distribution widths by phonon calculation. This conclusion is also in compliance with QENS, where we similarly observe absence of diffusion at similar conditions, and the AIMD calculations of Bai *et al*. which indicate no diffusion in La_2LiHO_3 in the absence of vacancies (section 2.5.1.1).[93]

What is observed, however, is the tendency of the hydride anions in La_2LiHO_3 to be weaker bonded with increasing temperature. If we extrapolate to higher temperatures, we find that the kinetic energy of the hydride anions should at some temperature be similar to the effective binding energy, and then the hydride anions should be free to migrate. In this scenario we will expect increased hydride diffusion at the temperature where the hydride anions become free to migrate. Further, we can speculate whether the increased hydride anion diffusion in this scenario is the origin of the decomposition, which we then correctly assigned the incensement of the QENS signal to.

4.1.8 Predicting oxyhydrides – Manipulating bonding and diffusion

Hydride anion diffusion in La_2LiHO_3 synthesized by the halide salt flux method is thoroughly studied in this thesis and is determined to be absent in the samples prepared in this work. To prepare oxyhydrides with enhanced hydride anion conductivity or other attractive properties, we need a basis to build on in the search for new oxyhydrides. In that respect, we have suggested a list of possible new oxyhydrides we consider possible to synthesize by the halide salt flux method in Appendix A based on general considerations of which cations could occupy the A- and B-sites in perovskite and perovskite-related oxyhydrides. The A- and B-site cations are evaluated following the basic principles; (1) which site do we expect the cation to take, (2) will the cations be stable in the flux, and (3) can the cations be accommodated in a compound which contains hydride anions without being reduced. Currently, a conservative selection of cations is included in Appendix A, thus it is possible to expand on the current suggestions. In addition, the melting

temperatures for relevant halide salts and decomposition temperatures for metal hydrides are included.

The general idea behind Appendix A is to lay a foundation for exploring synthesis of oxyhydrides by the halide salt flux method. A huge parameter-space for exploration is available and here we systematize our options. In Appendix A, only suggestions for the perovskite and RP1-type crystal structures are given, but the principle can be expanded to RP2, RP3, Aurivillius phases, spinel, garnet, *etc*. Average half-integer valence on a site could also be incorporated to the appendix to access *e.g.* oxyhydrides with two A-site cations with different valence as $LaSrLiH_2O_2$.

Now that we have an overview of possible new oxyhydrides, we should consider which of these oxyhydrides could potentially show enhanced hydride anion conductivity compared with La_2LiHO_3. From literature we know that the RP1 Ba_2ScHO_3 show superior hydride anion conductivity to the perovskite $BaScHO_2$ as the hydride anions move in the rock salt layers and not in the perovskite layer (section 2.5.1), and therefore understand that manipulating the hydride anions to move in the rock salt layer can be favorable.[65-66] We therefore attempt to transfer this concepts to La_2LiHO_3.

The factor we believe to be the origin of no or little hydride anion diffusion in La_2LiHO_3 is the covalent bonding between lanthanum and oxygen in the rock salt layer. Based on this finding, we may ask what aspects promote this covalent character. Two key factors come to mind. First, lithium has low electronegativity and charge to be a B-cation. This implies that lithium attracts the electron clouds of the anions weakly, allowing lanthanum to act as a polarizing cation although it usually does not. Second, lanthanum is bonded to both oxide and hydride anions. The ionic character of the lanthanum-hydride bond may strengthen the covalent character of the lanthanum-oxygen bond further.

By using these concepts, we see that by choosing appropriate A- and B-cations, we may reduce the covalent character of the bonding in the rock salt layer. Based on this, we suggest the compounds $Sr_2MgH_2O_2$ and $Ba_2MgH_2O_2$ in Appendix A. The higher charge of magnesium as B-cation will attract the electron clouds of the anions more strongly than lithium does, therefore suppress the polarization of the bonds between the A-cation and the anions. Further, the lower charge of strontium or barium as A-cation will create more ionic bonds. Thus, in these compounds we expect reduced covalent bonding in the rock salt layer and therefore hydride migration into and within the rock salt layer may be feasible. As discussed in section 2.3, the oxide anion conducting RP1 $La_2NiO_{4+\delta}$ and $La_2CuO_{4+\delta}$ have interstitial oxide anions in the rock salt layer promoting oxide conductivity by empty tetrahedral sites.[38-39] Similarly, we can propose $Ba_2Mg_{1-x}Sc_xH_{2+x}O_2$ and $Sr_2Mg_{1-x}Sc_xH_{2+x}O_2$ as oxyhydrides with interstitial hydride anions in the rock salt layer. This may increase the hydride conductivity of the suggested oxyhydrides further.

4.2   The LaSr$_3$Fe$_3$H$_y$O$_{10-x}$-system

LaSr$_3$Fe$_3$O$_{10-x}$ ($0 \leq x \leq 1.21$) creates the basis for this section. The possibility of incorporating hydride anions into this compound is considered promising, thus we refer to it as the LaSr$_3$Fe$_3$H$_y$O$_{10-x}$-system. The compound takes a RP-type crystal structure like many oxyhydrides and it can easily form vacancies which hydride anions can potentially fill. We therefore consider topotactic anion-exchange as an approach suitable to incorporate hydride anion into LaSr$_3$Fe$_3$O$_{10-x}$. A potential challenge is that iron is known to not form metal hydrides. However, this is not necessarily of major impact as cobalt and manganese form oxyhydrides, but are known to not form metal hydrides.[50, 64]

In section 2.5.2 the importance of vacancies in the precursor material is emphasized. Thus, before attempts to prepare oxyhydrides, insight to the defect situation in the precursor compound would be a valuable asset. The RP3 member LaSr$_3$Fe$_3$O$_{10}$ is the parent compound for several reduced and hydrate derivatives.[44-45] As discussed in section 2.3, the crystal structure of LaSr$_3$Fe$_3$O$_9$ is not reported in detail.[45] Further, there are no reports on the intermediate compositional range between LaSr$_3$Fe$_3$O$_{10}$ and LaSr$_3$Fe$_3$O$_9$. These topics also justify investigations.

4.2.1   Structural and magnetic aspects of LaSr$_3$Fe$_3$O$_9$

Although Øygarden et al. indexed LaSr$_3$Fe$_3$O$_9$ with an orthorhombic unit cell, the crystal structure is not accurately described.[45] The crystal structure of the related compound NdSr$_3$Fe$_3$O$_9$ is reported in its paramagnetic state.[162-163] By combined Rietveld refinements of synchrotron X-ray and neutron diffraction, we used the information at hand to accurately describe the crystal structure of LaSr$_3$Fe$_3$O$_9$. However, the neutron diffraction showed extra peaks at 8 and 298 K that could not be described by the crystallographic unit cell. Therefore, we attributed these peaks to magnetic ordering. Magnetic ordering was confirmed by magnetic susceptibility measurements, and antiferromagnetic ordering to temperatures above 350 K is suggested. To find the correct magnetic space group the crystal structure was transferred to standard settings to ease this process. The magnetic space group was determined by ISODISTORT to be $P_C bcm$ (BNS: 57.391), with a cell shifted (¼, ¼, ¼) with respect to the crystallographic unit cell. The crystal and magnetic structure of LaSr$_3$Fe$_3$O$_9$ is illustrated in Figure 37, and crystallographic and magnetic information is given Table 16 and Table 17.

Our findings confirm LaSr$_3$Fe$_3$O$_9$ to be isostructural with NdSr$_3$Fe$_3$O$_9$, and it takes a RP3-related crystal structure. In LaSr$_3$Fe$_3$O$_9$, the octahedral in middle layer in the perovskite slab is exchanged by tetrahedrons, similar to a brownmillerite. Thus, the crystal structure of LaSr$_3$Fe$_3$O$_9$ can be described as built up of brownmillerite slabs separated by one half rock salt layer. The magnetic structure is antiferromagnetic with G-type ordering of the magnetic moments. The octahedral site (Fe1) shows slightly higher magnetic moment than the tetrahedral site (Fe2), Table 17.

Table 16: Crystal structure data for LaSr$_3$Fe$_3$O$_9$ as obtained from combined Rietveld refinement of SR-XRD and PND in space group *Cmcm* at 8 K giving unit cell parameters of a = 28.7562(13), b = 5.5280(2), c = 5.4583(2). U_{iso} is the thermal displacement parameter. Reused with premission from Elsevier.[164]

Atom	Wyckoff	x	y	z	Occupancy	U_{iso} (Å^2)
La1	8g	0.20182(6)	0.2520(4)	0.25	0.2157(10)	0.0058(6)
Sr1	8g	0.20182(6)	0.2520(4)	0.25	0.7843(10)	0.0058(6)
La2	8g	0.07849(7)	0.2400(4)	0.25	0.2843(10)	0.0058(6)
Sr2	8g	0.07849(7)	0.2400(4)	0.25	0.7157(10)	0.0058(6)
Fe1	8g	0.64350(10)	0.2482(7)	0.25	1	0.0096(4)
Fe2	4c	0	0.6890(7)	0.25	1	0.0096(4)
O1	8e	0.8586(3)	0	0	1	0.0077(8)
O2	8e	0.6360(2)	0	0	1	0.0077(8)
O3	8g	0.71286(17)	0.2249(12)	0.25	1	0.0077(8)
O4	8g	0.55869(18)	0.2939(12)	0.25	1	0.0077(8)
O5	8f	0	0.358(2)	0.359(2)	0.5	0.0077(8)
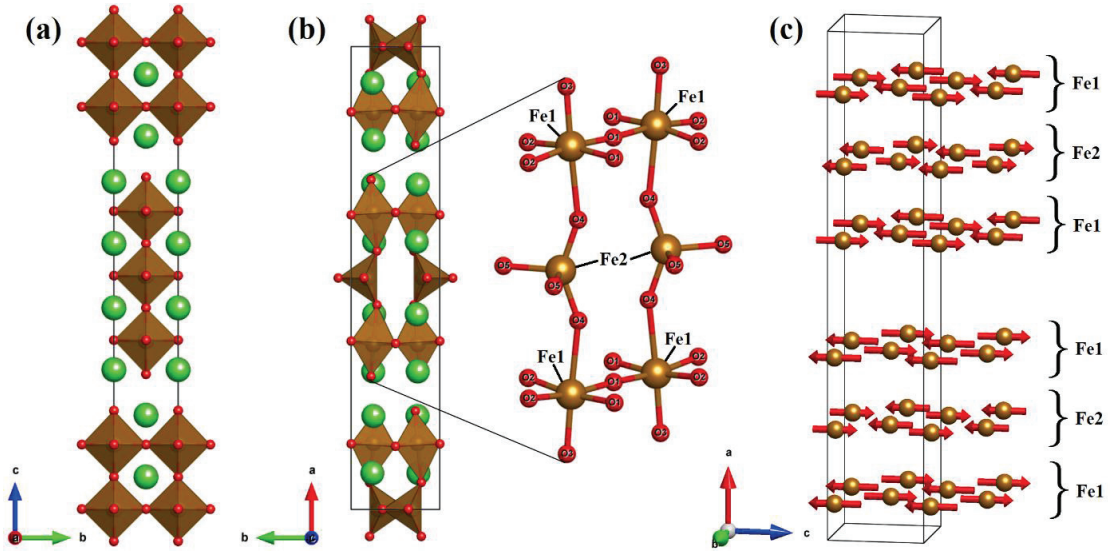
Figure 37: Crystal structure of LaSr$_3$Fe$_3$O$_{10}$ (*I4/mmm*) viewed along the *a*-axis. (b) Crystal structure of LaSr$_3$Fe$_3$O$_9$ (*Cmcm*) viewed along the *c*-axis. The crystal structure is built up of slabs of two perovskite layers with an additional layer of chains of vertex-sharing FeO4 tetrahedron in the center position, the slabs again being separated by one half layer of rock salt as common in RP3-type compounds. Light green, dark green, orange and red atoms correspond to strontium, lanthanum, iron and oxygen respectively. (c): Visualization of the G-type magnetic structure of LaSr$_3$Fe$_3$O$_9$ at 8 K. Only the iron atoms are displayed. The magnetic moments of the tetrahedral iron atoms (Fe2) are slightly lower than the octahedral iron atoms (Fe1). Reused with premission from Elsevier.[164]

Table 17: Magnetic moments of the iron atoms extracted from Rietveld refinements of the magnetic structure on powder neutron diffraction patterns. The symmetry of the magnetic space group only allows refinement of M_z, thus M_x and M_y is zero. Reused with premission from Elsevier.[164]

	M_z Fe1 (μ_B)	M_z Fe2 (μ_B)
8K	3.99(5)	3.58(8)
298K	3.24(8)	2.7(1)

4.2.2 Phase correlations between $LaSr_3Fe_3O_{10-\delta}$ and $LaSr_3Fe_3O_{9\pm\epsilon}$

$LaSr_3Fe_3O_{10-\delta}$ and $LaSr_3Fe_3O_{9\pm\epsilon}$ are two distinct phases with different crystal structures and oxygen ordering. Therefore we expect a two-phase region for intermediate oxygen compositions, and some degree of oxygen-non-stoichiometry in the two compounds.[44, 165] Based on this we prepared $LaSr_3Fe_3O_{10-x}$ ($0 \leq x \leq 1$) samples with various oxygen content by NbO reduction to study the phase situation in the intermediate range between $LaSr_3Fe_3O_{10-\delta}$ and $LaSr_3Fe_3O_{9\pm\epsilon}$. The overall oxygen content was determined by cerimetric titration and the molar fractions by Rietveld refinements. Based on the analysis we observe a two-phase region for $0.51 < x < 0.85$, Figure 38 a, and the transition between $LaSr_3Fe_3O_{10-\delta}$ and $LaSr_3Fe_3O_{9\pm\epsilon}$ is non-continuous. It is clear that $LaSr_3Fe_3O_{10-\delta}$ shows a large ability to lose oxygen while retaining the crystal structure. $LaSr_3Fe_3O_{9\pm\epsilon}$ on the other hand shows less ability to incorporate oxygen while retaining the crystal structure. Additionally, TGA (not included) show that removal and insertion of oxygen can be done reversible in both phases and that $LaSr_3Fe_3O_{9\pm\epsilon}$ can release oxygen, *i.e.* $\epsilon < 0$.

For further investigations of the two-phase region and the phase relation between $LaSr_3Fe_3O_{10-\delta}$ and $LaSr_3Fe_3O_{9\pm\epsilon}$, we performed an *in situ* oxidation experiment at 390 °C of a sample with nominal composition $LaSr_3Fe_3O_{9.22}$. The sample is in the two-phase region, mainly composed of $LaSr_3Fe_3O_{9\pm\epsilon}$. By inspections of the diffraction patterns (Figure 38 b), some aspects are clear. First, we see that the sample is still after heating to 390 °C in the two-phase region, thus no phase-transition to a high temperature crystal structure occurs. We see that the (117)-reflection of $LaSr_3Fe_3O_{10-\delta}$ moves to higher Q, indicating that the unit cell contracts, consistent with an oxidation of the compound. From surface Rietveld refinement we extract information of the evolution of the unit cell, Figure 39. Here, we also observe a contraction of the cell throughout the oxidation. In the beginning, the contraction is rapid, and then the contraction continues more steadily. The rapid contraction in the beginning of the experiment is attributed to the change in partial pressure of O_2 when the capillary was cut open.
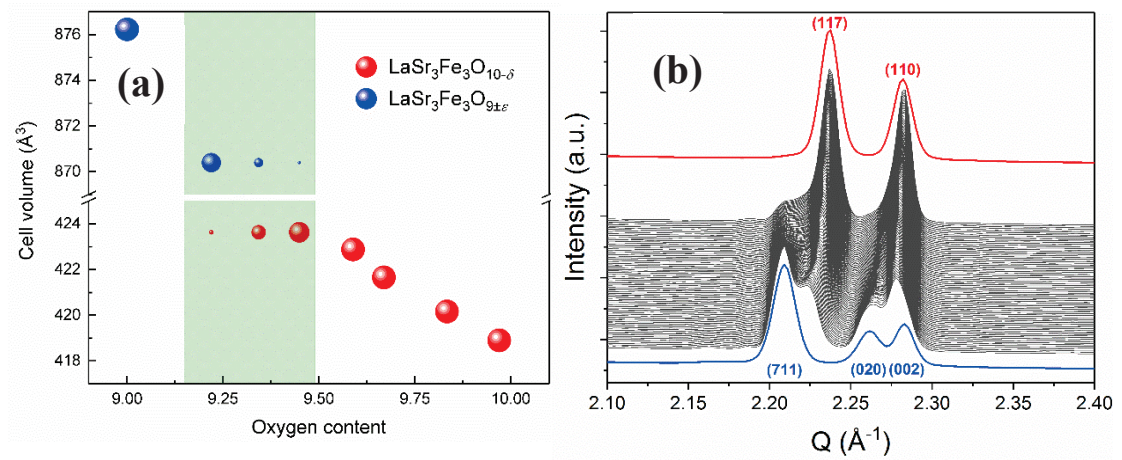
Figure 38: (a) Phase correlations and cell volumes of LaSr$_3$Fe$_3$O$_{10-\delta}$ (red spheres) and LaSr$_3$Fe$_3$O$_{9\pm\epsilon}$ (blue spheres) for LaSr$_3$Fe$_3$O$_{10-x}$ samples. The shaded area illustrates the two-phase region and the sizes of symbols illustrate the mole fraction of the individual phases in the two-phase region. (b) Stacked i*n situ* SR-XRD patterns of the oxidation of LaSr$_3$Fe$_3$O$_{9.22}$ at 390 °C in an open capillary. The blue and red are the calculated contribution from Rietveld refinements of orthorhombic LaSr$_3$Fe$_3$O$_{9\pm\epsilon}$ and of tetragonal LaSr$_3$Fe$_3$O$_{10-\delta}$ of the first and last diffraction pattern respectively. The Miller indices are given under the respective reflections. Note that the sample is in the two-phase region though the entire experiment. Mass fractions from Rietveld refinements are shown in Figure 39. Reused with premission from Elsevier.[164]
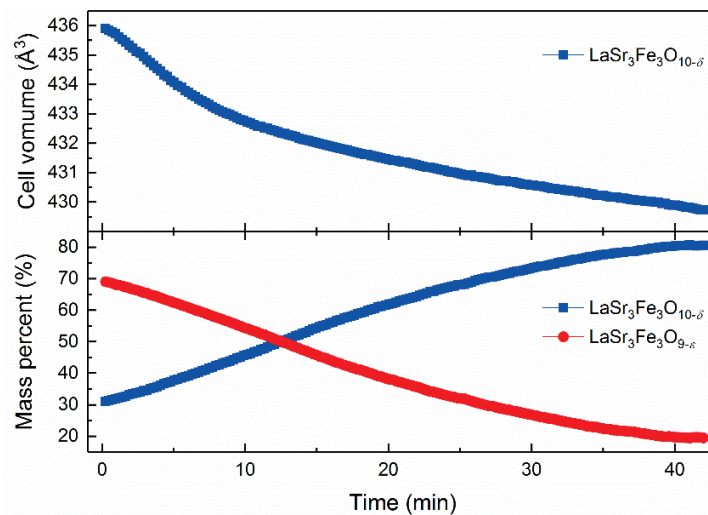

Figure 39: Evolution of cell volume of LaSr$_3$Fe$_3$O$_{10-\delta}$ (top) and evolution of mass fractions for LaSr$_3$Fe$_3$O$_{10-\delta}$ (red) and LaSr$_3$Fe$_3$O$_{9\pm\epsilon}$ (blue) during isothermal oxidation at 390 °C from surface Rietveld refinements. Reused with premission from Elsevier.[164]

4.2.3 Oxyhydride formation in the LaSr$_3$Fe$_3$H$_y$O$_{10-x}$-system

After studying the LaSr$_3$Fe$_3$O$_{10-x}$-system in detail with respect to crystal structure and vacancy formation, we decided to investigate the system further to see if we could incorporate hydride anions into the compounds by topotactic anion-exchange. The synthesis strategy was adapted from well-studied system as LaSrCoH$_{0.7}$O$_3$ and BaTiH$_x$O$_{3-x}$.[50, 56] Thus, LaSr$_3$Fe$_3$O$_{10}$ and LaSr$_3$Fe$_3$O$_{9.22}$ was carefully mixed and grinded with a 1:4 molar ratio CaH$_2$, and pressed into a pellet. Then the pellets were heated at temperatures between 400 and 450 °C for 7 days in evacuated quartz ampoules. The ampoules were opened inside an argon filled glovebox and the samples were further analyzed. Note that the excess CaH$_2$ and potential CaO was not removed from the samples and therefore TGA experiments have not been carried out. Capillaries were packed and sealed inside the glove box before XRD measurements.

Careful inspection of XRD of the obtained products show that the diffraction patterns, obtained from both LaSr$_3$Fe$_3$O$_{9.22}$ and LaSr$_3$Fe$_3$O$_{10}$ reacted with CaH$_2$ (400−450 °C), are very similar to that of unreacted LaSr$_3$Fe$_3$O$_{10}$ (Figure 40). Thus, the atomic arrangement in the CaH$_2$-reacted samples are assumed to be similar to a RP3-type crystal structure. Note that the LaSr$_3$Fe$_3$O$_{9.22}$-samples have LaSr$_3$Fe$_3$O$_{9\pm\epsilon}$ as the primary phase before the reduction step, thus this framework must be converted into a RP3-framework by the reaction with CaH$_2$.
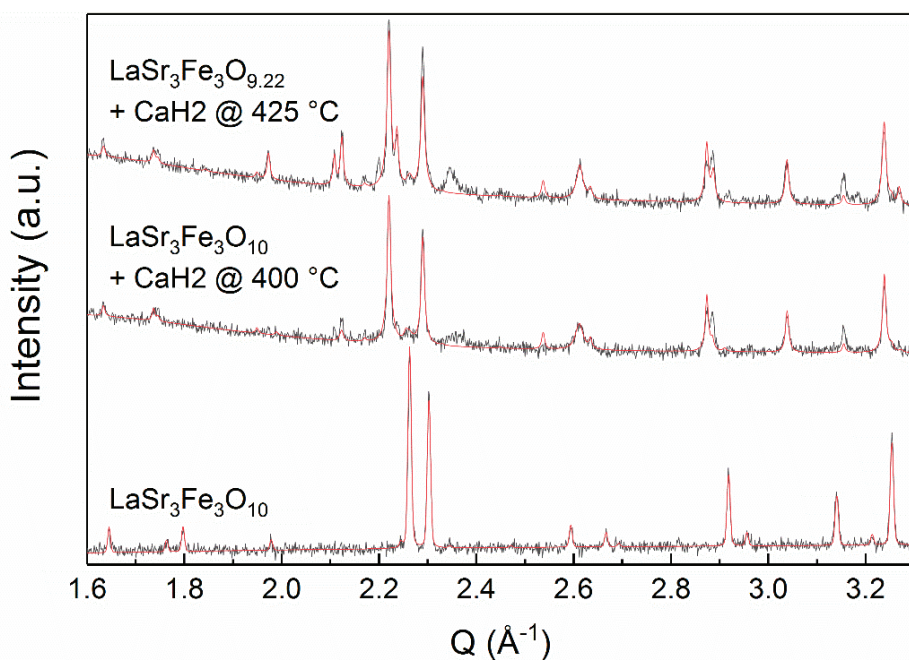

Figure 40: XRD patterns of LaSr$_3$Fe$_3$O$_{10}$, and LaSr$_3$Fe$_3$O$_{10}$ and LaSr$_3$Fe$_3$O$_{9.22}$ reacted with CaH$_2$ at 400 and 425 °C respectively. The two strongest reflections from LaSr$_3$Fe$_3$O$_{10}$ are clearly moved to lower *Q*, indicating that the cell have expanded. The additional reflections in the CaH$_2$-reacted samples are from CaH$_2$ (*Pnma*) and CaO (*Fm-3m*).

To extract further information, Rietveld refinements based on a $LaSr_3Fe_3O_{10}$-model were carried out. All the CaH_2-reacted samples show distinct and similar deviations in the unit cell parameters relative to $LaSr_3Fe_3O_{10}$; the unit cell parameters are expanded with about 0.9 Å along the c-direction compared to $LaSr_3Fe_3O_{10}$, Table 18.

Table 18: Unit cell parameters of $LaSr_3Fe_3O_{10}$ and the reduced samples. The last column shows the deviation of the c-axis of the samples compared with $LaSr_3Fe_3O_{10}$.

Sample	Temperature	a (Å)	c (Å)	Deviation (Å)
$LaSr_3Fe_3O_{10}$	Reference	3.86677(12)	28.0448(12)	-
$LaSr_3Fe_3O_{10}$	400 °C	3.87964(18)	28.9415(18)	0.8967(22)
$LaSr_3Fe_3O_{10}$	425 °C	3.8800(4)	28.954(4)	0.909(4)
$LaSr_3Fe_3O_{9.22}$	425 °C	3.88089(16)	28.9486(16)	0.9038(2)
$LaSr_3Fe_3O_{10}$	450 °C	3.88(2)	28.9(2)	0.9(2)
$LaSr_3Fe_3O_{9.22}$	450 °C	3.8805(4)	28.959(4)	0.914(4)

As the framework of the CaH_2-reacted samples is assumed to be similar to that of the RP3, the first hypothesis to consider is that the samples are reduced to $LaSr_3Fe_3O_8$, similar to $La_4Ni_3O_8$ with square-planar coordination of iron as in $SrFeO_2$ (section 2.2 and 2.3).[31, 41, 43] However, the reduction of $La_4Ni_3O_{10}$ to $La_4Ni_3O_8$, is associated with a contraction along the c-axis since nickel is going from octahedral to square-planar coordination. In the case of the CaH_2-reacted samples, we observe an elongation. Thus, we must exclude the formation of $LaSr_3Fe_3O_8$ with square-planar iron coordination.

To clarify the situation, neutron diffraction was carried out. Neutron diffraction supplies excellent contrast between hydrogen and oxygen (section 3.2.1) and could therefore clarify whether hydride anions are incorporated into the crystal structure. As the sample quantities were limited, all the CaH_2-reacted $LaSr_3Fe_3O_{10}$ and $LaSr_3Fe_3O_{9.22}$ samples were mixed, and measured at the PUS instrument at Institute for Energy Technology.[140]

An initial refinement based on the crystal structure of $LaSr_3Fe_3O_{10}$ gave a reasonable fit. To test if hydride anions might be present, all atomic positions and oxygen occupancies were refined with the thermal displacement parameter restricted to be equal for atoms for the same type. We found that the equatorial oxygen (O4) in the middle perovskite layer (Figure 37 a) converged to zero, with R_{wp} reduced from 5.50 % to 5.21 %. This structural model gives a composition of $LaSr_3Fe_3O_{8.1}$, with 2-coordinated iron, Table 19 and Figure 41 a. The reasonable oxidation state of 2.12 is obtained from bond-valance-sum calculations (R_0 = 1.759, B = 0.37).[166] However, 2-coordinated iron is considered highly unlikely due to the low coordination number. This model is therefore rejected.

Table 19: Refined structural parameters for LaSr$_3$Fe$_3$O$_{8.1}$ from neutron diffraction data, in space group *I4/mmm* and with unit cell parameters a = 3.8813(4) Å, b = 3.8813(4) Å and c = 28.928(4) Å. R_{wp} of the refinement was 5.21 % and R_{exp} 0.295 %. U_{iso} corresponds to the thermal displacement parameter.

Atom	Wyckoff	x	y	z	Occupancy	U_{iso} (Å^2)
La1	4e	0	0	0.5766(6)	0.25	0.29(18)
Sr1	4e	0	0	0.5766(6)	0.75	0.29(18)
La2	4e	0	0	0.7000(6)	0.25	0.29(18)
Sr2	4e	0	0	0.7000(6)	0.75	0.29(18)
Fe1	2a	0	0	0	1	1.6(2)
Fe2	4e	0	0	0.1420(7)	1	1.6(2)
O1	8g	0	0.5	0.1415(8)	1	1.45(19)
O2	4e	0	0	0.0607(9)	1	1.45(19)
O3	4e	0	0	0.2082(8)	1	1.45(19)
O4	4c	0	0.5	0	0.06(5)	1.45(19)
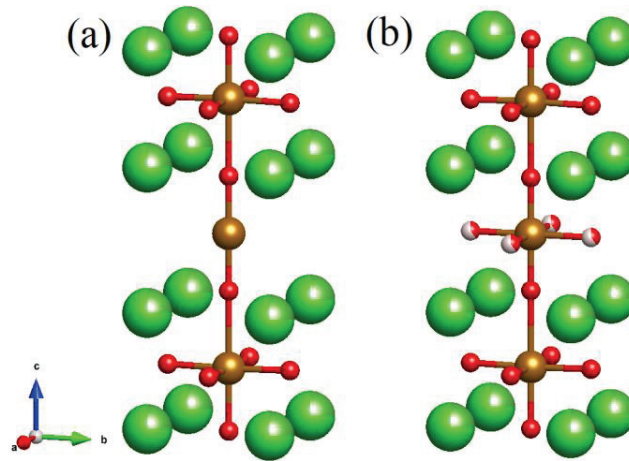
Figure 41: Structural models of one perovskite slab in (a) LaSr$_3$Fe$_3$O$_8$ and (b) LaSr$_3$Fe$_3$H$_{1.1}$O$_{8.9}$ from Rietveld refinements of neutron diffraction data from the PUS instrument at Institute for Energy Technology.[140] In (a) the O4 (see Table 19) is removed as the occupancy is close to zero.

Based on this, we introduced hydrogen to the structural model on the equatorial oxygen position (O4) in the middle octahedra layer, with the total occupancy of oxygen and hydrogen on the O4 site restricted to one. The oxygen:hydrogen ratio on the site converged to about 40:60, with a R_{wp} value of 5.21 %. The R_{wp} of this model is thus similar to the model with only oxygen vacancies. The crystal structure forms the refinements is visualized in Figure 41 b and structural details in Table 20. This structural model corresponding to the composition LaSr$_3$Fe$_3$H$_{1.1}$O$_{8.9}$, and the refinement of the neutron diffraction data is given in Figure 42. Refinements without restricting the occupancy gave comparable composition and R_{wp}.

Table 20: Refined structural parameters for LaSr₃Fe₃H₁.₁O₈.₉ from neutron diffraction data, in space group *I4/mmm* and with unit cell parameters *a* = 3.8813(4), Å, *b* = 3.8813(4) Å and *c* = 28.928(4) Å. *R_wp* of the refinement was 5.21 % and *R_exp* 0.295 %. *U_iso* corresponds to the thermal displacement parameter.

Atom	Wyckoff	x	y	z	Occupancy	U_{iso} (Å²)
La1	4e	0	0	0.5766(6)	0.25	0.31(18)
Sr1	4e	0	0	0.5766(6)	0.75	0.31(18)
La2	4e	0	0	0.6999(6)	0.25	0.31(18)
Sr2	4e	0	0	0.6999(6)	0.75	0.31(18)
Fe1	2a	0	0	0	1	1.5(2)
Fe2	4e	0	0	0.1420(7)	1	1.5(2)
O1	8g	0	0.5	0.1415(8)	1	1.46(19)
O2	4e	0	0	0.0608(9)	1	1.46(19)
O3	4e	0	0	0.2081(8)	1	1.46(19)
O4	4c	0	0.5	0	0.43(3)	1.46(19)
H4	4c	0	0.5	0	0.57(3)	1.46(19)
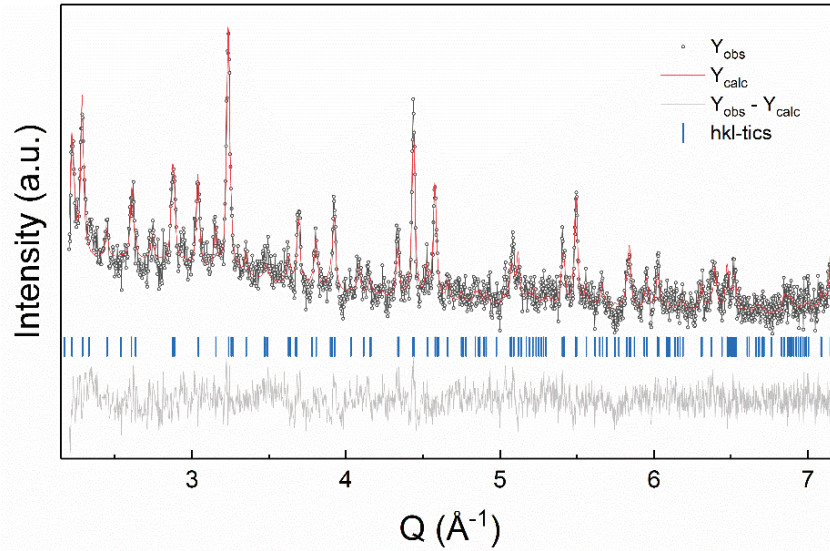
Figure 42: Neutron diffraction of CaH₂ reacted LaSr₃Fe₃O₁₀ + LaSr₃Fe₃O₉.₂₂. The structural model gives a composition of LaSr₃Fe₃H₁.₁O₈.₉ in space group *I4/mmm*. The hkl-tics indicate the position of reflections from LaSr₃Fe₃H₁.₁O₈.₉. Note that CaH₂ and CaO is also present in the sample.

Considering the bond-valence-sum in the case of $LaSr_3Fe_3H_{1.1}O_{8.2}$ is more complicated as R_0 is not given for iron-hydride bonds, however, we used the R_0 of the fluorine anion as it is the anion most similar to the hydride anion ($R_0 = 1.65$, B = 0.37). This yields an oxidation state of 3.10 for iron, which is also very reasonable. However, this model yields iron a coordination number of six, which is common for iron, and is therefore considered as unlikely. Thus, our preliminary conclusion is that the neutron diffraction indicates that we obtained an oxyhydride with composition $LaSr_3Fe_3H_{1.1}O_{8.9}$ by reacting $LaSr_3Fe_3O_{10}$ and $LaSr_3Fe_3O_{9.22}$ with CaH_2.

4. Results and discussion

At this stage we have a structural model consistent with neutron diffraction data which yields an oxyhydride, and it is the first iron containing oxyhydride. However, it must be noted that the quality of the neutron diffraction data is poor and therefore no final conclusions regarding the composition should be drawn. To conclude, additional experiments need to be carried out to verify our preliminary conclusion. We suggest TGA-DSC-MS of samples where CaH_2 and CaO is removed, as this could verify release of hydrogen from the sample upon heating and thus that hydride anions are present in the sample. Additionally, cerimetric titration, high quality neutron diffraction, NMR and possibly PEDT, may conclude on the presence of hydride anions in $LaSr_3Fe_3H_{1.1}O_{8.9}$.

5. Summary and outlook

A main goal for this work was to investigate the synthesis of oxyhydrides and anchor this material class as a new family of compounds within the NAFUMA research group. We have tackled this by applying both the halide salt flux method and topotactic anion-exchange of a possible oxyhydride precursor. With respect to the halide salt flux method, this work has yielded significant insight to aspects of this method for preparation of oxyhydrides, and the implications of this will be discussed in this section.

First, we have re-established the halide salt flux method as an aid for oxyhydride synthesis and our investigations on the preparation of the $La_{2-x}NdLiHO_3$-system yielded valuable new insight. Our investigations lead us to the conclusion that the optimal conditions for synthesis of oxyhydrides is a compromise between the thermal stability and the ionic conductivity of the oxyhydride in the synthesis medium. The halide salt flux significantly stabilizes the oxyhydrides compared to an oxidizing atmosphere, and we state that synthesis should be carried out as close to the decomposition temperature of the oxyhydride in the halide salt flux as possible to facilitate ionic mobility. For the $La_{2-x}NdLiHO_3$-system we observe the thermal stability of the oxyhydrides to decrease with increasing neodymium content, both in halide salt flux and in oxidizing atmosphere. This trend suggests lower thermal stability for oxyhydrides of heavier lanthanides which adopts the Ln_2LiHO_3 crystal structure and consequently lower synthesis temperatures are needed. DFT calculations suggest that Sm_2LiHO_3 are unstable and we therefore state that the heaviest lanthanide to form Ln_2LiHO_3 oxyhydrides are neodymium.

In the lower temperature range, we find the synthesis of the oxyhydrides to be limited by ionic conductivity. By QENS we document that the ionic conductivity shows an onset in the proximity of the decomposition temperature in oxidizing atmosphere. This temperature then yields the lower temperature limit for synthesis, as at lower temperatures the ionic conductivity in the oxyhydride is too low. Further, we surprisingly find that the lithium chloride flux yields sufficiently high mobility even in the solid state, and we prepare Nd_2LiHO_3 for the first time without impurities by the halide salt flux method. This valuable finding opens for synthesis of oxyhydrides at temperatures as low and possibly lower than used for topotactic anion-exchange (400 – 600 °C), and lower than used by the high-pressure method (650 – 1000 °C), see section 2.5.2. Additionally, it should be highlighted that this approach also offers large sample batches (gram scale), which is valuable for certain probes as neutrons as well as a necessity for applied purposes. We further foresee that it can be possible to synthesize transition metal containing oxyhydrides by the halide salt method, due to the increased temperature window accessible, as documented in this work. Finally, attempts to prepare an oxyhydride in the $LaSr_3Fe_3O_{10-x}$-system would also be very interesting. Unfortunately, this was not possible within the time-frame of this project.

In this thesis the $LaSr_3Fe_3H_{1.1}O_{8.9}$ oxyhydride is possibly prepared by topotactic anion-exchange by reacting $LaSr_3Fe_3O_{10-x}$ with CaH_2. Further experiments are needed to conclude with certainty.

5. Summary and outlook

Iron is known as a non-hydride forming metal, and it is therefore remarkable if this oxyhydride was formed as it would be the first reported iron-based oxyhydride. However, it has been shown that other non-hydride forming metals form oxyhydrides, as cobalt and nickel.[50, 67] The demonstration of an iron oxyhydride opens for investigation of oxyhydride formation in other iron systems which display oxygen non-stoichiometry. Opening this new branch of iron containing oxyhydrides could potentially lead to the discovery of new functional materials with compelling properties.

As briefly indicated above, another important aspect of the halide salt flux method is that it is possible to prepare large quantities of oxyhydride within one synthesis batch, and at most a sample of 25 grams was prepared in this work. This led the project in to neutron scattering experiments. INS, QENS and NCS experiments were carried out at ISIS pulsed neutron and muon source, and combined with computational efforts, we investigated hydride anion diffusion and chemical bonding. After the report by Kobayashi et al. on hydride anion conductivity in La_2LiHO_3 in 2016, we acted quickly. As we could prepare large sample quantities, we carried out QENS experiments to directly observe hydride anion diffusion and quantify it. However, when a QENS signal was observed, it was at higher temperatures than the reported diffusion and in proximity of the decomposition temperature in oxidizing atmosphere. Thus, we concluded that this was a dynamic associated with the decomposition of the oxyhydride.

In NCS we individually study the momentum distribution of the constituent atoms in La_2LiHO_3, and we see that we can describe the momentum distribution of the hydride anions in La_2LiHO_3 based on phonon calculations. This observation clearly suggests that the hydride anions in La_2LiHO_3 are not mobile, as if this was the case, the measured momentum distributions would deviate from the ones calculated from phonon density of states. Thus, the NCS and QENS results are consistent and we conclude that the hydride anions in La_2LiHO_3 are not mobile. When we compare the measured momentum distribution of the hydride anions with values calculated from the Maxwell-Boltzmann approximation, we observe that the binding energy of the hydride anions is reduced with increasing temperature. Based on this we speculate whether the reduction in binding energy is what causes the oxyhydride to decompose. If we at some point reach a situation where the kinetic energy of the hydride anions is larger than the binding energy, they will become free to migrate. This scenario can indeed be the dynamic we observe in QENS and then correctly associate with the decomposition of the oxyhydride.

In this work we have concluded that the hydride anions do not diffuse in La_2LiHO_3 below the decomposition temperature despite Kobayashi et al. observed diffusion in the same compound.[19] We suggest two explanations; either the diffusion observed by Kobayashi et al. arise from vacancies in the compounds which promote diffusion, or they observed surface diffusion of either hydride anions or protons. The report by Bai et al. and our computational results suggest that vacancies are needed to promote diffusion in La_2LiHO_3.[93] Correspondingly, we may not have observed diffusion due to the absence of vacancies. The presence of vacancies is a possible

difference between the samples of Kobayashi *et al*. and those prepared in this study. However, we emphasize again that Kobayashi *et al*. reported conductivity in both the tetragonal and orthorhombic (stoichiometric) compounds. The structural investigations in this work clearly supports that the halide salt flux method yields stoichiometric oxyhydrides. It could therefore be interesting to compare structural aspects of orthorhombic La_2LiHO_3 synthesized by the high-pressure and halide salt flux methods. If vacancies in the La_2LiHO_3 oxyhydride is essential for hydride anion migration, we foresee that oxyhydrides with vacancies promoting hydride anion migration in the perovskite layer can potentially be prepared by the halide salt flux method. This requests further investigations and also opens for new neutron scattering experiments aimed to observe and study hydride anion diffusion.

To address the absence of hydride anion diffusion in La_2LiHO_3 and to fulfill the potential of the halide salt flux method to prepare oxyhydrides, we suggest a list of possible oxyhydrides in Appendix A. We consider the suggested oxyhydrides as feasible to synthesize by the halide salt flux method and the list contains both known and completely new oxyhydrides. To investigate the possibility to prepare the suggested compounds, possibly combined with a screening process based on DFT calculations, would be interesting and could potentially yield new oxyhydrides.

INS together with DFT gave useful and surprising insight to the chemical bonding in La_2LiHO_3. Material scientists are introduced to the topic of chemical bonding at an early stage in their education. One can therefore state that it is surprising that arguments based on chemical bonding can be used to gain insight to advanced materials and their properties. However, when we describe the chemical bonding in La_2LiHO_3 based on Fajans' rules, we would suggest that it is a very ionic compound.[153-155] Our DFT calculations, which is consistent with INS, describes on the other hand the bonding as partially covalent. The covalent bonding character is found in the rock salt layer, where lanthanum polarizes the bonds to oxygen, while the perovskite layer and bonding of lithium is more ionic. Thus, the bonding in La_2LiHO_3 is anisotropic.

As an alternative approach to promoting hydride anion diffusion in the perovskite layer by introducing vacancies, we can promote hydride anion diffusion into and within the rock salt layer of the RP structure as this is known to yield high conductivity in other compounds. We use our considerations about chemical bonding in La_2LiHO_3 to address the high migration barriers for hydride anion migration into and within the rock salt layer. As lanthanum polarizes the bonds in the rock salt layer, we believe that this effectively hinders the hydride anions from migrating into and within the rock salt layer and the chemical bonding in the compound is thus influencing the hydride conductive properties in a negative manner, *i.e*. we describe a strong relation between crystal structure, bonding and properties. Therefore, we suggest aims to counteract the covalent bond character in the rock salt layer. Increasing the valence of the B-cation in the oxyhydride as the low valence of lithium may allow lanthanum to polarize the bonds. Based on this, we suggest $Sr_2MgH_2O_2$ and $Ba_2MgH_2O_2$ as candidates which may display increased hydride anion

conductivity compared to La_2LiHO_3. We note that the suggested compounds are included in Appendix A.

PEDT was evaluated as a potential method for structural description of oxyhydrides, with La_2LiHO_3 as test object. As the technique has its basis in electron diffraction it circumvents many of the disadvantages with neutron diffraction (availability and sample quantity) and still allows refinement of fine structural parameters as oxygen occupancies and position of light atoms like hydrogen.[111, 117-118] However, determination of hydrogen is only reported in the organic compound paracetamol and cobalt aluminophosphate.[118] Hydrogen had never been observed by PEDT in the presence of an element as heavy as lanthanum before this work. The crystal structure of La_2LiHO_3 was successfully determined by treating the PEDT data within the kinematical approach, yielding similar parameters as obtained by neutron diffraction. However, as twin crystals were measured the model was inferior due to overlap between reflections from the two domains. It is therefore incorrect to state that this work illustrated the feasibility of the technique, however, we did illustrate the potential. Further tests should be carried out to conclude on the suitability of PEDT for structural description of oxyhydrides. Including twinning methods in the data treatment process/software may circumvent the encountered problems, *e.g.* methods for merohedral twinning allows for refinement of completely overlapping twin domains.

Finally, the dispersion of neutron scattering methods outlined in this work display the comprehensive information accessible with these techniques in the combination with DFT calculations. Neutron diffraction have been employed to probe the crystal and local structure, yielding accurate information not obtainable with other methods. Further, neutron spectroscopy spanning between small and large energy transfers have been employed to address aspects of chemical bonding and diffusion. These advanced techniques yield information of highest quality which few alternative methods can challenge. This basis of experimental methods can be further used for studies of oxyhydrides, mixed anion compounds and other materials in the future.

Appendix A

Table 21: Cations considered suited for taking A- and B-sites in oxyhydrides for different valences.

Valence	1+	2+	3+	4+
A (large)	Na, K, Rb	Ca, Sr, Ba	La, Ce, Pr, Nd	
B (small)	Li	Mg, Nb	Sc, Ti V Al, Y	Zr, Nb, Ta

Table 22: Suggested oxyhydrides based on the perovskite crystal structure, constructed on the suggested elements in Table 21.

	Valence of A	Valence of B	Suggestion A	Suggestion B
$ABHO_2$	0	5	-	-
	1	4	Na, K, Rb	Zr, Nb, Ta
	2	3	Ca, Sr, Ba	Sc, Ti V Al, Y
	3	2	La, Ce, Pr, Nd	Mg, Nb
	4	1	-	Li

	Valence of A	Valence of B	Suggestion A	Suggestion B
ABH_2O	0	4	-	Zr, Nb, Ta
	1	3	Na, K, Rb	Sc, Ti V Al, Y
	2	2	Ca, Sr, Ba	Mg, Nb
	3	1	La, Ce, Pr, Nd	Li

Table 23: Suggested oxyhydrides based on the RP1-type crystal structure, constructed on the suggested elements in Table 21.

	Valence of A	Valence of B	Suggestion A	Suggestion B
A_2BHO_3	0	7	-	-
	1	5	Na, K, Rb	-
	2	3	Ca, Sr, Ba	Sc, Ti V Al, Y
	3	1	La, Ce, Pr, Nd	Li

	Valence of A	Valence of B	Suggestion A	Suggestion B
$A_2BH_2O_2$	0	6	-	-
	1	4	Na, K, Rb	Zr, Nb, Ta
	2	2	Ca, Sr, Ba	Mg, Nb
	3	0	La, Ce, Pr, Nd	-

	Valence of A	Valence of B	Suggestion A	Suggestion B
A_2BH_3O	0	5	-	-
	1	3	Na, K, Rb	Sc, Ti V Al, Y
	2	1	Ca, Sr, Ba	Li
	3	-1	La, Ce, Pr, Nd	-

Appendix A

Table 24: Melting and decomposition temperature of metal hydrides. [a] refers to values from Holleman-Wiberg Inorganic Chemistry, and [b] to values from Chemistry of the Elements (pressure of 10 mmHg).[96, 167]

Hydride	Melts [a]	Decomposes [a]	Decomposes [b]
LiH	686 °C	972 °C	550 °C
NaH		425 °C	210 °C
KH		420 °C	210 °C
RbH		364 °C	170 °C
MgH_2		*ca.* 300 °C	85 °C
CaH_2		*ca.*1000 °C	885 °C
SrH_2		*ca.*1000 °C	585 °C
BaH_2		*ca.*1000 °C	230 °C
LaH_3		972 °C	

Table 25: Thermal properties of metal chlorides, all values are from Holleman-Wiberg Inorganic Chemistry.[96]

Chloride	Melts
LiCl	610 °C
NaCl	808 °C
KCl	772 °C
RbCl	717 °C
$MgCl_2$	708 °C
$CaCl_2$	772 °C
$SrCl_2$	873 °C
$BaCl_2$	963 °C
$LaCl_3$	860 °C

References

1.	Granger P.; Parvulescu V. I. ; W., P., *Perovskites and Related Mixed Oxides*. Wiley-VCH Verlag GmbH & Company KGaA: 2016.

2.	Tilley, R. J. D., *Understanding Solids: The Science of Materials*. Wiley: 2005.

3.	West, A. R., *Solid State Chemistry and its Applications*. Wiley: 2014.

4.	Attfield, J. P.; Lightfoot, P.; Morris, R. E., Perovskites. *Dalton Trans.* **2015,** *44*, 10541-10542.

5.	Ishihara, T., *Perovskite Oxide for Solid Oxide Fuel Cells*. Springer US: 2009.

6.	Steele, B. C. H.; Heinzel, A., Materials for fuel-cell technologies. *Nature* **2001,** *414*, 345-352.

7.	Ramirez, A. P., Colossal magnetoresistance. *J. Phys.: Condens. Matter* **1997,** *9*, 8171-8199.

8.	Rodriguez-Martinez, L. M.; Attfield, J. P., Cation disorder and size effects in magnetoresistive manganese oxide perovskites. *Phys. Rev. B* **1996,** *54*, R15622-R15625.

9.	van Delft, D., *Freezing Physics: Hieke Kamerlingh Onnes and the Quest for Cold*. Aksant Academic Publishers: 2007.

10.	Kamerlingh Onnes, H., Further experiments with liquid helium. C. On the change of electric resistance of pure metals at very low temperatures, etc. IV. The resistance of pure mercury at helium temperatures. *Comm. Phys. Lab. Univ. Leiden* **1911,** *120b*.

11.	Kamerlingh Onnes, H., Further experiments with liquid helium. D. On the change of electric resistance of pure metals at very low temperatures, etc. V. The disappearance of the resistance of mercury. *Comm. Phys. Lab. Univ. Leiden* **1911,** *122b*.

12.	Kamerlingh Onnes, H., Further experiments with liquid helium. G. On the electrical resistance of pure metals, etc. VI. On the sudden change in the rate at which the resistance of mercury disappears. *Comm. Phys. Lab. Univ. Leiden* **1911,** *124b*.

13.	Wu, M. K.; Ashburn, J. R.; Torng, C. J.; Hor, P. H.; Meng, R. L.; Gao, L.; Huang, Z. J.; Wang, Y. Q.; Chu, C. W., Superconductivity at 93 K in a new mixed-phase Y-Ba-Cu-O compound system at ambient pressure. *Phys. Rev. Lett.* **1987,** *58*, 908-910.

14.	Sasaki, M.; Ehara, S.; Nakasato, T.; Tamakawa, Y.; Kuboya, Y.; Sugisawa, M.; Sato, T., MR of the shoulder with a 0.2-T permanent-magnet unit. *Am. J. Roentgenol.* **1990,** *154*, 777-778.

References

15. Gallop, J. C., *SQUIDs, the Josephson Effects and Superconducting Electronics*. Taylor & Francis: 1991.

16. Hannevold, L.; Nilsen, O.; Kjekshus, A.; Fjellvåg, H., Chemical vapor transport of platinum and rhodium with oxygen as transport agent. *J. Cryst. Growth* **2005,** *279*, 206-212.

17. Nowak, E. J., Prediction of platinum losses during ammonia oxidation. *Chem. Eng. Sci.* **1969,** *24*, 421-423.

18. Biausque, G.; Schuurman, Y., The reaction mechanism of the high temperature ammonia oxidation to nitric oxide over $LaCoO_3$. *J. Catal.* **2010,** *276*, 306-313.

19. Kobayashi, G.; Hinuma, Y.; Matsuoka, S.; Watanabe, A.; Iqbal, M.; Hirayama, M.; Yonemura, M.; Kamiyama, T.; Tanaka, I.; Kanno, R., Pure H^- conduction in oxyhydrides. *Science* **2016,** *351*, 1314-1317.

20. Cervera, R. B.; Miyoshi, S.; Oyama, Y.; Elammari, Y. E.; Yagi, T.; Yamaguchi, S., Perovskite-Structured $BaScO_2(OH)$ as a Novel Proton Conductor: Heavily Hydrated Phase Obtained via Low-Temperature Synthesis. *Chem. Mater.* **2013,** *25*, 1483-1489.

21. Sone, Y.; Ekdunge, P.; Simonsson, D., Proton Conductivity of Nafion 117 as Measured by a Four-Electrode AC Impedance Method. *J. Electrochem. Soc.* **1996,** *143*, 1254-1259.

22. Mitchell, R. H., *Perovskites: Modern and Ancient*. Almaz Press: 2002.

23. v. Náray-Szabó, S., Der Strukturtyp des Perowskits ($CaTiO_3$). *Naturwissenschaften* **1943,** *31*, 202-203.

24. Goldschmidt, V. M., Die Gesetze der Krystallochemie. *Naturwissenschaften* **1926,** *14*, 477-485.

25. Glazer, A., Simple ways of determining perovskite structures. *Acta Crystallogr., Sect. A* **1975,** *31*, 756-762.

26. Hodges, J. P.; Short, S.; Jorgensen, J. D.; Xiong, X.; Dabrowski, B.; Mini, S. M.; Kimball, C. W., Evolution of Oxygen-Vacancy Ordered Crystal Structures in the Perovskite Series $Sr_nFe_nO_{3n-1}$ (n=2, 4, 8, and ∞), and the Relationship to Electronic and Magnetic Properties. *J. Solid State Chem.* **2000,** *151*, 190-209.

27. Takeda, Y.; Kanno, K.; Takada, T.; Yamamoto, O.; Takano, M.; Nakayama, N.; Bando, Y., Phase relation in the oxygen nonstoichiometric system, $SrFeO_x$ ($2.5 \leq x \leq 3.0$). *J. Solid State Chem.* **1986,** *63*, 237-249.

28. Tofield, B. C.; Greaves, C.; Fender, B. E. F., The $SrFeO_{2.5}$ | $SrFeO_{3.0}$ system. Evidence of a new phase $Sr_4Fe_4O_{11}$ ($SrFeO_{2.75}$). *Mater. Res. Bull.* **1975,** *10*, 737-745.

29.   Schmidt, M.; Campbell, S. J., In situ neutron diffraction study (300–1273K) of non-stoichiometric strontium ferrite $SrFeO_x$. *J. Phys. Chem. Solids* **2002,** *63*, 2085-2092.

30.   Schmidt, M.; Campbell, S. J., Crystal and Magnetic Structures of $Sr_2Fe_2O_5$ at Elevated Temperature. *J. Solid State Chem.* **2001,** *156*, 292-304.

31.   Tsujimoto, Y.; Tassel, C.; Hayashi, N.; Watanabe, T.; Kageyama, H.; Yoshimura, K.; Takano, M.; Ceretti, M.; Ritter, C.; Paulus, W., Infinite-layer iron oxide with a square-planar coordination. *Nature* **2007,** *450*, 1062.

32.   Rao, C. N. R.; Gopalakrishnan, J., *New directions in solid state chemistry. 2nd edition*. Cambridge University Press: 1997.

33.   Töpfer, J.; Goodenough, J. B., $LaMnO_{3+\delta}$ Revisited. *J. Solid State Chem.* **1997,** *130*, 117-128.

34.   Müller, U., *Inorganic Structural Chemistry*. Wiley: 2007.

35.   Cava, R. J.; van Dover, R. B.; Batlogg, B.; Rietman, E. A., Bulk superconductivity at 36 K in $La_{1.8}Sr_{0.2}CuO_4$. *Phys. Rev. Lett.* **1987,** *58*, 408-410.

36.   Lee, D.; Lee, H., Controlling Oxygen Mobility in Ruddlesden–Popper Oxides. *Materials* **2017,** *10*, 368.

37.   McIntosh, S., Oxygen Anion Transport in Solid Oxides. In *Encyclopedia of Applied Electrochemistry*, Kreysa, G.; Ota, K.-i.; Savinell, R. F., Eds. Springer New York: New York, NY, 2014; pp 1461-1475.

38.   Cleave, A. R.; Kilner, J. A.; Skinner, S. J.; Murphy, S. T.; Grimes, R. W., Atomistic computer simulation of oxygen ion conduction mechanisms in La_2NiO_4. *Solid State Ionics* **2008,** *179*, 823-826.

39.   Kushima, A.; Parfitt, D.; Chroneos, A.; Yildiz, B.; Kilner, J. A.; Grimes, R. W., Interstitialcy diffusion of oxygen in tetragonal $La_2CoO_{4+\delta}$. *Phys. Chem. Chem. Phys.* **2011,** *13*, 2242-2249.

40.   Nagell, M. U.; Sławiński, W. A.; Vajeeston, P.; Fjellvåg, H.; Sjåstad, A. O., Temperature induced transitions in $La_4(Co_{1-x}Ni_x)_3O_{10+\delta}$; oxygen stoichiometry and mobility. *Solid State Ionics* **2017,** *305*, 7-15.

41.   Lacorre, P., Passage from T-type to T′-type arrangement by reducing $R_4Ni_3O_{10}$ to $R_4Ni_3O_8$ (R = La, Pr, Nd). *J. Solid State Chem.* **1992,** *97*, 495-500.

42.   Olafsen, A. Structure and stability of rare earth oxide carbonates: properties of Nd-based Ruddlesden-Popper type oxides. Faculty of Mathematics and Natural Sciences, University of Oslo Unipub, Oslo, 1999.

References

43.   Poltavets, V. V.; Lokshin, K. A.; Croft, M.; Mandal, T. K.; Egami, T.; Greenblatt, M., Crystal Structures of $Ln_4Ni_3O_8$ (Ln = La, Nd) Triple Layer T'-type Nickelates. *Inorg. Chem.* **2007,** *46*, 10887-10891.

44.   Lee, J. Y.; Swinnea, J. S.; Steinfink, H.; Reiff, W. M.; Pei, S.; Jorgensen, J. D., The Crystal Chemistry and Physical Properties of the Triple Layer Perovskite Intergrowths $LaSr_3Fe_3O_{10-\delta}$ and $LaSr_3(Fe_{3-x}Al_x)O_{10-\delta}$. *J. Solid State Chem.* **1993,** *103*, 1-15.

45.   Øygarden, V.; Fjellvåg, H.; Sørby, M. H.; Sjåstad, A. O., Crystal Structure of $LaSr_3Fe_3O_8(OH)_2 \cdot xH_2O$. *Inorg. Chem.* **2016,** *55*, 7630-7636.

46.   Kageyama, H.; Hayashi, K.; Maeda, K.; Attfield, J. P.; Hiroi, Z.; Rondinelli, J. M.; Poeppelmeier, K. R., Expanding frontiers in materials chemistry and physics with multiple anions. *Nat. Commun.* **2018,** *9*, 772.

47.   Atkins, P.; Overton, T., *Shriver and Atkins' Inorganic Chemistry*. OUP Oxford: 2010.

48.   Connelly, N. G.; Chemistry, R. S. o.; Hartshorn, R. M.; Damhus, T.; Pure, I. U. o.; Chemistry, A.; Hutton, A. T.; Pure, I. U. o.; Chemistry, A. C. D. o. I., *Nomenclature of Inorganic Chemistry: IUPAC recommendations 2005*. Royal Society of Chemistry Publishing/IUPAC,. 2005.

49.   Kobayashi, Y.; Hernandez, O.; Tassel, C.; Kageyama, H., New chemistry of transition metal oxyhydrides. *Sci. Technol. Adv. Mater.* **2017,** *18*, 905-918.

50.   Hayward, M. A.; Cussen, E. J.; Claridge, J. B.; Bieringer, M.; Rosseinsky, M. J.; Kiely, C. J.; Blundell, S. J.; Marshall, I. M.; Pratt, F. L., The Hydride Anion in an Extended Transition Metal Oxide Array: $LaSrCoO_3H_{0.7}$. *Science* **2002,** *295*, 1882-1884.

51.   Bridges, C. A.; Darling, G. R.; Hayward, M. A.; Rosseinsky, M. J., Electronic Structure, Magnetic Ordering, and Formation Pathway of the Transition Metal Oxide Hydride $LaSrCoO_3H_{0.7}$. *J. Am. Chem. Soc.* **2005,** *127*, 5996-6011.

52.   Bridges, C. A.; Fernandez-Alonso, F.; Goff, J. P.; Rosseinsky, M. J., Observation of Hydride Mobility in the Transition-Metal Oxide Hydride $LaSrCoO_3H_{0.7}$. *Adv. Mater* **2006,** *18*, 3304-3308.

53.   Bowman, A.; Claridge, J. B.; Rosseinsky, M. J., Anion Composition Control and Magnetic Short- and Long-Range Order in Transition Metal Oxide Hydrides. *Chem. Mater.* **2006,** *18*, 3046-3056.

54.   Helps, R. M.; Rees, N. H.; Hayward, M. A., $Sr_3Co_2O_{4.33}H_{0.84}$: An Extended Transition Metal Oxide-Hydride. *Inorg. Chem.* **2010,** *49*, 11062-11068.

55.   Sakaguchi, T.; Kobayashi, Y.; Yajima, T.; Ohkura, M.; Tassel, C.; Takeiri, F.; Mitsuoka, S.; Ohkubo, H.; Yamamoto, T.; Kim, J. e.; Tsuji, N.; Fujihara, A.; Matsushita, Y.; Hester, J.; Avdeev, M.; Ohoyama, K.; Kageyama, H., Oxyhydrides of (Ca,Sr,Ba)TiO$_3$ Perovskite Solid Solutions. *Inorg. Chem.* **2012,** *51*, 11371-11376.

56.   Kobayashi, Y.; Hernandez, O. J.; Sakaguchi, T.; Yajima, T.; Roisnel, T.; Tsujimoto, Y.; Morita, M.; Noda, Y.; Mogami, Y.; Kitada, A.; Ohkura, M.; Hosokawa, S.; Li, Z.; Hayashi, K.; Kusano, Y.; Kim, J. e.; Tsuji, N.; Fujiwara, A.; Matsushita, Y.; Yoshimura, K.; Takegoshi, K.; Inoue, M.; Takano, M.; Kageyama, H., An oxyhydride of BaTiO$_3$ exhibiting hydride exchange and electronic conductivity. *Nat. Mater.* **2012,** *11*, 507-511.

57.   Yamamoto, T.; Yoshii, R.; Bouilly, G.; Kobayashi, Y.; Fujita, K.; Kususe, Y.; Matsushita, Y.; Tanaka, K.; Kageyama, H., An Antiferro-to-Ferromagnetic Transition in EuTiO$_{3-x}$H$_x$ Induced by Hydride Substitution. *Inorg. Chem.* **2015,** *54*, 1501-1507.

58.   Hernandez, O. J.; Geneste, G.; Yajima, T.; Kobayashi, Y.; Okura, M.; Aidzu, K.; Tassel, C.; Paofai, S.; Swain, D.; Ritter, C.; Kageyama, H., Site Selectivity of Hydride in Early-Transition-Metal Ruddlesden–Popper Oxyhydrides. *Inorg. Chem.* **2018,** *57*, 11058-11067.

59.   Denis Romero, F.; Leach, A.; Möller, J. S.; Foronda, F.; Blundell, S. J.; Hayward, M. A., Strontium Vanadium Oxide–Hydrides: "Square-Planar" Two-Electron Phases. *Angew. Chem., Int. Ed.* **2014,** *53*, 7556-7559.

60.   Bang, J.; Matsuishi, S.; Hiraka, H.; Fujisaki, F.; Otomo, T.; Maki, S.; Yamaura, J.-i.; Kumai, R.; Murakami, Y.; Hosono, H., Hydrogen Ordering and New Polymorph of Layered Perovskite Oxyhydrides: Sr$_2$VO$_{4-x}$H$_x$. *J. Am. Chem. Soc.* **2014,** *136*, 7221-7224.

61.   Yamamoto, T.; Shitara, K.; Kitagawa, S.; Kuwabara, A.; Kuroe, M.; Ishida, K.; Ochi, M.; Kuroki, K.; Fujii, K.; Yashima, M.; Brown, C. M.; Takatsu, H.; Tassel, C.; Kageyama, H., Selective Hydride Occupation in BaVO$_{3-x}$H$_x$ ($0.3 \leq x \leq 0.8$) with Face- and Corner-Shared Octahedra. *Chem. Mater.* **2018,** *30*, 1566-1574.

62.   Katayama, T.; Chikamatsu, A.; Kamisaka, H.; Yokoyama, Y.; Hirata, Y.; Wadati, H.; Fukumura, T.; Hasegawa, T., Topotactic synthesis of strontium cobalt oxyhydride thin film with perovskite structure. *AIP Adv.* **2015,** *5*, 107147.

63.   Onozuka, T.; Chikamatsu, A.; Katayama, T.; Fukumura, T.; Hasegawa, T., Formation of defect-fluorite structured NdNiO$_x$H$_y$ epitaxial thin films via a soft chemical route from NdNiO$_3$ precursors. *Dalton Trans.* **2016,** *45*, 12114-12118.

64.   Tassel, C.; Goto, Y.; Watabe, D.; Tang, Y.; Lu, H.; Kuno, Y.; Takeiri, F.; Yamamoto, T.; Brown, C. M.; Hester, J.; Kobayashi, Y.; Kageyama, H., High-Pressure Synthesis of Manganese Oxyhydride with Partial Anion Order. *Angew. Chem., Int. Ed.* **2016,** *128*, 9819-9822.

References

65.   Goto, Y.; Tassel, C.; Noda, Y.; Hernandez, O.; Pickard, C. J.; Green, M. A.; Sakaebe, H.; Taguchi, N.; Uchimoto, Y.; Kobayashi, Y.; Kageyama, H., Pressure-Stabilized Cubic Perovskite Oxyhydride $BaScO_2H$. *Inorg. Chem.* **2017,** *56*, 4840-4845.

66.   Takeiri, F.; Watanabe, A.; Kuwabara, A.; Nawaz, H.; Ayu, N. I. P.; Yonemura, M.; Kanno, R.; Kobayashi, G., Ba_2ScHO_3: H^- Conductive Layered Oxyhydride with H^- Site Selectivity. *Inorg. Chem.* **2019,** *58*, 4431-4436.

67.   Lun, J.; Michael, L.; Dihao, Z.; K., K. F. K.; Franz, L.; Pascal, M.; J., B. S.; E., M. J.; A., H. M., $LaSr_3NiRuO_4H_4$: A 4d Transition-Metal Oxide–Hydride Containing Metal Hydride Sheets. *Angew. Chem., Int. Ed.* **2018,** *57*, 5025-5028.

68.   Brice, J.; Brice, Synthesis and anionic conductivity of [lanthanum] hydride-oxides: LaHO, $LaH_{1+2x}O_{1-x}$, and $LaH_{1+y}O_{1-x}$ (y<2x). *Annales de chimie* **1982,** *7*, 623.

69.   Malaman, B.; Brice, J. F., Etude structurale de l'hydruro-oxyde LaHO par diffraction des rayons X et par diffraction des neutrons. *J. Solid State Chem.* **1984,** *53*, 44-54.

70.   Widerøe, M.; Fjellvåg, H.; Norby, T.; Willy Poulsen, F.; Willestofte Berg, R., NdHO, a novel oxyhydride. *J. Solid State Chem.* **2011,** *184*, 1890-1894.

71.   Yamashita, H.; Broux, T.; Kobayashi, Y.; Takeiri, F.; Ubukata, H.; Zhu, T.; Hayward, M. A.; Fujii, K.; Yashima, M.; Shitara, K.; Kuwabara, A.; Murakami, T.; Kageyama, H., Chemical Pressure-Induced Anion Order–Disorder Transition in LnHO Enabled by Hydride Size Flexibility. *J. Am. Chem. Soc.* **2018,** *140*, 11170-11173.

72.   Zapp, N.; Kohlmann, H., The lanthanide hydride oxides SmHO and HoHO. In *Zeitschrift für Naturforschung B*, 2018; Vol. 73, p 535.

73.   Ueda, J.; Matsuishi, S.; Tokunaga, T.; Tanabe, S., Preparation, electronic structure of gadolinium oxyhydride and low-energy 5d excitation band for green luminescence of doped Tb^{3+} ions. *J. Phys. Chem. C* **2018,** *6*, 7541-7548.

74.   Schwarz, H., *Neuartige Hydrid-Oxide der Seltenen Erden: Ln_2LiHO_3 mit Ln = La, Ce, Pr und Nd*. Karlsruhe, 1991.

75.   Iwasaki, Y.; Matsui, N.; Suzuki, K.; Hinuma, Y.; Yonemura, M.; Kobayashi, G.; Hirayama, M.; Tanaka, I.; Kanno, R., Synthesis, crystal structure, and ionic conductivity of hydride ion-conducting Ln_2LiHO_3 (Ln = La, Pr, Nd) oxyhydrides. *J. Mater. Chem. A* **2018,** *6*, 23457-23463.

76.   Watanabe, A.; Kobayashi, G.; Matsui, N.; Yonemura, M.; Kubota, A.; Suzuki, K.; Hirayama, M.; Kanno, R., Ambient Pressure Synthesis and H^- Conductivity of $LaSrLiH_2O_2$. *Electrochemistry* **2017,** *85*, 88-92.

77.   Huang, B.; Corbett, J. D., Ba3AlO4H: Synthesis and Structure of a New Hydrogen-Stabilized Phase. *J. Solid State Chem.* **1998,** *141*, 570-575.

78.   Huang, B.; Corbett, J. D., Ba21Ge2O5H24 and Related Phases. A Corrected Structure Type and Composition for a Zintl Phase Stabilized by Hydrogen. *Inorg. Chem.* **1998,** *37*, 1892-1899.

79.   Jehle, M.; Hoffmann, A.; Kohlmann, H.; Scherer, H.; Röhr, C., The 'sub' metallide oxide hydrides and (M = Zn, Cd, Hg, In, Tl, Si, Ge, Sn, Pb, As, Sb, Bi). *J. Alloys Compd.* **2015,** *623*, 164-177.

80.   Shannon, R., Revised effective ionic radii and systematic studies of interatomic distances in halides and chalcogenides. *Acta Crystallogr., Sect. A* **1976,** *32*, 751-767.

81.   Tassel, C.; Goto, Y.; Kuno, Y.; Hester, J.; Green, M.; Kobayashi, Y.; Kageyama, H., Direct Synthesis of Chromium Perovskite Oxyhydride with a High Magnetic-Transition Temperature. *Angew. Chem., Int. Ed.* **2014**, 10377-10380.

82.   Blundell, S. J.; Marshall, I. M.; Pratt, F. L.; Hayward, M. A.; Cussen, E. J.; Claridge, J. B.; Bieringer, M.; Kiely, C. J.; Rosseinsky, M. J., Magnetism in oxide chains bridged with the hydride anion: $LaSrCoO_3H_{0.7}$ studied using muon-spin rotation. *Phys. B (Amsterdam, Neth.)* **2003,** *326*, 527-531.

83.   Nedumkandathil, R.; Jaworski, A.; Grins, J.; Bernin, D.; Karlsson, M.; Eklöf-Österberg, C.; Neagu, A.; Tai, C.-W.; Pell, A. J.; Häussermann, U., Hydride Reduction of $BaTiO_3$ − Oxyhydride Versus O Vacancy Formation. *ACS Omega* **2018,** *3*, 11426-11438.

84.   Zhang, J.; Gou, G.; Pan, B., Study of Phase Stability and Hydride Diffusion Mechanism of $BaTiO_3$ Oxyhydride from First-Principles. *J. Phys. Chem. C* **2014,** *118*, 17254-17259.

85.   Liu, X.; Bjorheim, T. S.; Haugsrud, R., Formation and migration of hydride ions in $BaTiO_{3-x}H_x$ oxyhydride. *J. Mater. Chem. A* **2017,** *5*, 1050-1056.

86.   Eklöf-Österberg, C.; Nedumkandathil, R.; Häussermann, U.; Jaworski, A.; Pell, A. J.; Tyagi, M.; Jalarvo, N. H.; Frick, B.; Faraone, A.; Karlsson, M., Dynamics of Hydride Ions in Metal Hydride-Reduced $BaTiO_3$ Samples Investigated with Quasielastic Neutron Scattering. *J. Phys. Chem. C* **2018,** *123*, 2019-2030.

87.   Tang, Y.; Kobayashi, Y.; Shitara, K.; Konishi, A.; Kuwabara, A.; Nakashima, T.; Tassel, C.; Yamamoto, T.; Kageyama, H., On Hydride Diffusion in Transition Metal Perovskite Oxyhydrides Investigated via Deuterium Exchange. *Chem. Mater.* **2017,** *29*, 8187-8194.

88.   Takeiri, F.; Aidzu, K.; Yajima, T.; Matsui, T.; Yamamoto, T.; Kobayashi, Y.; Hester, J.; Kageyama, H., Promoted Hydride/Oxide Exchange in $SrTiO_3$ by Introduction

References

of Anion Vacancy via Aliovalent Cation Substitution. *Inorg. Chem.* **2017,** *56*, 13035-13040.

89.   Liu, X.; Bjørheim, T. S.; Vines, L.; Fjellvåg, Ø. S.; Granerød, C.; Prytz, Ø.; Yamamoto, T.; Kageyama, H.; Norby, T.; Haugsrud, R., Highly Correlated Hydride Ion Tracer Diffusion in $SrTiO_{3-x}H_x$ Oxyhydrides. *J. Am. Chem. Soc.* **2019,** *141*, 4653-4659.

90.   Kobayashi, Y.; Tang, Y.; Kageyama, T.; Yamashita, H.; Masuda, N.; Hosokawa, S.; Kageyama, H., Titanium-Based Hydrides as Heterogeneous Catalysts for Ammonia Synthesis. *J. Am. Chem. Soc.* **2017,** *139*, 18240-18246.

91.   Tang, Y.; Kobayashi, Y.; Tassel, C.; Yamamoto, T.; Kageyama, H., Hydride-Enhanced CO_2 Methanation: Water-Stable $BaTiO_{2.4}H_{0.6}$ as a New Support. *Adv. Energy Mater.* **2018,** *8*, 1800800.

92.   Liu, X.; Bjorheim, T. S.; Haugsrud, R., Formation of defects and their effects on hydride ion transport properties in a series of K_2NiF_4-type oxyhydrides. *J. Mater. Chem. A* **2018,** *6*, 1454-1461.

93.   Bai, Q.; He, X.; Zhu, Y.; Mo, Y., First-Principles Study of Oxyhydride H^- Ion Conductors: Toward Facile Anion Conduction in Oxide-Based Materials. *ACS Appl. Energy Mater.* **2018,** *1*, 1626-1634.

94.   Schubert, U.; Hüsing, N., *Synthesis of Inorganic Materials*. Wiley: 2012.

95.   Badding, J. V., High-pressure synthesis, characterization and tuning of solid state materials *Annu. Rev. Mater. Sci.* **1998,** *28*, 631-658.

96.   Holleman, A. F.; Wiberg, E.; Wiberg, N.; Eagleson, M.; Brewer, W., *Inorganic Chemistry*. Academic Press: 2001.

97.   Kimura, T., Molten Salt Synthesis of Ceramic Powders. In *Advances in Ceramics*, Sikalidis, C., Ed. IntechOpen: 2011.

98.   Xue, P.; Wu, H.; Lu, Y.; Zhu, X., Recent progress in molten salt synthesis of low-dimensional perovskite oxide nanostructures, structural characterization, properties, and functional applications: A review. *J. Mater. Sci. Technol. (Shenyang, China)* **2018,** *34*, 914-930.

99.   Matsui, N.; Kobayashi, G.; Suzuki, K.; Watanabe, A.; Kubota, A.; Iwasaki, Y.; Yonemura, M.; Hirayama, M.; Kanno, R., Ambient pressure synthesis of La_2LiHO_3 as a solid electrolyte for a hydrogen electrochemical cell. *J. Am. Ceram. Soc.* **2018,** *0*.

100.   Willis, B. T. M.; Willis, B. T. M.; Carlile, C. J., *Experimental Neutron Scattering*. OUP Oxford: 2009.

101.   Fernandez-Alonso, F.; Price, D. L., *Neutron Scattering – Fundamentals*. Elsevier Science: 2013.

102.   Dinnebier, R. E.; Billinge, S. J. L.; Bail, A. L., *Powder Diffraction: Theory and Practice*. Royal Society of Chemistry: 2008.

103.   Bacon, G. E., *Neutron Scattering in Chemistry*. Butterworth-Heinemann Limited: 1977.

104.   Als-Nielsen, J.; McMorrow, D., *Elements of Modern X-ray Physics*. Wiley: 2011.

105.   Goldstein, J. I.; Newbury, D. E.; Michael, J. R.; Ritchie, N. W. M.; Scott, J. H. J.; Joy, D. C., *Scanning Electron Microscopy and X-Ray Microanalysis*. Springer New York: 2017.

106.   Blundell, S., *Magnetism in Condensed Matter*. OUP Oxford: 2001.

107.   Kittel, C., *Introduction to Solid State Physics*. Wiley: 2004.

108.   Kubin, M.; Kern, J.; Guo, M.; Källman, E.; Mitzner, R.; Yachandra, V. K.; Lundberg, M.; Yano, J.; Wernet, P., X-ray-induced sample damage at the Mn L-edge: a case study for soft X-ray spectroscopy of transition metal complexes in solution. *Phys. Chem. Chem. Phys.* **2018,** *20*, 16817-16827.

109.   Eckert, J., Theoretical introduction to neutron scattering spectroscopy. *Spectrochimica Acta Part A: Molecular Spectroscopy* **1992,** *48*, 271-283.

110.   Castellanos, M. M.; McAuley, A.; Curtis, J. E., Investigating Structure and Dynamics of Proteins in Amorphous Phases Using Neutron Scattering. *Comput. Struct. Biotechnol. J.* **2017,** *15*, 117-130.

111.   Palatinus, L.; Correa, C. A.; Steciuk, G.; Jacob, D.; Roussel, P.; Boullay, P.; Klementova, M.; Gemmi, M.; Kopecek, J.; Domeneghetti, M. C.; Camara, F.; Petricek, V., Structure refinement using precession electron diffraction tomography and dynamical diffraction: tests on experimental data. *Acta Crystallogr., Sect. B* **2015,** *71*, 740-751.

112.   Williams, D. B.; Carter, C. B., *Transmission Electron Microscopy: A Textbook for Materials Science*. Springer: 2009.

113.   Zuo, J. M.; Rouviére, J. L., Solving difficult structures with electron diffraction. *IUCrJ* **2015,** *2*, 7-8.

114.   Kolb, U.; Gorelik, T.; Kübel, C.; Otten, M. T.; Hubert, D., Towards automated diffraction tomography: Part I—Data acquisition. *Ultramicroscopy* **2007,** *107*, 507-513.

115.   Kolb, U.; Gorelik, T.; Otten, M. T., Towards automated diffraction tomography. Part II—Cell parameter determination. *Ultramicroscopy* **2008,** *108*, 763-772.

References

116.   Mugnaioli, E.; Gorelik, T.; Kolb, U., "Ab initio" structure solution from electron diffraction data obtained by a combination of automated diffraction tomography and precession technique. *Ultramicroscopy* **2009,** *109*, 758-765.

117.   Palatinus, L.; Petricek, V.; Correa, C. A., Structure refinement using precession electron diffraction tomography and dynamical diffraction: theory and implementation. *Acta Crystallogr., Sect. A* **2015,** *71*, 235-244.

118.   Palatinus, L.; Brázda, P.; Boullay, P.; Perez, O.; Klementová, M.; Petit, S.; Eigner, V.; Zaarour, M.; Mintova, S., Hydrogen positions in single nanocrystals revealed by electron diffraction. *Science* **2017,** *355*, 166-169.

119.   Rietveld, H., A profile refinement method for nuclear and magnetic structures. *J. Appl. Crystallogr.* **1969,** *2*, 65-71.

120.   Young, R. A., *The Rietveld Method*. Oxford University Press: 1995.

121.   Stinton, G. W.; Evans, J. S. O., Parametric Rietveld refinement. *J. Appl. Crystallogr.* **2007,** *40*, 87-95.

122.   Bruker-AXS *TOPAS V5: General profile and structure analysis software for powder diffraction data, Bruker AXS, Karlsruhe, Germany.*, 2013.

123.   Coelho, A., TOPAS and TOPAS-Academic: an optimization program integrating computer algebra and crystallographic objects written in C++. *J. Appl. Crystallogr.* **2018,** *51*, 210-218.

124.   Neder, R. B.; Proffen, T., *Diffuse Scattering and Defect Structure Simulations: A Cook Book Using the Program DISCUS*. OUP Oxford: 2008.

125.   Slawinski, W. A.; Fjellvåg, Ø. S.; Ruud, A.; Fjellvåg, H., A novel polytype - the stacking fault based γ-MoO$_3$ nanobelts. *Acta Crystallogr., Sect. B* **2016,** *72*, 201-208.

126.   Egami, T.; Billinge, S. J. L., *Underneath the Bragg Peaks: Structural Analysis of Complex Materials*. Elsevier Science: 2003.

127.   Nield, V. M.; Keen, D. A., *Diffuse Neutron Scattering from Crystalline Materials*. Clarendon Press: 2001.

128.   Keen, D., A comparison of various commonly used correlation functions for describing total scattering. *J. Appl. Crystallogr.* **2001,** *34*, 172-177.

129.   Slawinski, W., Calculation of pair distribution functions for multiphase systems. *J. Appl. Crystallogr.* **2018,** *51*, 919-923.

130.   Masadeh, A. S., Total scattering atomic pair distribution function: new methodology for nanostructure determination. *J. Exp. Nanosci.* **2016,** *11*, 951-974.

131. Farrow, C. L.; Juhas, P.; Liu, J. W.; Bryndin, D.; Božin, E. S.; Bloch, J.; Th, P.; Billinge, S. J. L., PDFfit2 and PDFgui: computer programs for studying nanostructure in crystals. *J. Phys.: Condens. Matter* **2007,** *19*, 335219.

132. Matthew, G. T.; David, A. K.; Martin, T. D.; Andrew, L. G.; Qun, H., RMCProfile: reverse Monte Carlo for polycrystalline materials. *J. Phys.: Condens. Matter* **2007,** *19*, 335218.

133. Qun, H.; Matthew, G. T.; Martin, T. D.; Stephen, A. W.; David, A. K., Total scattering and reverse Monte Carlo study of the 105 K displacive phase transition in strontium titanate. *J. Phys.: Condens. Matter* **2005,** *17*, S111.

134. Andreani, C.; Krzystyniak, M.; Romanelli, G.; Senesi, R.; Fernandez-Alonso, F., Electron-volt neutron spectroscopy: beyond fundamental systems. *Adv. Phys.* **2017,** *66*, 1-73.

135. Haines, P. J., *Thermal Methods of Analysis: Principles, Applications and Problems*. Springer Netherlands: 2012.

136. Karen, P., Nonstoichiometry in oxides and its control. *J. Solid State Chem.* **2006,** *179*, 3167-3183.

137. Basin, A. S.; Kaplun, A. B.; Meshalkin, A. B.; Uvarov, N. F., The LiCl-KCl binary system. *Russ. J. Inorg. Chem.* **2008,** *53*, 1509-1511.

138. Fjellvåg, Ø. S.; Nygård, K. H.; Vajeeston, P.; Sjåstad, A. O., Advances in the LiCl salt flux method and the preparation of phase pure $La_{2-x}Nd_xLiHO_3$ ($0 \leq x \leq 2$) oxyhydrides. *Chemical Communications* **2019,** *55*, 3817-3820.

139. Hull, S.; Smith, R. I.; David, W. I. F.; Hannon, A. C.; Mayers, J.; Cywinski, R., The Polaris powder diffractometer at ISIS. *Phys. B (Amsterdam, Neth.)* **1992,** *180-181*, 1000-1002.

140. Hauback, B. C.; Fjellvåg, H.; Steinsvoll, O.; Johansson, K.; Buset, O. T.; Jørgensen, J., The high resolution Powder Neutron Diffractometer PUS at the JEEP II reactor at Kjeller in Norway. *J. Neutron Res.* **2000,** *8*, 215-232.

141. Fjellvåg, Ø. S.; Armstrong, J.; Sławiński, W. A.; Sjåstad, A. O., Thermal and Structural Aspects of the Hydride-Conducting Oxyhydride La_2LiHO_3 Obtained via a Halide Flux Method. *Inorg. Chem.* **2017,** *56*, 11123-11128.

142. Petříček, V.; Dušek, M.; Palatinus, L., Crystallographic Computing System JANA2006: General features. In *Zeitschrift für Kristallographie - Crystalline Materials*, 2014; Vol. 229, p 345.

143. Sears, V. F., Neutron scattering lengths and cross sections. *Neutron News* **1992,** *3*, 26-37.

144. Vegard, L., Die Konstitution der Mischkristalle und die Raumfüllung der Atome. *Zeitschrift für Physik* **1921,** *5*, 17-26.

145. Rayner-Canham, G.; Overton, T., *Descriptive Inorganic Chemistry*. W. H. Freeman: 2009.

146. Attfield, J. P.; Férey, G., Preparation and crystal structures of $La_2Cu_{1-x}Li_xO_4$ solid solutions and evidence for a new oxide with a defect K_2NiF_4 structure: $La_4Li_2O_7$. *J. Solid State Chem.* **1989,** *80*, 112-119.

147. Stokes, H. T.; Hatch, D. M.; Campbell, B. J.; Tanner, D. E., ISODISPLACE: a web-based tool for exploring structural distortions. *J. Appl. Crystallogr.* **2006,** *39*, 607-614.

148. Telling, M. T. F.; Andersen, K. H., Spectroscopic characteristics of the OSIRIS near-backscattering crystal analyser spectrometer on the ISIS pulsed neutron source. *Phys. Chem. Chem. Phys.* **2005,** *7*, 1255-1261.

149. Carlile, C. J.; Adams, M. A., The design of the IRIS inelastic neutron spectrometer and improvements to its analysers. *Phys. B (Amsterdam, Neth.)* **1992,** *182*, 431-440.

150. Campbell, S. I.; Telling, M. T. F.; Carlile, C. J., The optimisation of analyser geometry in near-backscattering spectrometers – IRIS on the ISIS-pulsed source. *Phys. B (Amsterdam, Neth.)* **2000,** *276-278*, 206-207.

151. Fjellvåg, Ø. S.; Armstrong, J.; Vajeeston, P.; Sjåstad, A. O., New Insights into Hydride Bonding, Dynamics, and Migration in La_2LiHO_3 Oxyhydride. *J. Phys. Chem. Lett.* **2018,** *9*, 353-358.

152. Sholl, D.; Steckel, J. A., *Density Functional Theory: A Practical Introduction*. Wiley: 2009.

153. Fajans, K., Struktur und Deformation der Elektronenhüllen in ihrer Bedeutung für die chemischen und optischen Eigenschaften anorganischer Verbindungen. *Naturwissenschaften* **1923,** *11*, 165-172.

154. Fajans, K.; Joos, G., Molrefraktion von Ionen und Molekülen im Lichte der Atomstruktur. *Zeitschrift für Physik* **1924,** *23*, 1-46.

155. Fajans, K., II. Die Eigenschaften salzartiger Verbindungen und Atombau. In *Zeitschrift für Kristallographie - Crystalline Materials*, 1924; Vol. 61, pp 18-48.

156. Krzystyniak, M.; Romanelli, G.; Fabian, M.; Gutmann, M.; Festa, G.; Arcidiacono, L.; Gigg, M.; Drużbicki, K.; Andreani, C.; Senesi, R.; Fernandez-Alonso, F., VESUVIO+: The Current Testbed for a Next-generation Epithermal Neutron Spectrometer. *J. Phys.: Conf. Ser.* **2018,** *1021*, 012026.

157.   Romanelli, G.; Krzystyniak, M.; Festa, G.; Andreani, C.; Fernandez-Alonso, F.; Senesi, R., The road to a station for epithermal and thermal neutron analysis. *J. Phys.: Conf. Ser.* **2018,** *1055*, 012017.

158.   Fernandez-Alonso, F.; Price, D. L., *Neutron Scattering – Applications in Biology, Chemistry, and Materials Science*. Elsevier Science: 2017.

159.   Krzystyniak, M.; Drużbicki, K.; Romanelli, G.; Gutmann, M. J.; Rudić, S.; Imberti, S.; Fernandez-Alonso, F., Nuclear dynamics and phase polymorphism in solid formic acid. *Phys. Chem. Chem. Phys.* **2017,** *19*, 9064-9074.

160.   Krzystyniak, M.; Seel, A. G.; Richards, S. E.; Gutmann, M. J.; Fernandez-Alonso, F., Mass-selective Neutron Spectroscopy Beyond the Proton. *J. Phys.: Conf. Ser.* **2014,** *571*, 012002.

161.   Andreani, C.; Ceriotti, M.; Chass, G.; Drechsel-Grau, C.; Fernandez-Alonso, F.; Greaves, N.; Gidopolous, N.; Krzystyniak, M.; Parmentier, A.; Refson, K.; Reiter, G. F.; Romanelli, G.; Seel, A.; Walewski, L.; Wiles, T., Discussion: Nuclear Quantum Dynamics - Protons and Beyond. *J. Phys.: Conf. Ser.* **2014,** *571*, 012004.

162.   Barrier, N.; Pelloquin, D.; Nguyen, N.; Giot, M.; Bourée, F.; Raveau, B., Ferrite $Sr_3NdFe_3O_9$: An Original Intergrowth between the Brownmillerite and K_2NiF_4-type Structures. *Chem. Mater.* **2005,** *17*, 6619-6623.

163.   Pelloquin, D.; Hadermann, J.; Giot, M.; Caignaert, V.; Michel, C.; Hervieu, M.; Raveau, B., Novel, Oxygen-Deficient n = 3 RP-Member $Sr_3NdFe_3O_{9-\delta}$ and Its Topotactic Derivatives. *Chem. Mater.* **2004,** *16*, 1715-1724.

164.   Fjellvåg, Ø. S.; Øygarden, V.; Sørby, M. H.; Sjåstad, A. O., Crystal structure of $LaSr_3Fe_3O_9$ and its phase relation with $LaSr_3Fe_3O_{10}$. *J. Solid State Chem.* **2019,** *275*, 56-62.

165.   Tsipis, E. V.; Naumovich, E. N.; Patrakeev, M. V.; Anikina, P. V.; Waerenborgh, J. C.; Kharton, V. V., Defect Interactions in $Sr_3La(Fe,Al)_3O_{10-\delta}$ by Computer Simulations and Mössbauer Spectroscopy. *Chem. Mater.* **2009,** *21*, 5072-5078.

166.   Brown, I. D.; Altermatt, D., Bond-valence parameters obtained from a systematic analysis of the Inorganic Crystal Structure Database. *Acta Crystallogr., Sect. B* **1985,** *41*, 244-247.

167.   Greenwood, N. N.; Earnshaw, A., *Chemistry of the Elements*. Elsevier Science: 2012.

Paper I

I

Thermal and Structural Aspect of the Hydride Conducting Oxyhydride La$_2$LiHO$_3$ obtained via a Halide Flux Method

ØS Fjellvåg, J Armstrong, WA Sławiński, AO Sjåstad

Paper II

Advances on the LiCl salt flux method and the preparation of phase pure La$_{2-x}$Nd$_x$LiHO$_3$

ØS Fjellvåg, KH Nygård, P Vajeeston, AO Sjåstad

II

II

Check for updates

Advances in the LiCl salt flux method and the preparation of phase pure La₂₋ₓNdₓLiHO₃ (0 ≤ x ≤ 2) oxyhydrides†

Øystein Slagtern Fjellvåg, [ID]* Kristin Hubred Nygård, Ponniah Vajeeston [ID] and Anja Olafsen Sjåstad*

The LiCl salt flux method is an established aid in oxyhydride synthesis. By operating the flux below its melting point, we have obtained phase pure Nd_2LiHO_3 for the first time. Further, the suitability of the flux method is shown to be dictated by a delicate balance between the thermal stability of the oxyhydride in question and the ionic mobility of the reactants.

Within technology and the academic community, oxyhydrides are emerging as a new class of materials. In contrast to traditional ionic conductors, conducting ions such as H^+, Li^+ and O^{2-}, oxyhydrides conduct H^-. The chemistry of oxyhydrides is exotic due to their rare combination of anions, as the anion lattice is composed of both O^{2-} and H^-. A very limited number of reported oxyhydrides are at hand, which is a good indicator of the difficulty in synthesizing these compounds.[1] One key challenge in the preparation work is the very reducing nature of the hydride anion. More insight and development of the preparation routes of oxyhydrides are required to add new members to this material class.

Oxyhydrides described by the general formula $Ln_{2-x-y}A_{x+y}LiH_{1-x-y}O_{3-y}$ (Ln = rare earth elements; A = alkaline earth elements) attract attention as a result of Kobayashi *et al.*'s documentation of pure H^- conductivity, and their proof-of-concept demonstration of oxyhydrides' suitability as electrolytes in batteries.[2] This report is followed by several computational investigations of the diffusional properties of the hydride anions in the lattice.[3–5] However, to explore functional properties in detail, phase pure samples in reasonable quantity (on a gram scale) are a prerequisite. For this reason, full control and understanding of the synthesis become indispensable.

Ln_2LiHO_3 (Ln = La, Ce, Pr and Nd) oxyhydrides take an orthorhombic K_2NiF_4-type structure (Ruddlesden–Popper; $n = 1$).

Centre for Materials Science and Nanotechnology, Department of Chemistry, University of Oslo, P. O. Box 1033, N-0315 Oslo, Norway.
E-mail: o.s.fjellvag@smn.uio.no, a.o.sjastad@kjemi.uio.no

† Electronic supplementary information (ESI) available. See DOI: 10.1039/c9cc00920e

In their crystal structure the oxide and hydride anions are ordered in the equatorial positions in the octahedron coordinating lithium, making the structure orthorhombic (*Immm*).[6] A tetragonal hydride anion deficient analogue (*I4/mmm*) is also reported in the system, with the nominal formula $La_2Li(H_{0.53}O_{1.21}\square_{0.26})O_2$ (□ denotes vacancies).[2]

Conventional ceramic synthesis has not proven successful for the preparation of Ln_2LiHO_3 oxyhydrides; however, several methods are well-established: the LiCl salt flux method, the ceramic method under a H_2-atmosphere, the high-pressure ceramic method and the ceramic based LiH self-flux method.[2,6–10] The different methods all have their pros and cons. The LiCl salt flux method and the ceramic method in a H_2-atmosphere provide large sample quantities (on a gram scale), but suffer from only La_2LiHO_3 being prepared without impurities.[6,7] Recently, Pr_2LiHO_3 and Nd_2LiHO_3 were prepared by the high-pressure ceramic method.[9] The high-pressure method is a solid–solid reaction, similar to the ceramic method; however, high pressure stabilizes oxyhydrides at moderate temperature. A drawback is that the method only provides small sample quantities (on a mg scale). Notably, in parallel to our work, Matsui *et al.*[8] prepared La_2LiHO_3 by a so-called LiH self-flux method, which documents and supports our findings. However, the possibility of lowering the synthesis temperature significantly was not realized and investigated.[8] Although the LiH-self-flux route allows upscaling, ceramic reactions with large quantities of LiH are not very attractive with respect to safety.

The present study addresses a modified LiCl salt flux route for the synthesis of phase pure Ln_2LiHO_3 (Ln = La, Nd) in large quantities, including evaluation of the required delicate balance over a wide range of synthesis temperatures, to meet the requirements of being within the thermal stability window of the compound, and at the same time maintaining sufficient ionic mobility for mixing at an atomic level. We postulate that our findings on the suitability of operating the flux far below its melting point give us completely new opportunities to discover so far unknown oxyhydrides, which normally have restricted thermal stability. In addition, a full structural analysis of $LaNdLiHO_3$
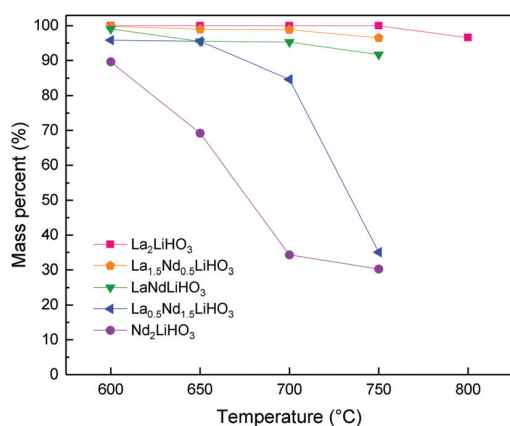
Fig. 1 Quantity (mass%) of the desired phase, La$_{2-x}$Nd$_x$LiHO$_3$ ($0 \leq x \leq 2$), as a function of temperature. Impurity phases are Ln$_2$O$_3$ and LnHO.

based on neutron diffraction is included together with a mapping of the thermal stability of La$_{2-x}$Nd$_x$LiHO$_3$.

Schwartz successfully synthesized La$_2$LiHO$_3$ at 750 °C with a 1:4 molar ratio between La$_2$O$_3$ and LiH in a LiCl salt flux.[6] Earlier studies have synthesized gram batches of single phase orthorhombic La$_2$LiHO$_3$ between 600 and 750 °C using different ratios between La$_2$O$_3$ and LiH.[10] By preparing selected members in the La$_{2-x}$Nd$_x$LiHO$_3$ series ($0 \leq x \leq 2$), over a large temperature range, limited by the melting point of LiCl (605 °C)[11] and the maximum recommended operational temperature of the stainless steel ampoule (800 °C) used, we studied the phase content and mass percent of the targeted phase, Fig. 1. All compositions of La$_{2-x}$Nd$_x$LiHO$_3$ ($0 \leq x \leq 2$) take the orthorhombic structure. Of the five evaluated compositions, only La$_2$LiHO$_3$ became phase pure above 600 °C, while the remaining compositions contain Ln$_2$O$_3$ and LnHO as impurities.

Considering the unit cell volume (V) for the different compositions (x) of La$_{2-x}$Nd$_x$LiHO$_3$ ($0 \leq x \leq 2$), Fig. 2, we observe a linear relation between V and x. This observation is in
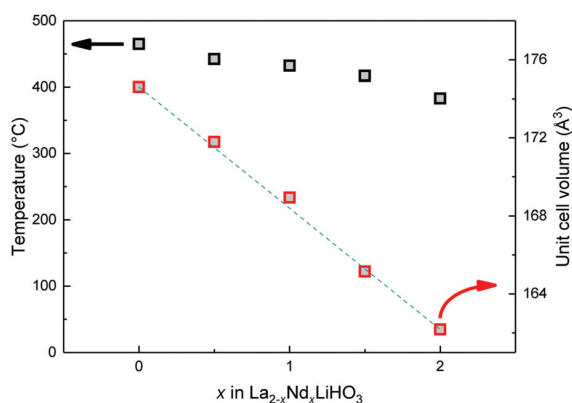
Fig. 2 Unit cell volume (red) for La$_{2-x}$Nd$_x$LiHO$_3$ ($0 \leq x \leq 2$) synthesized at 600 °C in a LiCl salt flux. The green dotted line illustrates Vegard's law; a linear relationship in cell volume for intermediate compositions in a solid solution. Decomposition temperature (black), obtained by TGA, versus x in La$_{2-x}$Nd$_x$LiHO$_3$ ($0 \leq x \leq 2$).
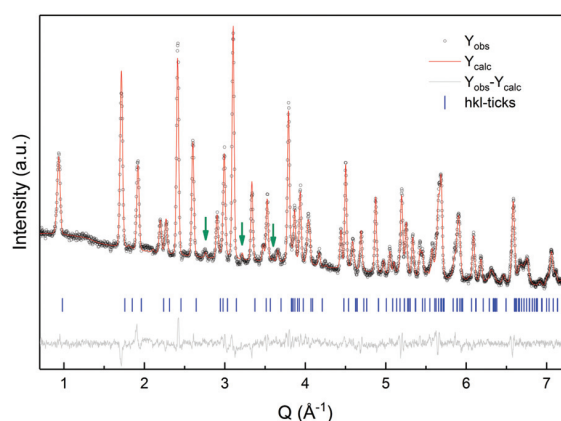
Fig. 3 Neutron diffraction pattern of LaNdLiHO$_3$ synthesized at 650 °C in LiCl. The green arrows indicate the positions of Bragg reflections from the secondary phase Ln$_2$O$_3$. Structural information from the refinement is given in Table S2 (ESI†).

accordance with Vegard's law and suggests a solid-solution in the system.[12] The contracting unit cell volume with increasing neodymium content is expected and in compliance with the lanthanide contraction.

Neutron diffraction was employed to analyse LaNdLiHO$_3$ prepared at 650 °C in LiCl salt flux, Fig. 3. Based on this, we confirm the crystal structure to accommodate hydrogen in the anionic lattice, and that LaNdLiHO$_3$ is isostructural to ortho-rhombic La$_2$LiHO$_3$, Table S1 (ESI†). The experiment further validates the solid-solution, as no signs of ordering of lanthanum and neodymium are observed. A small quantity of Ln$_2$O$_3$ is identified in the sample, in accordance with the selected synthesis conditions.

Returning to Fig. 1, two trends are evident: (1) increasing amounts of impurities with increasing neodymium content and (2) increasing amounts of impurities with increasing synthesis temperature. Based on these observations, we hypothesized for the explored nominal compositions under the used thermal conditions that all studied oxyhydrides are formed during the cooling sequence. Further, prolonged dwelling at high temperature stabilizes side products (LnHO) or induces crystallite growth of the reactants (Ln$_2$O$_3$, LiH); that is, elevated reaction temperatures suppress Ln$_2$LiHO$_3$ formation. To verify this hypothesis, we used Nd$_2$LiHO$_3$ as an indicator of success of an experiment, as this compound gave less promising results in the initial screening phase. We conducted several experiments to verify the hypothesis, Table 1.

In the case of Nd$_2$LiHO$_3$, slow cooling from high temperature (e.g. 650 °C) would indicate whether the oxyhydride is formed during the cooling process. At 650 °C, we expect about 30 mass% impurities, Fig. 1. However, by cooling the sample slowly (96 h), Nd$_2$LiHO$_3$ was prepared without any impurities for the first time by the salt flux method, Table 1. It is therefore evident that the oxyhydride phase is formed at lower temperatures than 650 °C. Correspondingly, fast cooling by quenching from 650 °C to room temperature by transferring the stainless-steel ampoule directly from 650 °C into cold water is likely to

Table 1 Experimental conditions and products obtained from selected syntheses. Quantifications are obtained by Rietveld refinements. The quenched sample was transferred directly from the furnace at 650 °C into cold water

Temperature	Flux	Dwelling	Cooling	Products
650 °C	LiCl	48 h	96 h	100 mass% Nd_2LiHO_3
650 °C	LiCl	48 h	Quenched	77 mass% Nd_2O_3
				23 mass% NdHO
700 → 550 °C	LiCl	48 h, 48 h	2 h, 3 h	71 mass% Nd_2LiHO_3
				29 mass% Nd_2O_3
550 °C	LiCl	48 h	5 h	96 mass% Nd_2LiHO_3
				3.0 mass% NdHO
				1.0 mass% Nd_2O_3
500 °C	LiCl	48 h	5 h	100 mass% Nd_2LiHO_3
500 °C	LiCl–KCl	48 h	5 h	100 mass% Nd_2LiHO_3 + KCl
400 °C	LiCl–KCl	48 h	5 h	56 mass% Nd_2O_3
				36 mass% Nd_2LiHO_3
				8.0 mass% NdHO
375 °C	LiCl–KCl	48 h	5 h	85 mass% Nd_2O_3
				15 mass% NdHO

reflect the phase content present at 650 °C. It is striking that we find no Nd_2LiHO_3 in this sample, Table 1. Instead, we observe Nd_2O_3 and NdHO. Thus, Nd_2LiHO_3 is not present in the system at 650 °C. This is in great contrast to the slow cooling (96 h), and the two experiments prove that Nd_2LiHO_3 forms below 650 °C in the LiCl salt flux. We attribute the absence of Nd_2LiHO_3 at 650 °C to exceeding the thermal stability of the oxyhydride in the flux.

The behaviour is clear; lower temperatures are key to preparing oxyhydrides without impurities. Although LiCl melts at 605 °C, we attempted to prepare Nd_2LiHO_3 at 500 and 550 °C in the hope that the salt would work as a dry flux giving improved mobility to the reactants and promote the formation of Nd_2LiHO_3. Accordingly, we find the method to yield Nd_2LiHO_3 with a low amount of secondary phases at 550 °C, and to be phase pure at 500 °C, Table 1. This complies with our hypothesis of low temperature being desirable for oxyhydride synthesis. We consider this finding as an advance; that is, we document here that phase pure materials can be obtained far below the melting temperature of the applied flux and that the flux facilitates ionic mobility also below its melting temperature. We further note that this temperature is comparable with temperatures used to obtain oxyhydrides with topotactic anion-exchange with CaH_2.[13,14] Thus, we suggest that oxyhydrides with transition metals are feasible by this "low" temperature approach, which are yet to be reported with the salt flux method.

In order to pursue the second part of the hypothesis, *i.e.* on the possible crystallite growth of the reactants in the melted flux, we performed a two-step synthesis starting at 700 °C for 48 h followed by a second holding time of 48 h at 550 °C. According to Table 1 and Fig. 1, we observed a significantly higher yield in this experiment than that in the standard 700 °C synthesis (71 mass% *versus* 34 mass%), but the yield is also substantially lower than what is obtained from direct synthesis at 550 °C (96 mass%). As the impurity phase is Nd_2O_3, our interpretation is that Nd_2O_3 undergoes crystallite growth upon long dwelling in the melt at 700 °C, which in turn slows down the subsequent transformation to Nd_2LiHO_3 at 550 °C. This explains why the sample is not fully converted after 48 h at 550 °C, compared to the one reacted directly at 550 °C for 48 h (Table 1).

We further investigated the aspects of the salt flux method by introducing an alternative eutectic salt flux, LiCl–KCl, which is a known method to decrease the working temperature of a flux.[15] With a melting point of 352 °C, the eutectic mixture allows synthesis in a molten state at lower temperatures compared to LiCl.[11] We successfully synthesized Nd_2LiHO_3 in the eutectic LiCl–KCl salt flux at 500 °C. Thus, it is evident that the alternative flux offers similar aids for the reactions as solid LiCl with respect to the mobilities of the reactants. However, at $T \leq 400$ °C, Nd_2LiHO_3 did not form without impurities. We attribute this to low mobility in the oxyhydride anion/cation lattice (see below).

According to Fig. 2, TGA documents that the thermal stability of $La_{2-x}Nd_xLiHO_3$ in air steadily decreases with increasing neodymium (x) content. Further, the thermal stability also follows the unit cell volume (V) and lanthanide contraction. To identify the origin of this trend, the heats of formation (ΔH_f) from the corresponding binary constituents *versus x* for selected compositions of $La_{2-x}Nd_xLiHO_3$ were established by DFT calculations, Fig. 4. The ΔH_f coincides with the thermal stability trend and cell volume contraction, showing less favourable heat of formation with increasing neodymium content. Furthermore, phonon calculations stating that the calculated compounds are dynamically stable, and the phonon densities of states are given in the ESI† (Fig. S1 and S2).

Ionic mobility is a prerequisite for reacting components to make a product, *i.e.* an oxyhydride. Previously, we have observed that the hydride anion mobility in the case of La_2LiHO_3 increases significantly at a temperature in the proximity of the decomposition temperature in air.[10] Relating this to the impurities observed in samples formed at $T \leq 400$ °C for Nd_2LiHO_3, we suggest that temperatures below the threshold for ionic mobility in the oxyhydride result in too slow diffusion to form the targeted phase at a satisfactory rate. Thus, prolonged dwelling is needed to form the oxyhydride phase without impurity phases at low temperatures.

To suggest guidelines for the synthesis of Ln_2LiHO_3 oxyhydrides based on our findings, we carefully evaluated the tested synthesis conditions to obtain Nd_2LiHO_3 (Table 1), and
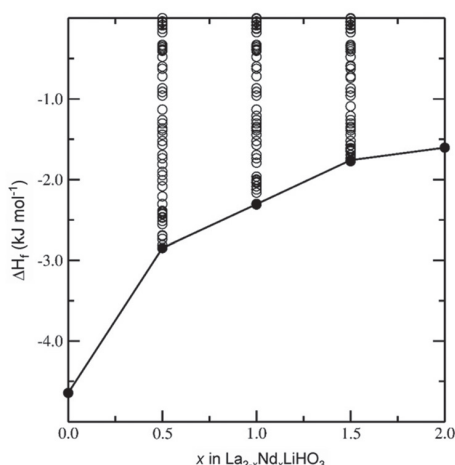
Fig. 4 Calculated heats of formation (ΔH_f) of La$_{2-x}$Nd$_x$LiHO$_3$ (x = 0, 0.5, 1.0, 1.5, 2) from the binary constituents (La$_2$O$_3$, Nd$_2$O$_3$, LiH) as a function of Nd concentration (x). The open circles correspond to the energetics of possible different atomic arrangements of La/Nd in the matrix; all the structures are generated with a random structure generator approach.

we propose that the optimal synthesis temperature is bracketed. The upper temperature limit is dictated by the decomposition temperature of the compound in the flux medium. Note that Ln$_2$LiHO$_3$ is significantly stabilized in a LiH enriched LiCl salt flux relative to air (Table 1 and Fig. 3). Correspondingly, the lower temperature limit to obtain phase pure samples is restricted by ionic mobility in the oxyhydride. By adding these observations, we state that the synthesis of an oxyhydride by the salt flux method should be performed slightly below its decomposition temperature (in the flux medium) to ensure sufficient ionic mobility, and to form the targeted phase and suppress the formation and growth of undesired phases. At lower temperatures, the ionic mobility limits the formation of the targeted oxyhydride.

Based on our findings, we may ask what would promote the synthesis of Ln$_2$LiHO$_3$ with heavier lanthanides than lanthanum and neodymium, e.g. samarium. Iwasaki et al. unsuccessfully attempted to synthesize Sm$_2$LiHO$_3$ under high-pressures at 600 °C.[9] The trends observed in this work suggest clearly that Sm$_2$LiHO$_3$ would show lower thermal stability than Nd$_2$LiHO$_3$. Correspondingly, the compound would need to be synthesized at very low temperatures to avoid impurities. With this motivation, we evaluated the stability of Sm$_2$LiHO$_3$ by DFT calculations by assuming it to be isostructural to La$_2$LiHO$_3$. Unlike in La$_2$LiHO$_3$ and Nd$_2$LiHO$_3$, we encountered negative phonon frequencies, Fig. S3 (ESI†). Therefore, we state that the formation of Sm$_2$LiHO$_3$ is not limited by the thermal stability or too high synthesis temperature, rather by the intrinsic instability of the compound. Thus, neodymium is the heaviest lanthanide to form Ln$_2$LiHO$_3$ with an RP1 type structure.

In summary, we have revisited the LiCl salt flux method and discovered its suitability as an excellent medium for preparation of oxyhydrides below its melting point (605 °C). We have found that the flux approach has an upper temperature limit,

dictated by the thermal stability of the targeted oxyhydride in the flux. Correspondingly, the lower temperature limit is controlled by ionic mobility. We anticipate that significantly lower synthesis temperatures are possible as the flux medium (solid or melt) facilitates ion transport between reactants. This knowledge is an advance in how to aid the experimental conditions in our search for new oxyhydrides. Finally, we must emphasize, based on the recent discoveries of the flux approach, that Nd$_2$LiHO$_3$ has been, for the first time, synthesized phase pure by means of a LiCl salt flux approach.

Conflicts of interest

There are no conflicts to declare.

Notes and references

1 H. Kageyama, K. Hayashi, K. Maeda, J. P. Attfield, Z. Hiroi, J. M. Rondinelli and K. R. Poeppelmeier, Nat. Commun., 2018, 9, 772.
2 G. Kobayashi, Y. Hinuma, S. Matsuoka, A. Watanabe, M. Iqbal, M. Hirayama, M. Yonemura, T. Kamiyama, I. Tanaka and R. Kanno, Science, 2016, 351, 1314–1317.
3 X. Liu, T. S. Bjorheim and R. Haugsrud, J. Mater. Chem. A, 2018, 6, 1454–1461.
4 Ø. S. Fjellvåg, J. Armstrong, P. Vajeeston and A. O. Sjåstad, J. Phys. Chem. Lett., 2018, 9, 353–358.
5 Q. Bai, X. He, Y. Zhu and Y. Mo, ACS Appl. Energy Mater., 2018, 1, 1626–1634.
6 H. Schwarz, Neuartige Hydrid-Oxide der Seltenen Erden: Ln$_2$LiHO$_3$ mit Ln = La, Ce, Pr und Nd, Karlsruhe, 1991.
7 A. Watanabe, G. Kobayashi, N. Matsui, M. Yonemura, A. Kubota, K. Suzuki, M. Hirayama and R. Kanno, Electrochemistry, 2017, 85, 88–92.
8 N. Matsui, G. Kobayashi, K. Suzuki, A. Watanabe, A. Kubota, Y. Iwasaki, M. Yonemura, M. Hirayama and R. Kanno, J. Am. Ceram. Soc., 2018, 1–8.
9 Y. Iwasaki, N. Matsui, K. Suzuki, Y. Hinuma, M. Yonemura, G. Kobayashi, M. Hirayama, I. Tanaka and R. Kanno, J. Mater. Chem. A, 2018, 6, 23457–23463.
10 Ø. S. Fjellvåg, J. Armstrong, W. A. Sławiński and A. O. Sjåstad, Inorg. Chem., 2017, 56, 11123–11128.
11 A. S. Basin, A. B. Kaplun, A. B. Meshalkin and N. F. Uvarov, Russ. J. Inorg. Chem., 2008, 53, 1509–1511.
12 L. Vegard, Z. Phys., 1921, 5, 17–26.
13 M. A. Hayward, E. J. Cussen, J. B. Claridge, M. Bieringer, M. J. Rosseinsky, C. J. Kiely, S. J. Blundell, I. M. Marshall and F. L. Pratt, Science, 2002, 295, 1882–1884.
14 Y. Kobayashi, O. J. Hernandez, T. Sakaguchi, T. Yajima, T. Roisnel, Y. Tsujimoto, M. Morita, Y. Noda, Y. Mogami, A. Kitada, M. Ohkura, S. Hosokawa, Z. Li, K. Hayashi, Y. Kusano, J. e. Kim, N. Tsuji, A. Fujiwara, Y. Matsushita, K. Yoshimura, K. Takegoshi, M. Inoue, M. Takano and H. Kageyama, Nat. Mater., 2012, 11, 507–511.
15 D. E. Bugaris and H.-C. zur Loye, Angew. Chem., Int. Ed., 2012, 51, 3780–3811.

Advances on the LiCl salt flux method and the preparation of phase pure $La_{2-x}Nd_xLiHO_3$ $(0 \leq x \leq 2)$ oxyhydrides

Øystein Slagtern Fjellvåg,[*a] Kristin Hubred Nygård,[a] Ponniah Vajeeston,[a] and Anja Olafsen Sjåstad[*a]

[a] Centre for Materials Science and Nanotechnology, Department of Chemistry, University of Oslo, P. O. Box 1033, N-0315 Oslo, Norway.

E-mail: o.s.fjellvag@smn.uio.no; a.o.sjastad@kjemi.uio.no

Experimental:

The oxyhydrides $La_{2-x}Nd_xHO_3$ $(0 \leq x \leq 2)$ were prepared from the binary oxides La_2O_3 (Molycorp 99.99 %) and Nd_2O_3 (Molycorp 99.9 %). Prior to synthesis, the oxides were dried at 1100 °C for 12 hours and transferred directly into an argon filled glove box (MBraun) to avoid hydration. LiCl and KCl (both Sigma-Aldrich 99.0 %) were dried at 585 °C before transferred into the glove box. Stoichiometric amounts of the binary oxides together with a 1:4 excess of LiH (Sigma-Aldrich, 95 %) was grinded together with 100 mass % salt (with respect to the reactants) inside the glove box. The mixture was transferred to a tantalum crucible and sealed in a stainless-steel ampoule. The samples were heated at temperatures between 375 and 800 °C. Excess LiCl and LiH were removed by washing with methanol. Note: All experiments must be evaluated with respect to safety. Care must be taken when working with metal hydrides as they react vigorously with water and air. A detailed description is given elsewhere.[1-2]

Home-laboratory XRD measurements were performed on a Bruker AXS D8 Discover instrument with Cu $K_{\alpha 1}$ radiation from a Ge(111) Johansen monochromator in Bragg-Brentano geometry. The mass percent of the different phases were quantified by Rietveld refinements. The Rietveld refinements were carried out in TOPAS V5.[3-4] Six background parameters was used to fit the background and a Thomson-Cox-Hasting to fit the peak shape. The structure was not refined, but obtained from literature.[2]

Neutron diffraction were carried out at room temperature at the two-axis powder diffractometer PUS at the JEEP II reactor at Institute for Energy Technology (IFE), Kjeller, Norway, with a wavelength of 1.55434 Å. The Rietveld refinements were carried out in TOPAS V5.[3-4] A eight polynomial background function was used and a Thompson-Cox-Hastings pseudo-Voigt peak

shape. Lanthanum and neodymium were restricted to have the same atomic position and thermal displacement parameters. Structural information from the refinements are given in Table 1.

Table 1: Crystallographic data of LaNdLiHO$_3$ in space group *Immm* [a = 3.5265(3) Å, b = 3.7248(2) Å, and c = 12.8099(8) Å] from neutron diffraction.

Atom	Wycoff	x	y	z	Occupancy	B_{ISO}
La	4i	0	0	0.36254(12)	0.5	0.09(4)
Nd	4i	0	0	0.36254(12)	0.5	0.09(4)
Li	2a	0	0	0	1	0.40(16)
H	2b	0.5	0	0	1	1.39(11)
O1	4i	0	0	0.17706(17)	1	0.64(4)
O2	2d	0.5	0	0.5	1	0.64(4)

Thermogravimetric (TG) measurements were performed by heating powder samples under a 50 % O$_2$ in N$_2$ atmosphere (both 99.999 %, Praxair) and measuring the mass change as a function of temperature using a Netzsch STA 449 F1 Jupiter instrument. All samples were heated at 10 °C min^{-1} up to 800 °C, where the temperature was held for 120 min. The sample mass was 10.0 ± 1.0 mg for all measured samples and the "flex tangent" method were used to find the decomposition temperature. The buoyancy effect was corrected by subtracting a blank reference scan at exactly the same conditions.

Computational details:

Total energies were calculated by the projected augmented plane-wave (PAW) implementation of the Vienna *ab initio* package (VASP).[5-6] All these calculations were performed with the Perdew, Burke, and Ernzerhof (PBE)[7] exchange correlation functional with the Hubbard parameter correction (GGA+U), following the rotationally invariant form.[8-9] An effective U values of 7.5 eV and 6.2 eV was used for the La and Nd, respectively. The ground-state geometries were determined by minimizing stresses and Hellman-Feynman forces using the conjugate-gradient algorithm with force convergence < 10^{-3} eV Å^{-1}. Brillouin zone integration was performed with a Gaussian broadening of 0.1 eV during all relaxations. 512 k-points in the whole Brillouin zone for the structure with a 600 eV plane-wave cutoff were found sufficient to ensure the required accuracy. The k-points were generated using the Monkhorst-Pack method with a grid size of 8×8×8 for structural optimization. A similar density of k-points and energy cutoffs were used to estimate total energy as a function Nd concentration in La$_{2-x}$Nd$_x$LiHO$_3$ solid solutions. For the initial structure

generation the structural data for La_2LiHO_3 and Nd_2LiHO_3 are taken from ICSD database and we used the *ab initio* random searching structure (AIRSS)[10] method to generate possible model structures for the chosen Nd substitution in La_2LiHO_3 matrix coupled with VASP calculations. Iterative relaxation of atomic positions was stopped when the change in total energy between successive steps was < 1 meV/cell. The heat of formation (ΔH) is calculated using the following equation

$$\Delta H = E_{total}^{La(2-x)NdxLiHO3} - [E_{bulk}^{LiH} + (2-x)\,E_{bulk}^{La2O3} + xE_{bulk}^{Nd2O3}]$$

where $E_{total}^{La(2-x)NdxLiHO3}$, E_{bulk}^{LiH}, E_{bulk}^{La2O3}, and xE_{bulk}^{Nd2O3} are the total energy of the bulk $La_{2-x}Nd_xLiHO$ (in *Immm*), LiH (in *Fm-3m*), La_2O_3 (in *P-3m1*) and Nd_2O_3 (in *P-3m1*), respectively.

A frozen phonon calculation was applied to the supercells using the phonopy program to obtain the phonon dispersion curve and phonon density of states.[11] An atomic displacement of 0.0075 Å was used with a symmetry consideration to obtain the force constants for the phonon calculations. The displacements in opposite directions along all possible axes were incorporated in the calculations to improve the precision. The force calculations were made using the VASP code with the supercell approach (with GGA+*U* correction) and the resulting data were imported into the Phonopy program. The dynamical matrices were calculated from the force constants, and phonon density of states (DOS) curves were computed using the Monkhorst-Pack scheme.[12] Phonon calculations for La_2LiHO_3 and Nd_2LiHO_3 is given in Figure S1 and S2. As no negative vibrational frequencies are encountered, the calculated compounds are considered stable. Phonon calculations was also carried out for Sm_2LiHO_3 with basis in an optimized structure based the structure of La_2LiHO_3. The phonon dispersion and DOS is given in Figure S3. Negative phonon frequencies are encountered for this compound, thus it is considered unstable.
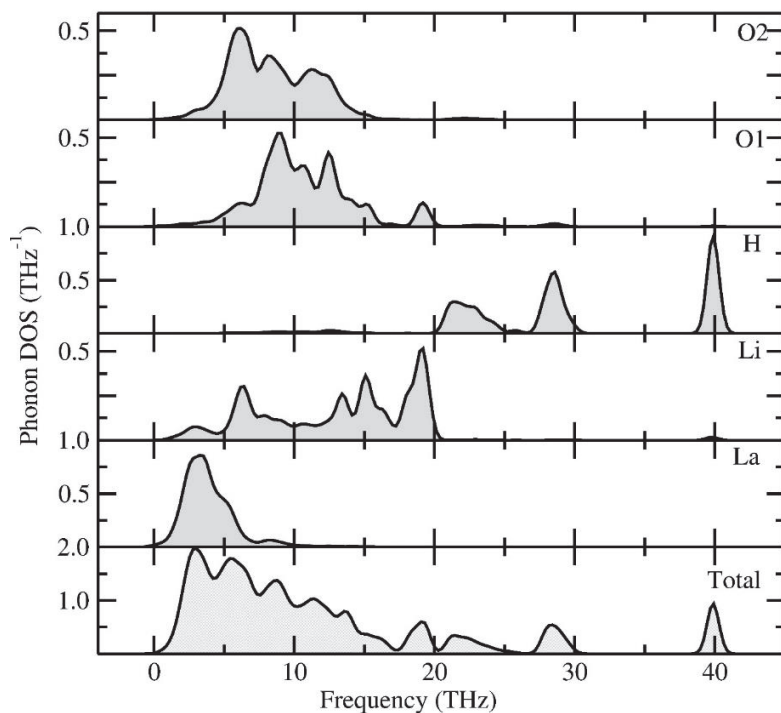
Figure S1: Calculated total and site projected phonon density of states (PDOS) for La$_2$LiHO$_3$.
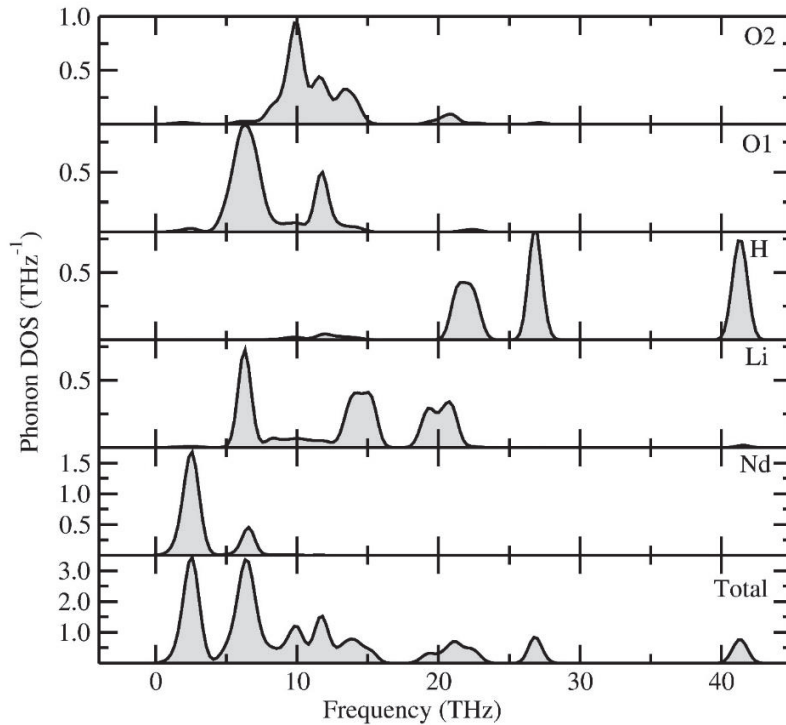
Figure S2: Calculated total and site projected phonon density of states (PDOS) for Nd$_2$LiHO$_3$.
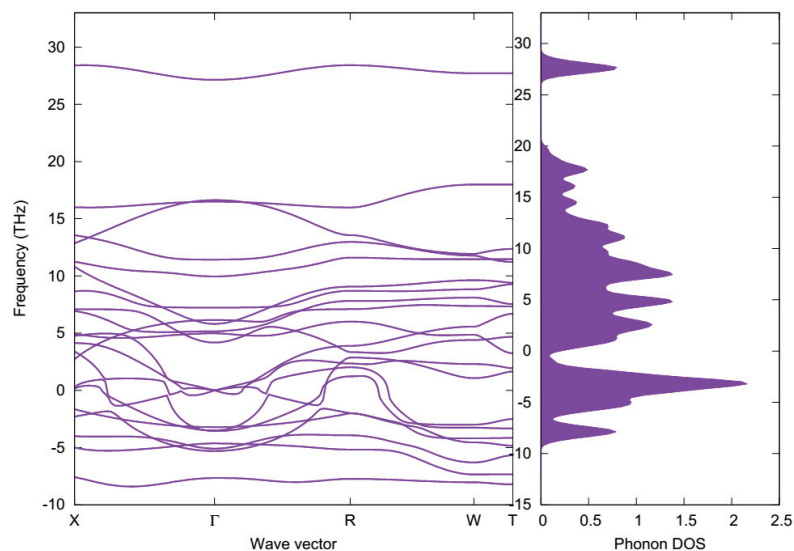
Figure S3: Calculated phonon dispersion and density of states (DOS) of Sm$_2$LiHO$_3$. The structural model is based on the crystal structure of orthorhombic La$_2$LiHO$_3$. Phonons with negative frequencies are encountered, therefore the compound is considered to be unstable.

References:

1.   Schwarz, H., *Neuartige Hydrid-Oxide der Seltenen Erden: Ln2LiHO3 mit Ln = La, Ce, Pr und Nd*. Karlsruhe, 1991.

2.   Fjellvåg, Ø. S.; Armstrong, J.; Sławiński, W. A.; Sjåstad, A. O., Thermal and Structural Aspects of the Hydride-Conducting Oxyhydride La2LiHO3 Obtained via a Halide Flux Method. *Inorg. Chem.* **2017,** *56*, 11123-11128.

3.   Bruker-AXS *TOPAS V5: General profile and structure analysis software for powder diffraction data, Bruker AXS, Karlsruhe, Germany.*, 2013.

4.   Coelho, A., TOPAS and TOPAS-Academic: an optimization program integrating computer algebra and crystallographic objects written in C++. *Journal of Applied Crystallography* **2018,** *51*, 210-218.

5.   Kresse, G.; Furthmüller, J., Efficient iterative schemes for *ab initio* total-energy calculations using a plane-wave basis set. *Phys. Rev. B* **1996,** *54*, 11169-11186.

6.   Kresse, G.; Furthmuller, J., Efficiency of ab-initio total energy calculations for metals and semiconductors using a plane-wave basis set. *Computational Materials Science* **1996,** *6*, 15-50.

7.   Perdew, J. P.; Burke, K.; Ernzerhof, M., Generalized Gradient Approximation Made Simple. *Phys. Rev. Lett.* **1996,** *77*, 3865.

8.   Liechtenstein, A. I.; Anisimov, V. I.; Zaanen, J., Density-functional theory and strong interactions: Orbital ordering in Mott-Hubbard insulators. *Phys. Rev. B* **1995,** *52*, R5467-R5470.

9.   Dudarev, S. L.; Botton, G. A.; Savrasov, S. Y.; Szotek, Z.; Temmerman, W. M.; Sutton, A. P., Electronic Structure and Elastic Properties of Strongly Correlated Metal Oxides from First Principles: LSDA + U, SIC-LSDA and EELS Study of UO_2 and NiO. *Phys. Status Solidi A* **1998,** *166*, 429-443.

10.   Chris, J. P.; Needs, R. J., Ab initio random structure searching. *Journal of Physics: Condensed Matter* **2011,** *23*, 053201.

11.   Togo, A.; Oba, F.; Tanaka, I., First-principles calculations of the ferroelastic transition between rutile-type and SiO_2 at high pressures. *Phys. Rev. B* **2008,** *78*, 134106.

12.   Monkhorst, H. J.; Pack, J. D., Special points for Brillouin-zone integrations. *Phys. Rev. B* **1976,** *13*, 5188-5192.

Paper III

New Insights into Hydride Bonding, Dynamics and Migration in La₂LiHO₃ Oxyhydride

ØS Fjellvåg, J Armstrong, P Vajeeston, AO Sjåstad

III

Paper IV

Crystal structure of LaSr$_3$Fe$_3$O$_9$ and its phase relation with LaSr$_3$Fe$_3$O$_{10}$

ØS Fjellvåg, V Øygarden, MH Sørby, AO Sjåstad

IV

IV

Crystal structure of $LaSr_3Fe_3O_9$ and its phase relation with $LaSr_3Fe_3O_{10}$

Øystein S. Fjellvåg [a], Vegar Øygarden [a], Magnus H. Sørby [b], Anja O. Sjåstad [a,*]

[a] Centre for Materials Science and Nanotechnology, Department of Chemistry, University of Oslo, P.O. Box 1033, N-0315, Oslo, Norway
[b] Department for Neutron Materials Characterization, Institute for Energy Technology, P.O. Box 40, NO-2027, Kjeller, Norway

ARTICLE INFO

ABSTRACT

The Ruddlesden-Popper phase $LaSr_3Fe_3O_{10}$ and its reduced derivatives with nominal composition $LaSr_3Fe_3O_{10-x}$, with $0 < x < 1.21$, are described in detail with respect to crystal structure, magnetic order, thermal stability and likely vacancy mechanisms. The crystal structure of the $LaSr_3Fe_3O_9$ ($x = 1$) phase is described. The $LaSr_3Fe_3O_{10-\delta}$ phase prevails for $x < 0.51$, whereas $LaSr_3Fe_3O_{9\pm\varepsilon}$ prevails for $x > 0.85$. The phases are separated by a two-phase region $0.51 < x < 0.85$. By combined Rietveld refinements of high-resolution powder synchrotron and neutron diffraction, the crystallographic and magnetic structure of $LaSr_3Fe_3O_9$ is described. $LaSr_3Fe_3O_9$ takes a layer like RP3 type structure with features of the brownmillerite structure in the triple perovskite type slabs; unit cell dimensions $a = 28.7562(13)$ Å, $b = 5.5280(2)$ Å, $c = 5.4583(2)$ Å, space group *Cmcm*. $LaSr_3Fe_3O_9$ is an antiferromagnet with $T_N > 350$ K and with a G-type magnetic structure, magnetic space group P_Cbcm. Based on unit cell volume considerations, local oxygen vacancy ordering schemes are suggested.

1. Introduction

Multicomponent transition metal oxides display a wide range of functional properties with potential for applications based on ionic conductivity, magnetic, electrical or optical properties. There is a continuous race for improved and new materials with higher yields, enhanced stability, lower costs, etc. In this respect the perovskite family is of particular interest. Its members display functional properties such as high T_C superconductivity [1], ferroic properties [2], catalytic selectivity [3], colossal magnetoresistance [4] and ionic conductivity [5]. The closely related Ruddlesden-Popper ($A_{n+1}B_nO_{3n+1}$, RPn) type structure is built up of n perovskite layers separated by half a rock salt layer. The layer-like RP compounds exhibits similar physical properties. Moreover, the reduced dimensionality of the 2D-like RP phases may give rise to additional phenomena.

$LaSr_3Fe_3O_{10}$ takes the RP3 type structure and crystallizes in space group $I4/mmm$ [6]. Despite knowing the compound displays oxygen non-stoichiometry, a complete picture of the defect situation is not at hand. Based on neutron diffraction, Lee et al. found that vacancies in $LaSr_3Fe_3O_{10-x}$ form in the middle perovskite layer in the RP3 type structure [6]. This is supported by computer simulations by Tsipis et al. who found that tetrahedral iron in the middle perovskite layer is formed when oxygen is removed from $LaSr_3Fe_3O_{10}$ [7]. Tsipis et al. further suggested that the more strongly reduced $LaSr_3Fe_{2.7}Al_{0.3}O_9$ compound

takes a similar structure to that of orthorhombic $NdSr_3Fe_3O_9$ [7]. $NdSr_3Fe_3O_9$ is an oxygen deficient derivative of the RP3 $NdSr_3Fe_3O_{10}$ and is described as a RP3 compound where the octahedra in the middle perovskite layer are exchanged with tetrahedra, similar to the brownmillerite structure [8,9]. The structural arrangement is thus also similar to the non-stoichiometric perovskite $LaSr_2Fe_3O_{8+y}$, different only in the introduction of an intergrowth layer between the perovskite layers, which is the signature of RP-type structures [10,11]. This is emphasized by the similar Néel temperature of $NdSr_3Fe_3O_9$ and $LaSr_2Fe_3O_{8+y}$ of 600 and 715 ± 5 K, respectively [8,10].

$LaSr_3Fe_3O_{10}$ transforms into $LaSr_3Fe_3O_9$ upon reduction [12]. Although the structure is not reported in detail, $LaSr_3Fe_3O_9$ is indexed in the orthorhombic space group *Bbmm* [12]. The compound shows the unusual property of being able to intercalate water and thereby form a hydrated hydroxide-derivative $LaSr_3Fe_3O_8(OH)_2 \cdot xH_2O$ [12]. The latter material, $LaSr_3Fe_3O_8(OH)_2 \cdot xH_2O$, has attracted attention due to its potential as electrode material for metal-air batteries because of its high ionic conductivity [13].

The current work reports on $LaSr_3Fe_3O_{10-x}$ ($0 < x < 1.2$), as obtained by post-reduction of $LaSr_3Fe_3O_{10}$. We describe the crystal structure and the oxygen vacancy ordering of $LaSr_3Fe_3O_9$ with basis in combined Rietveld refinements of high-resolution powder synchrotron X-ray diffraction (SR-XRD) and powder neutron diffraction (ND). The magnetic properties of $LaSr_3Fe_3O_9$ are characterized by means of magnetization

---

* Corresponding author.
  E-mail address: a.o.sjastad@kjemi.uio.no (A.O. Sjåstad).

(PPMS) studies, whereas the magnetic structure is determined on basis of ND analysis. The stoichiometry and phase-relations between $LaSr_3Fe_3O_{10-\delta}$ and $LaSr_3Fe_3O_{9\pm\varepsilon}$, including their reversible transformation and defect situation, were explored by combination of cerimetric titration, thermogravimetry (TGA), XRD, *in situ* SR-XRD and unit cell volume considerations.

2. Experimental

2.1. Synthesis of oxygen stoichiometric LaSr₃Fe₃O₁₀

$LaSr_3Fe_3O_{10}$ was synthesized by the citric acid method starting from 0.1 M lanthanum-, strontium- and iron(III) nitrate solutions (reactants from Sigma-Aldrich, > 99.9%). Accurate metal content of the nitrate solutions was determined by thermogravimetry. Stoichiometric quantities of the cationic solutions were mixed with excess molten citric acid monohydrate (Sigma-Aldrich, 99.5%) under vigorous stirring. Water and nitrous gasses were evaporated from the solution, thereby forming a gel that was dried overnight at 553 K and calcined at 723 K for 12 h. The obtained black powder was crushed and heat-treated at 1173 K for 12 h, before regrinding and a last annealing at 1573 K for 12 h. Finally, the sample was cooled at a rate of $2.5\,K\,min^{-1}$ to room temperature, giving an oxygen stoichiometry of $LaSr_3Fe_3O_{9.97}$ (cerimetric titration, see details below). All heat treatments were performed in air.

2.2. Preparation of oxygen defective LaSr₃Fe₃O₁₀₋ₓ

$LaSr_3Fe_3O_{10-x}$ samples with controlled oxygen content were obtained by reducing $LaSr_3Fe_3O_{9.97}$ with NbO (99%, Alpha Aesar) according to the reaction:

$$LaSr_3Fe_3O_{10} + x \cdot \frac{2}{3}NbO \rightarrow LaSr_3Fe_3O_{10-x} + x \cdot \frac{1}{3}Nb_2O_5$$
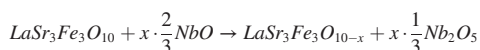
We obtain the reduced complex oxide by loading two alumina crucibles with stoichiometric amounts of $LaSr_3Fe_3O_{10}$ and NbO, and sealing them in a quartz ampule under vacuum before heating to 1173 K for 12 h. To avoid potential re-oxidation, hydration or undesired carbon dioxide uptake, all handling of the ampules were done in an argon filled glovebox from MBraun [12].

Exact oxygen content was determined by cerimetric titration. Mohr salt, $(NH_4)_2Fe(SO_4)_2·6H_2O$ (Sigma-Aldrich, 99%), and a small amount of the sample was dissolved in 1 M HCl. Three parallels were prepared and titrated with 0.1 M $Ce(SO_4)_2$ (Fluka, volumetric). The titration was done in inert Ar (Aga, 5N). Exact formula weight of the Mohr salt was determined gravimetrically (four parallels). The exact concentration of the $Ce(SO_4)_2$ solution was determined separately by titrations with Mohr salt.

2.3. Crystal structure analysis

High-resolution SR-XRD was collected for $LaSr_3Fe_3O_9$ at the Swiss-Norwegian beamline (SNBL, BM01B) at the European Synchrotron Radiation Facility (ESRF, Grenoble, France) for the scattering angle range 1–40.5° in steps of $\Delta(2\theta) = 0.005°$. Monochromatic X-rays were obtained from a channel-cut Si(111) crystal, and LaB₆ was used for wavelength ($\lambda = 0.50513$ Å) and detector calibration. ND data were collected using the two-axis powder diffractometer PUS at the JEEP II reactor at Institute for Energy Technology (IFE), Kjeller, Norway, with $\lambda = 1.5539$ Å [14]. The sample was measured in a cylindrical vanadium sample container sealed with an indium wire. Diffraction patterns were collected at 8 and 298 K, the low-temperature data were obtained in a Displex type cryostat. Data were collected by two detector units, each containing a vertical stack of seven position sensitive ^{3}He detectors each covering 20° in 2θ. The 2θ-range 10–130° was covered by measuring each bank in three different positions. The obtained data were binned in steps of $\Delta(2\theta) = 0.05°$.

The $LaSr_3Fe_3O_9$ crystal structure was simultaneous refined using the high resolution SR-XRD and ND datasets in TOPAS V5 [15,16]. In the combined Rietveld refinement, the parameters restricted to be identical for both datasets are listed in Table S1. The datasets were weighted according to the standard routines in TOPAS V5. For the ND data, a purely nuclear structure and a magnetic structure with just magnetic contribution were refined. Chebyshev polynomials were used for background. The peak shape of the SR-XRD and ND patterns were modeled with full-Voigt and Thompson-Cox-Hastings pseudo-Voigt peak shapes, respectively. The thermal displacement parameters were constrained to be equal for sites with the same elements. The relative occupancy of lanthanum and strontium was refined with the overall sum locked to one. The magnetic structure and space group was identified by ISODISTORT [17]. Due to the symmetry of the magnetic space group, only M_z was refined for the two iron sites.

Isothermal and variable temperature diffraction data of $LaSr_3Fe_3O_{9.22}$ were collected at SNBL (BM01A; wavelength 0.69687 Å) using a Pilatus2M detector and a counting time of 10 s (+10 s read out/wait). $LaSr_3Fe_3O_{9.22}$ was packed and sealed in a 0.3 mm quartz capillary inside an Ar-filled glovebox. The capillary was heated to 663 K, then the tip of the capillary was cut, and the progressing oxidation was monitored by diffraction. The 2D images were integrated using the Fit2D program and rebinned into 1D datasets for the range 1.8–49° in steps of $\Delta(2\theta) = 0.015°$. LaB₆ was used for wavelength and detector calibration. The diffraction patterns (175 in total) were analyzed by surface Rietveld refinements in TOPAS V5 [15,16]. In the surface Rietveld refinement, sample displacement and peak shape was refined as global parameters, while lattice parameters, scale factor and background were refined for the individual diffraction patterns. Atomic positions were not refined, but acquired from the structural determination of $LaSr_3Fe_3O_9$ and from the literature for $LaSr_3Fe_3O_{10}$ [6].

XRD of the reduced phases, $LaSr_3Fe_3O_{10-x}$, were collected in transmission capillary geometry with a Bruker D8-A25 with Ge(111) Johansson monochromator, Lynxeye detector and Cu $K_{\alpha 1}$ radiation at the RECX laboratory, University of Oslo. The samples were packed and sealed in 0.5 mm capillaries inside an Ar filled glove box. Diffraction data were collected for $2\theta = 3$–90°, with a step size of 0.011°. Profile refinements were carried out in TOPAS V5 for accurate determination of unit cell parameters [15,16]. Three samples with composition in a two-phase region were simultaneously refined with two set of unit cell parameters, one set for each phase. The limits of the two-phase region were calculated based on refined phase fractions.

2.4. Thermal and physical characterization

Thermogravimetry (TG) and Differential Scanning Calorimetry (DSC) data were obtained from 298 to 1473 K of approximately 20 mg samples using a combined TGA/DSC Netzsch STA 449 F1 Jupiter instrument, at a heating rate of $1\,K\,min^{-1}$ in N_2 (5 N, AGA) or O_2 (5 N, Praxair) gas flow. N_2 (5 N, Praxair) was used as protective gas for experiments in O_2. The sample was kept in a platinum crucible. The buoyancy effect was corrected for by subtracting a blank reference scan obtained at the same experimental conditions.

Magnetization measurements were performed using a Quantum Design PPMS in the temperature range 4–350 K and an applied field of 10 kOe. Magnetization data measured at lower fields gave poor data due to the antiferromagnetic nature of the material. The $LaSr_3Fe_3O_9$ sample (76.7 mg) was contained in an evacuated high purity quartz ampoule and measured under Zero Field (ZFC) and Field Cooled (FC) conditions.

3. Results and discussion

According to XRD and analysis by cerimetric titration, the as-synthesized $LaSr_3Fe_3O_{10}$ is phase pure with an oxygen stoichiometry of $LaSr_3Fe_3O_{9.97}$. The compound takes a tetragonal (*I4/mmm*) RP3 type structure (Fig. 1a) with lattice parameters $a = 3.8671(3)$ Å and
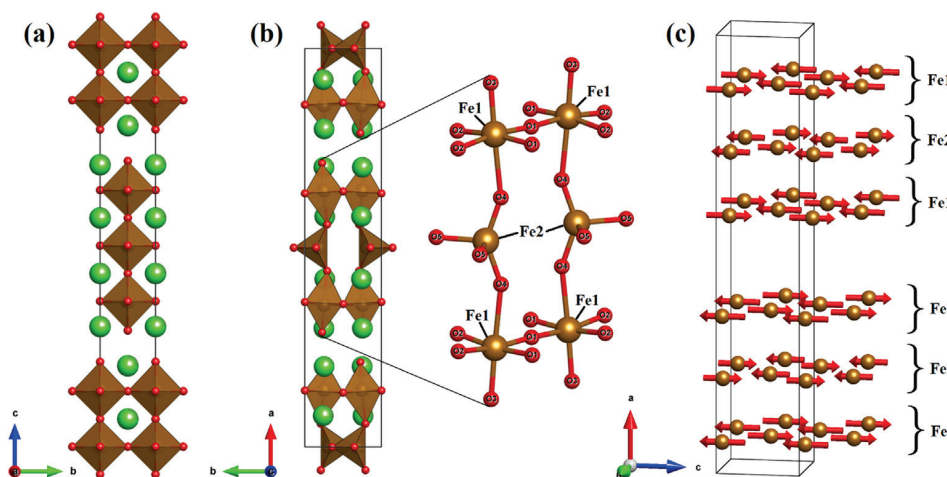
Fig. 1. Crystal structure of (a) $LaSr_3Fe_3O_{10}$ ($I4/mmm$) viewed along the a-axis and (b) $LaSr_3Fe_3O_9$ ($Cmcm$) viewed along the c-axis. In the crystal structure, the octahedra of the middle perovskite layer of the RP3 is now replaced by tetrahedra. Light green, dark green, orange and red spheres correspond to strontium, lanthanum, iron and oxygen atoms. (c): Visualization of the G-type anti-ferromagnetic structure of $LaSr_3Fe_3O_9$ at 8 K described in magnetic space group P_Cbcm. The origin of the magnetic cell is shifted (¼, ¼, 0) relative to the crystallographic cell. Only the iron atoms are displayed. The magnetic moments of the tetrahedral iron atoms (Fe2) are slightly lower than those of the octahedral iron atoms (Fe1), see Table 3. (For interpretation of the references to color in this figure legend, the reader is referred to the Web version of this article.)

$c = 28.018(2)$ Å, in accordance with Lee et al. [6]. With basis in $LaSr_3Fe_3O_{9.97}$, we prepared a series of oxygen deficient samples ($LaSr_3Fe_3O_{10-x}$) with well-defined (nominal) oxygen contents. Careful analysis of the samples showed that they contained either one or two phases; one of the two single phases $LaSr_3Fe_3O_{10}$ ($LaSr_3Fe_3O_{10-\delta}$) and $LaSr_3Fe_3O_9$ ($LaSr_3Fe_3O_{9\pm\varepsilon}$), or a mixture of these two. In the following, we present crystal structural analysis of $LaSr_3Fe_3O_9$ including description of its magnetic properties, and furthermore a phase analysis of $LaSr_3Fe_3O_{10-x}$ in the oxygen stoichiometry range $0 < x < 1.21$.

3.1. Crystal structure, magnetic structure and magnetic properties of $LaSr_3Fe_3O_9$

A full description of the crystal structure of $LaSr_3Fe_3O_9$ is lacking. However, Øygarden et al. indexed its XRD pattern in the orthorhombic space group $Bbmm$ [12], and Barrier et al. reported a structural analysis of the related compound $NdSr_3Fe_3O_9$ in its paramagnetic state at 673 K [8]. We initiated the structural analysis of $LaSr_3Fe_3O_9$ with the available information, first by converting the reported space group $Bbmm$ ($Bbmm$: $a = 5.5479$ Å, $b = 5.4846$ Å, and $c = 28.8846$ Å) to standard settings, *i.e.*

$Cmcm$ ($Cmcm$: $a = 28.8846$ Å, $b = 5.5479$ Å, and $c = 5.4846$ Å). For achieving a precise structural description, we performed combined Rietveld refinements of SR-XRD and ND data (Fig. 2 and Fig. S1). The additional peaks from antiferromagnetic ordering in the ND patterns (8 and 298 K) that were not in accordance with the crystallographic space group, Fig. 2 and Fig. S1, were assigned by ISODISTORT to the magnetic space group P_Cbcm (BNS 57.391) with a cell shifted (¼, ¼, 0) and a propagation vector $k = 0$ [17]. The magnetic structure was successfully refined together with the crystallographic structure, providing a good fit to the peaks with magnetic origin, Fig. 2 and Fig. S1. Illustrations of the crystal- and magnetic structures are presented in Fig. 1b and c. Crystallographic data obtained at 8 and 298 K are summarized in Table 1, Table 2 and Table S2. The magnetic moments extracted from the refined magnetic structure are given in Table 3.

The structure analysis confirms $LaSr_3Fe_3O_9$ to be isostructural to $NdSr_3Fe_3O_9$ and represents hence an ordered oxygen-deficient RP3 phase. The RP3 structure consists of slabs of three perovskite layers separated by a half rock salt layer (Fig. 1a). While in $LaSr_3Fe_3O_9$, the octahedra in the middle layer of the perovskite slab is exchanged with tetrahedra (Fig. 1b and Fig. S2), making the slab similar to the
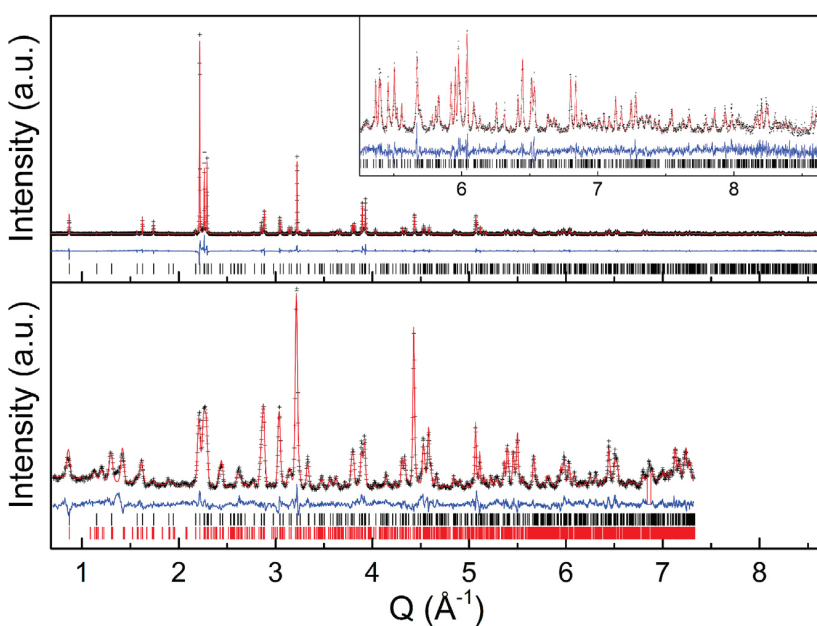

Fig. 2. Observed (black), calculated (red) and difference (blue) intensity profile from combined Rietveld refinements of high resolution SR-XRD (top) and ND (bottom) patterns of $LaSr_3Fe_3O_9$ at 298 K. The positions of Bragg reflections allowed by the crystallographic ($Cmcm$) and magnetic (P_Cbcm) space group are marked with black and red bars, respectively. Black arrows indicate reflections with only magnetic contribution and red arrows indicate reflections with both nuclear and magnetic contribution. The reflection in the ND pattern at 6.9 Å^{-1} is from the cryostat (blue arrow). (For interpretation of the references to color in this figure legend, the reader is referred to the Web version of this article.)

Table 1

Unit cell data and reliability factors for the combined SR-XRD and ND Rietveld refinements of orthorhombic $LaSr_3Fe_3O_9$, space group $Cmcm$. Calculated standard deviations in parentheses.

		8 K	298 K
a (Å)		28.7559(13)	28.8739(4)
b (Å)		5.5279(2)	5.54507(7)
c (Å)		5.4582(2)	5.47804(6)
V (Å³)		867.64(6)	877.076(19)
Z		4	4
R_p	SR-XRD		13.977
	ND	6.768	6.676
R_{wp}	SR-XRD		18.196
	ND	8.745	8.638
R_{exp}	SR-XRD		10.035
	ND	4.076	5.454

brownmillerite- and the $LaSr_2Fe_3O_{8+y}$ framework [8–11]. Hence, the crystal structure of $LaSr_3Fe_3O_9$ can be describes as composed of brownmillerite slabs separated by a half rock salt layer.

By comparing the crystal structures of $LaSr_3Fe_3O_{10}$ and $LaSr_3Fe_3O_9$, it becomes evident that converting the three-layered perovskite slab to a brownmillerite slab leads to an elongation of the slab by ~0.25 Å in the stacking direction. Similar to the brownmillerite and $LaSr_2Fe_3O_{8+y}$ framework, elongation and corresponding volume increase is caused by the expansion of the Fe-O bond in the octahedra directed towards the tetrahedral layer [8–11]. According to the bond valence concept (using the parameters B = 0.37 and R_0 = 1.759) [18], the Fe-O separations in $LaSr_3Fe_3O_9$ correspond to iron valences of 3.07 (Fe1) and 2.85 (Fe2) for the octahedra and the tetrahedra, respectively. This is in good agreement with the expected Fe(III) state based on stoichiometry and the rusty red color of the compound. For $LaSr_3Fe_3O_{10}$, the corresponding bond valence sums are 3.41 and 3.72 for the upper/lower and middle octahedra in the RP3 slab, quite close to the average oxidation state of iron in $LaSr_3Fe_3O_{10}$ of 3.67.

The magnetic structure of $LaSr_3Fe_3O_9$ is unraveled from analysis of ND data in tandem with magnetic susceptibility measurements. Neutron diffraction clearly proves that $LaSr_3Fe_3O_9$ is magnetically ordered at 8 and 298 K and can be described in the magnetic space group P_Cbcm. The analysis shows that $LaSr_3Fe_3O_9$ is a G-type antiferromagnet, Fig. 1c, with a similar spin configuration as $LaSr_2Fe_3O_{8+y}$ [11]. The magnetic moments order antiferromagnetically within the brownmillerite slabs and across the rock salt layer. Thus, the two brownmillerite slabs pictured in Fig. 1c have opposite magnetic spin directions. The magnetic moments are 3.99(5) and 3.58(8) μ_B at 8 K on the octahedral iron (Fe1) and the tetrahedral iron site (Fe2) respectively; the magnetic moments are given in Table 3. The lower magnetic moment on the tetrahedral site is consistent with $LaSr_2Fe_3O_{8+y}$, as reported by Battle et al. [11]. They attributed this to structural disorder on the tetrahedral site lowering the super-exchange interactions, which in turn may be the case for $LaSr_3Fe_3O_9$ as well.

Table 3

Magnetic moments of iron atoms from Rietveld refinements of ND. The symmetry of the magnetic space group, P_Cbcm, allows only refinement of M_z, hence M_x and M_y is zero by symmetry. Calculated standard deviations are given in parentheses.

	M_z Fe1 (μ_B)	M_z Fe2 (μ_B)
8 K	3.99(5)	3.58(8)
298 K	3.24(8)	2.7(1)

The temperature dependence of the magnetic susceptibility (Fig. 3a) supports the antiferromagnetic nature of $LaSr_3Fe_3O_9$ with a transition to the paramagnetic state above the maximum temperature achievable in the PPMS (350 K), possibly similarly to that of $NdSr_3FeO_9$ and $LaSr_2Fe_3O_{8+y}$ which is antiferromagnetic up to 600 and 715 ± 5 K, respectively [8,10]. Notably, field dependent M(H) measurements at 4 K reveal a small hysteresis (Fig. 3b) and a weakly S-shaped M(H) behavior. Currently, we cannot explain this contribution, but it has most likely its origin in a minor impurity (not detected by XRD) obtained during sample preparation. Number of unpaired electrons at high field (H > 80 kOe) is calculated to be 0.14 at 4 K. This low value confirms the strong antiferromagnetic coupling in the material.

3.2. Oxygen deficiency in $LaSr_3Fe_3O_{10-x}$ and phase relations between $LaSr_3Fe_3O_{10-\delta}$ and $LaSr_3Fe_3O_{9\pm\varepsilon}$

Thermogravimetry of $LaSr_3Fe_3O_{9.97}$ upon heating/cooling cycles in O_2 and N_2 (Fig. 4) shows that the oxygen vacancy concentration depends on both temperature and pO_2. For example, at 1473 K, $x = 0.76$ in O_2, and $x = 1.21$ in N_2. In addition, upon subsequent cooling in O_2 from 1473 K the sample returns almost to its initial fully oxidized state, whereas on cooling in N_2 the sample stabilizes with an oxygen content of $x = 0.90$. The modest re-oxidation in N_2 during the cooling step is most likely due to oxygen impurities in the N_2-gas. Upon heating in N_2, $LaSr_3Fe_3O_{10}$ arrives at the composition of the $LaSr_3Fe_3O_9$ phase, indicating a reversible transformation between the two compounds. Furthermore, the TGA experiments illustrate the system's ability to release and incorporate oxygen in a reversible manner. We observe a weak plateau in the TGA curves at $x = 0.2$ on heating in both N_2 and O_2, and in N_2 we note a distinct change in curvature at $x = 1.0$. These changes are probably indicative of changes in the oxygen vacancy mechanism.

TGA shows that $LaSr_3Fe_3O_{10-x}$ has a huge span in oxygen content. Correspondingly, $LaSr_3Fe_3O_{10-\delta}$ and $LaSr_3Fe_3O_{9\pm\varepsilon}$ appears as two distinct phases with significant differences in their crystal structures. To correlate the structural state with the overall oxygen content, a series of $LaSr_3Fe_3O_{10-x}$ $(0 < x < 1)$ compositions were prepared by controlled NbO reduction followed by cerimetric titration and structural analysis. The combined structural and oxygen content analysis (Fig. 5) show that unit cell volumes of $LaSr_3Fe_3O_{10-\delta}$ and $LaSr_3Fe_3O_{9\pm\varepsilon}$ vary significantly with oxygen deficiency concentration and reveal that $LaSr_3Fe_3O_{10-\delta}$ retains its structure to $\delta = 0.51$ ($LaSr_3Fe_3O_{9.49}$). For the interval $0.51 < x < 0.85$, the two phases $LaSr_3Fe_3O_{10-\delta}$ and $LaSr_3Fe_3O_{9\pm\varepsilon}$ co-

Table 2

Crystal structure data for $LaSr_3Fe_3O_9$ as obtained from combined Rietveld refinement of SR-XRD and ND data (space group $Cmcm$; 8 K) giving lattice parameters of $a = 28.7559(13)$ Å, $b = 5.5280(2)$ Å, $c = 5.4583(2)$ Å. Calculated standard deviations are given in parentheses.

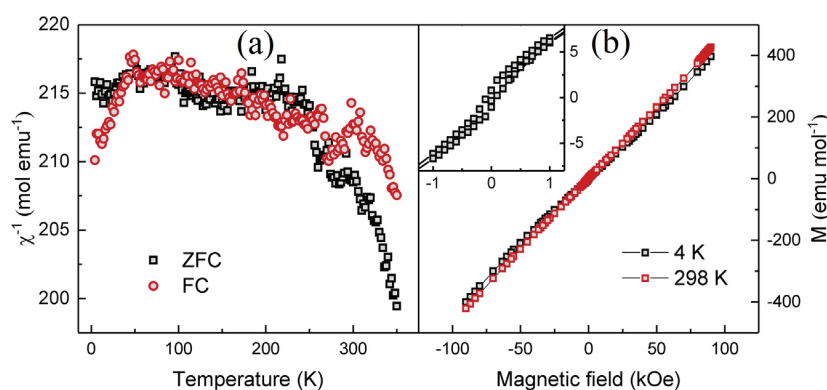| Atom	Wyckoff	x	y	z	Occupancy	U_{iso}
La1	8 g	0.20181(6)	0.2520(4)	0.25	0.2157(10)	0.0058(6)
Sr1	8 g	0.20181(6)	0.2520(4)	0.25	0.7843(10)	0.0058(6)
La2	8 g	0.07850(7)	0.2399(4)	0.25	0.2843(10)	0.0058(6)
Sr2	8 g	0.07850(7)	0.2399(4)	0.25	0.7157(10)	0.0058(6)
Fe1	8 g	0.64349(10)	0.2483(7)	0.25	1	0.0096(4)
Fe2	4c	0	0.6892(7)	0.25	1	0.0096(4)
O1	8e	0.8587(3)	0	0	1	0.0077(8)
O2	8e	0.6360(2)	0	0	1	0.0077(8)
O3	8 g	0.71285(17)	0.2248(12)	0.25	1	0.0077(8)
O4	8 g	0.55865(18)	0.2939(12)	0.25	1	0.0077(8)
O5	8f	0	0.358(2)	0.359(2)	0.5	0.0077(8)

Fig. 3. (a) Temperature dependence of the inverse molar magnetic susceptibility of $LaSr_3Fe_3O_9$ at ZFC and FC conditions and measured in a filed of 10 kOe. (b) Field dependence of the molar magnetization of $LaSr_3Fe_3O_9$ at 4 K (black) and 298 K (red). The inset shows a small hysteresis. (For interpretation of the references to color in this figure legend, the reader is referred to the Web version of this article.)
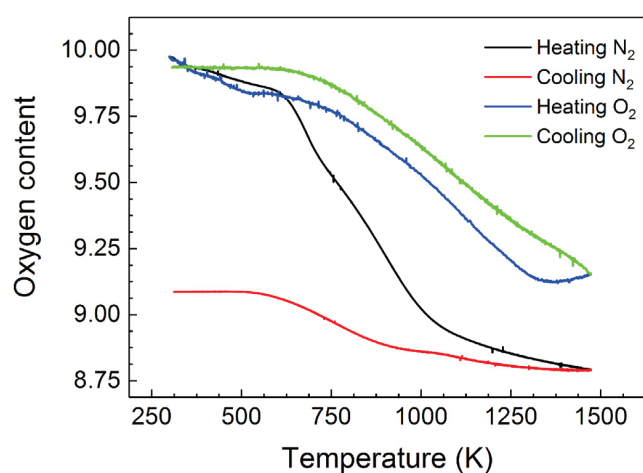

Fig. 4. Oxygen content as determined by TGA for $LaSr_3Fe_3O_{9.97}$ in N_2 and O_2, heating rate 1 K min^{-1}. The black and blue curves show mass loss during heating in N_2 and O_2, while the red and green curves show re-oxidation during cooling to room temperature in N_2 and O_2. (For interpretation of the references to color in this figure legend, the reader is referred to the Web version of this article.)

Fig. 5. Phase relations and unit cell volumes of $LaSr_3Fe_3O_{10-\delta}$ (red spheres) and $LaSr_3Fe_3O_{9\pm\varepsilon}$ (blue spheres) for $LaSr_3Fe_3O_{10-x}$ samples prepared by means of controlled oxygen reduction. The shaded area illustrates the two-phase region ($0.51 < x < 0.85$). The size of symbols illustrates the mole fraction of the individual phases in the two-phase region. (For interpretation of the references to color in this figure legend, the reader is referred to the Web version of this article.)

exists, whereas for $x > 0.85$ non-stoichiometric $LaSr_3Fe_3O_{9\pm\varepsilon}$ is the stable configuration. $LaSr_3Fe_3O_{9\pm\varepsilon}$ is associated with a small, yet significant solid solution range of oxygen; $\varepsilon < 0.15$. Furthermore, TGA (Fig. 4) suggest that the $LaSr_3Fe_3O_{9\pm\varepsilon}$ phase also exists with oxygen vacancies up to $x = 1.21$ (*i.e.* $LaSr_3Fe_3O_{8.79}$). The latter finding is in good agreement with observations for the isostructural $NdSr_3Fe_3O_9$ compound [8,9].

The TGA study shows that oxidation and reduction are fast reactions (Fig. 4). However, the structural analysis at 295 K documents that $LaSr_3Fe_3O_{9\pm\varepsilon}$ and $LaSr_3Fe_3O_{10-\delta}$ are two distinct phases, crystallizing in orthorhombic and tetragonal symmetries, respectively. On that basis, we expect a discontinuity, or a two-phase region, connecting the reduced and oxidized variants. This is confirmed by the unit cell volumes of the tailor-made oxygen stoichiometry samples (Fig. 5). In order to clarify the transition between the two phases, an *in-situ* SR-XRD experiment was carried out. A sample with initial nominal composition $LaSr_3Fe_3O_{9.22}$ (*i.e.*, at the verge to two-phase region with $LaSr_3Fe_3O_{9\pm\varepsilon}$ as the dominant phase) was heated to 663 K in a closed capillary. Regular thermal expansion was observed, and at 663 K the capillary was opened to the air while the progressing oxidation of the sample was monitored.

By inspection of the diffraction patterns (Fig. 6), it is evident that the sample is composed of $LaSr_3Fe_3O_{9\pm\varepsilon}$ and $LaSr_3Fe_3O_{10-\delta}$ at 663 K and that no other high temperature phase is formed. No continuous conversion of $LaSr_3Fe_3O_{9\pm\varepsilon}$ into $LaSr_3Fe_3O_{10-\delta}$ is observed, *i.e.* they exist as a two-

phase mixture while the phase fraction changes during the progressing oxidation. Further, in the early stage of the oxidation process, we clearly observe that the (117) reflection of $LaSr_3Fe_3O_{10-\delta}$ moves to higher Q, and thus a smaller unit cell volume (Fig. 6). This indicates oxidation of $LaSr_3Fe_3O_{10-\delta}$, consistent with the ability to incorporate oxygen in vacant sites. The process was quantified through surface Rietveld refinements, and Fig. S3 shows the evolution of the unit cell volume of $LaSr_3Fe_3O_{10-\delta}$ and phase fractions throughout the oxidation. Initially, the unit cell volume decreases rapidly, followed by a more moderate contraction. This shows that $LaSr_3Fe_3O_{10-\delta}$ is continuously incorporating oxygen throughout the entire experiment. The initial rapid decrease in the cell volume is attributed to the system's response to the change in partial pO_2 over the sample when the capillary was cut open.

3.3. Vacancy formation and vacancy ordering in $LaSr_3Fe_3O_{10-\delta}$ and $LaSr_3Fe_3O_{9\pm\varepsilon}$

In general, iron cations are well known to coordinate as octahedra (6), tetragonal pyramids (5) or tetrahedra (4), and in some rare cases also in square planar (4) coordination ($SrFeO_2$) [19]. Concerning $LaSr_3Fe_3O_{10}$,
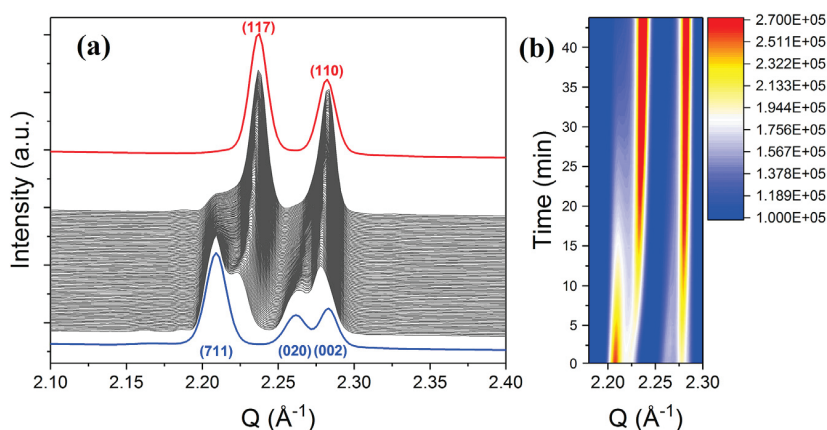
Fig. 6. (a) Stacked *in situ* SR-XRD patterns for oxidation of $LaSr_3Fe_3O_{9.22}$ in an open capillary at 663 K versus time. The blue (first) and red (last) patterns are the calculated intensities associated with orthorhombic $LaSr_3Fe_3O_{9\pm\varepsilon}$ and tetragonal $LaSr_3Fe_3O_{10-\delta}$ in the first and the last diffraction pattern, respectively. Miller indices are given for the respective reflections. Phase fractions from Rietveld refinements are shown in Fig. S3. (b) Contour plot illustrating the evolution of the diffraction pattern of the $LaSr_3Fe_3O_{9\pm\varepsilon}$ and $LaSr_3Fe_3O_{10-\delta}$ versus time in the same *Q*-region as (a). Note that the sample is in a two-phase region though the entire experiment. (For interpretation of the references to color in this figure legend, the reader is referred to the Web version of this article.)

Table 4

Volume expansion slopes derived from linear regression of the volume versus B-cation oxidation state. .

System	$SrFeO_{3-x}$	$LaCoO_{3-x}$	$LaSr_3Fe_3O_{10-\delta}$	$LaSr_3Fe_3O_{9\pm\varepsilon}$
Vacancy type	Tetragonal pyramids [20]	Tetrahedra [21,22]	Unknown	Tetrahedra
Slope	−1.42	−5.33	−3.01 −2.32[a] −3.80[b]	−5.76

[a] Derived value for the two data points with largest unit cell volume of $LaSr_3Fe_3O_{10-\delta}$ ($\delta = 0.03$ and 0.17) in Fig. 5.
[b] Derived value for the two data points with smallest unit cell volume of $LaSr_3Fe_3O_{10-\delta}$ ($\delta = 0.33$ and 0.41) in Fig. 5.

Tsipis et al. suggested that oxygen vacancies are located to the central layer of the perovskite slab giving rise to tetrahedrally coordinated iron [7]. In Fig. 5, we observe that the unit cell volumes of $LaSr_3Fe_3O_{10-\delta}$ and $LaSr_3Fe_3O_{9\pm\varepsilon}$ vary significantly with oxygen deficiency concentration. With basis in unit cell volume considerations due to oxygen deficiency in $SrFeO_{3-x}$ ($SrFeO_3$, $Sr_8Fe_8O_{23}$, $Sr_4Fe_4O_{11}$) and $LaCoO_{3-x}$ ($LaCoO_3$, $La_3Co_3O_8$, $La_2Co_2O_5$), one may identify the likely local vacancy ordering scheme in $LaSr_3Fe_3O_{10-\delta}$ and $LaSr_3Fe_3O_{9\pm\varepsilon}$. $SrFeO_{3-x}$ and $LaCoO_{3-x}$ represent two different vacancy situations; 5-coordinated tetragonal pyramids and 4-coordinated tetrahedra, respectively [20–22]. Based on literature data for these two ABO_{3-x} systems, the volume expansion as a function of oxidation state of the B-cations in $SrFeO_{3-x}$ and $LaCoO_{3-x}$ are plotted along with corresponding data for $LaSr_3Fe_3O_{10-\delta}$ and $LaSr_3Fe_3O_{9\pm\varepsilon}$ in Fig. S4. The volume - composition slopes are reported in Table 4.

From Table 4 (and Fig. S4) we note that the local vacancy ordering influences the unit cell volume expansion significantly as seen by comparing data for $SrFeO_{3-x}$ and $LaCoO_{3-x}$. Both $LaCoO_{3-x}$ and $LaSr_3Fe_3O_{9\pm\varepsilon}$ the B site cations partly take tetrahedral coordination and the volume slopes are similar (−5.33 and −5.76). The similar slopes are a signature of both these systems having tetrahedra as their local ordering scheme of vacancies. When it comes to $LaSr_3Fe_3O_{10-\delta}$, the situation is less clear with an average volume slope of −3.01, *i.e.* an intermediate situation relative to local vacancy ordering by tetrahedra (−5.33) and by tetragonal pyramids (−1.42). This may indicate that both these local configurations exist in oxygen deficient $LaSr_3Fe_3O_{10-\delta}$.

By considering Fig. 5 in more detail, a small change in the unit cell volume slope is seen around $x = 0.25$, *cf.* also Table 4 and Fig. S4. Although the change is small, the TGA data in Fig. 4 shows a clear feature at approximately the same oxygen content. Note, the kink in TGA is at higher temperatures, whereas Fig. 5 represents a quenched situation at NbO reducing conditions. These observations suggest a composition mediated change in the local vacancy ordering mechanism. The two

observed volume slopes of $LaSr_3Fe_3O_{10-\delta}$ are −2.32 for $\delta < 0.25$ and −3.80 for $\delta > 0.25$. Although neither of these clearly support one ordering scheme above the other, we suggest that initial formation of tetragonal pyramids is replaced by tetrahedra at high vacancy concentrations. To fully reveal the vacancy-ordering situation, we suggest revisiting the system by computational modelling and to perform pair distribution function (PDF) analysis of ND data as the next steps.

4. Summary

This study is the first report on the crystal- and magnetic structure of $LaSr_3Fe_3O_9$. The title compound is isostructural to $NdSr_3Fe_3O_9$. By means of magnetization and ND we conclude that $LaSr_3Fe_3O_9$ is a G-type antiferromagnet, described in the magnetic space group P_Cbcm, with a Néel temperature above 350 K possible similar to that of $NdSr_3FeO_9$ and $LaSr_2Fe_3O_{8+y}$ [8,10]. TGA shows that the $LaSr_3Fe_3O_{10-x}$ phases can reversibly accommodate and release oxygen in the range $0 < x < 1.21$. However, in this wide oxygen range, two distinct RP3 like phases are occurring; $LaSr_3Fe_3O_{10-\delta}$ and $LaSr_3Fe_3O_{9\pm\varepsilon}$, separated by a two-phase region. By combining information from TGA and structural considerations, we propose that oxygen deficient $LaSr_3Fe_3O_{10-\delta}$ initially form local oxygen vacancy ordering through tetragonal pyramids, which is replaced by tetrahedra at higher vacancy concentrations. We suggest this issue is carefully addressed in future work by computational modelling and PDF analysis of ND.

Appendix A. Supplementary data

Supplementary data to this article can be found online at https://doi.org/10.1016/j.jssc.2019.03.050.

References

[1] D.W. Murphy, S. Sunshine, R.B. van Dover, R.J. Cava, B. Batlogg, S.M. Zahurak, L.F. Schneemeyer, New superconducting cuprate perovskites, Phys. Rev. Lett. 58 (18) (1987) 1888–1890.
[2] H. Liu, X. Yang, A brief review on perovskite multiferroics, Ferroelectrics 507 (1) (2017) 69–85.

[3] F. Polo-Garzon, Z. Wu, Acid–base catalysis over perovskites: a review, J. Mater. Chem. A 6 (7) (2018) 2877–2894.

[4] B. Raveau, A. Maignan, C. Martin, M. Hervieu, Colossal magnetoresistance manganite Perovskites: relations between crystal chemistry and properties, Chem. Mater. 10 (10) (1998) 2641–2652.

[5] D. Pergolesi, E. Fabbri, A. D'Epifanio, E. Di Bartolomeo, A. Tebano, S. Sanna, S. Licoccia, G. Balestrino, E. Traversa, High proton conduction in grain-boundary-free yttrium-doped barium zirconate films grown by pulsed laser deposition, Nat. Mater. 9 (2010) 846.

[6] J.Y. Lee, J.S. Swinnea, H. Steinfink, W.M. Reiff, S. Pei, J.D. Jorgensen, The crystal chemistry and physical properties of the triple layer perovskite intergrowths $LaSr_3Fe_3O_{10-\delta}$ and $LaSr_3(Fe_{3-x}Al_x)O_{10-\delta}$, J. Solid State Chem. 103 (1) (1993) 1–15.

[7] E.V. Tsipis, E.N. Naumovich, M.V. Patrakeev, P.V. Anikina, J.C. Waerenborgh, V.V. Kharton, Defect interactions in $Sr_3La(Fe,Al)_3O_{10-\delta}$ by computer simulations and mössbauer spectroscopy, Chem. Mater. 21 (21) (2009) 5072–5078.

[8] N. Barrier, D. Pelloquin, N. Nguyen, M. Giot, F. Bourée, B. Raveau, Ferrite $Sr_3NdFe_3O_9$: an original intergrowth between the brownmillerite and K_2NiF_4-type structures, Chem. Mater. 17 (26) (2005) 6619–6623.

[9] D. Pelloquin, J. Hadermann, M. Giot, V. Caignaert, C. Michel, M. Hervieu, B. Raveau, Novel, oxygen-deficient n = 3 RP-member $Sr_3NdFe_3O_{9-\delta}$ and its topotactic derivatives, Chem. Mater. 16 (9) (2004) 1715–1724.

[10] P.D. Battle, T.C. Gibb, S. Nixon, A study of the ordering of oxygen vacancies in the nonstoichiometric perovskite $Sr_2LaFe_3O_{8+y}$ by Mössbauer spectroscopy and a comparison with $SrFeO_{3-y}$, J. Solid State Chem. 79 (1) (1989) 75–85.

[11] P.D. Battle, T.C. Gibb, P. Lightfoot, The crystal and magnetic structures of $Sr_2LaFe_3O_8$, J. Solid State Chem. 84 (2) (1990) 237–244.

[12] V. Øygarden, H. Fjellvåg, M.H. Sørby, A.O. Sjåstad, Crystal structure of $LaSr_3Fe_3O_8(OH)_2 \cdot xH_2O$, Inorg. Chem. 55 (15) (2016) 7630–7636.

[13] T. Takeguchi, T. Yamanaka, H. Takahashi, H. Watanabe, T. Kuroki, H. Nakanishi, Y. Orikasa, Y. Uchimoto, H. Takano, N. Ohguri, M. Matsuda, T. Murota, K. Uosaki, W. Ueda, Layered perovskite oxide: a reversible air electrode for oxygen evolution/reduction in rechargeable metal-air batteries, J. Am. Chem. Soc. 135 (30) (2013) 11125–11130.

[14] B.C. Hauback, H. Fjellvåg, O. Steinsvoll, K. Johansson, O.T. Buset, J. Jørgensen, The high resolution powder neutron diffractometer PUS at the JEEP II reactor at Kjeller in Norway, J. Neutron Res. 8 (3) (2000) 215–232.

[15] Bruker-AXS, TOPAS V5: General Profile and Structure Analysis Software for Powder Diffraction Data, Bruker AXS, Karlsruhe, Germany., 2013.

[16] A. Coelho, TOPAS and TOPAS-Academic: an optimization program integrating computer algebra and crystallographic objects written in C++, J. Appl. Crystallogr. 51 (1) (2018) 210–218.

[17] H.T. Stokes, D.M. Hatch, B.J. Campbell, D.E. Tanner, Isodisplace: a web-based tool for exploring structural distortions, J. Appl. Crystallogr. 39 (4) (2006) 607–614.

[18] I.D. Brown, D. Altermatt, Bond-valence parameters obtained from a systematic analysis of the inorganic crystal structure database, Acta Crystallogr. Sect. B 41 (4) (1985) 244–247.

[19] Y. Tsujimoto, C. Tassel, N. Hayashi, T. Watanabe, H. Kageyama, K. Yoshimura, M. Takano, M. Ceretti, C. Ritter, W. Paulus, Infinite-layer iron oxide with a square-planar coordination, Nature 450 (2007) 1062.

[20] J.P. Hodges, S. Short, J.D. Jorgensen, X. Xiong, B. Dabrowski, S.M. Mini, C.W. Kimball, Evolution of oxygen-vacancy ordered crystal structures in the perovskite series $Sr_nFe_nO_{3n-1}$ (n=2, 4, 8, and ∞), and the relationship to electronic and magnetic properties, J. Solid State Chem. 151 (2) (2000) 190–209.

[21] O.H. Hansteen, H. Fjellvåg, B.C. Hauback, Crystal structure and magnetic properties of $La_2Co_2O_5$, J. Solid State Chem. 141 (2) (1998) 411–417.

[22] O.H. Hansteen, H. Fjellvåg, B.C. Hauback, Crystal structure, thermal and magnetic properties of $La_3Co_3O_8$. Phase relations for $LaCoO_{3-\delta}$ ($0.00 \leq \delta \leq 0.50$) at 673 K, J. Mater. Chem. 8 (9) (1998) 2081–2088.

Crystal structure of $LaSr_3Fe_3O_9$ and its phase relation with $LaSr_3Fe_3O_{10}$

Øystein S. Fjellvåg,[†] Vegar Øygarden,[†] Magnus H. Sørby,[‡] Anja O. Sjåstad,[†*]

[†] Centre for Materials Science and Nanotechnology, Department of Chemistry, University of Oslo, P.O. Box 1033, N–0315 Oslo, Norway

[‡] Department for Neutron Materials Characterization, Institute for Energy Technology, P.O. Box 40, NO-2027 Kjeller, Norway

Tables:

Table S1: Characteristic features of the SR–XRD and ND datasets and list of refined parameters. "a" gives parameters parameters restricted to be the same for both datasets.

	SR–XRD		ND		
Measured data points	7901		2400		
Reflections	689		426		
λ (Å)	0.50513		1.5539		
Scale factor	1		1		
Zero point	1		1		
Profile parameters	4		4		
Anisotropic line broadening		7[a]			
Unit cell dimensions		3[a]			
Positional parameters		15[a]			
Isotropic displacement parameters		3[a]			
Occupational parameters		1[a]			
Magnetic components			1		
Background coefficients	6		6		
Absorption correction	1				
Refined parameters	13 +	29 +	13	=	55

1

Table S2: Crystal structure data for $LaSr_3Fe_3O_9$ as obtained from combined Rietveld refinement of SR–XRD and PND in space group Cmcm at 298 K giving lattice parameters of a = 28.8738(4) Å, b = 5.54507(7) Å, c = 5.47804(6) Å. Calculated standard deviations are given in parentheses.

| Atom	Wyckoff	x	y	z	Occupancy	U_{iso}
La1	8g	0.20190(6)	0.2515(4)	0.25	0.2103(10)	0.0071(8)
Sr1	8g	0.20190(6)	0.2515(4)	0.25	0.7897(10)	0.0071(8)
La2	8g	0.07849(6)	0.2399(4)	0.25	0.2897(10)	0.0071(8)
Sr2	8g	0.07849(6)	0.2399(4)	0.25	0.7103(10)	0.0071(8)
Fe1	8g	0.64348(12)	0.2485(7)	0.25	1	0.0109(4)
Fe2	4c	0	0.6896(7)	0.25	1	0.0109(4)
O1	8e	0.8585(3)	0	0	1	0.0114(3)
O2	8e	0.6363(3)	0	0	1	0.0114(3)
O3	8g	0.7124(2)	0.2241(15)	0.25	1	0.0114(3)
O4	8g	0.5583(2)	0.2916(15)	0.25	1	0.0114(3)
O5	8f	0	0.355(3)	0.363(3)	0.5	0.0114(3)

Figures:
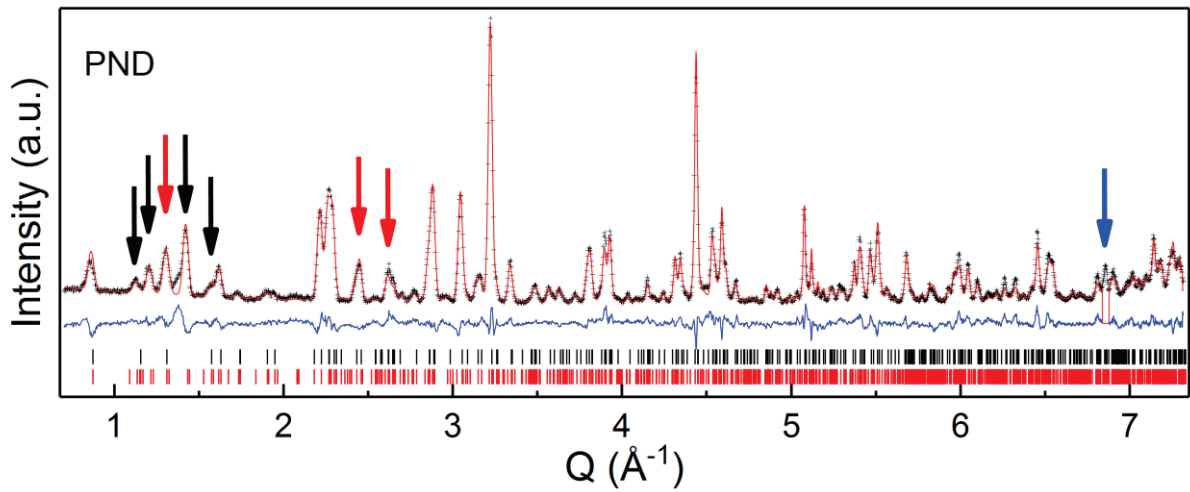
Figure S1: Observed (black), calculated (red) and difference (blue) intensity profile from Rietveld refinement of ND pattern of $LaSr_3Fe_3O_9$ at 8 K. The positions of Bragg reflections allowed by the crystallographic (*Cmcm*) and magnetic (*Pcbcm*) space group are marked with black and red bars, respectively. Black arrows indicate reflections with only magnetic contribution and red arrows indicate reflections with both nuclear and magnetic contribution. The reflection in the ND pattern at 6.9 Å⁻¹ is from the cryostat (blue arrow).
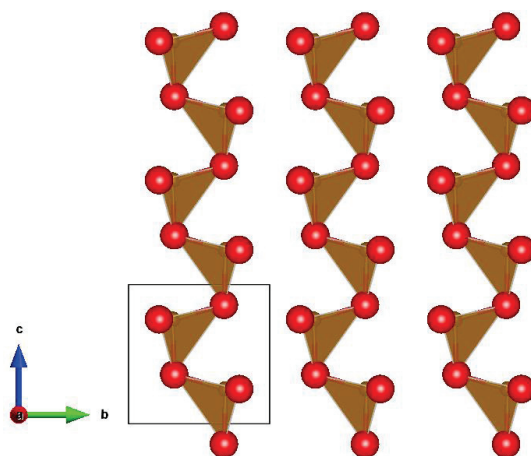
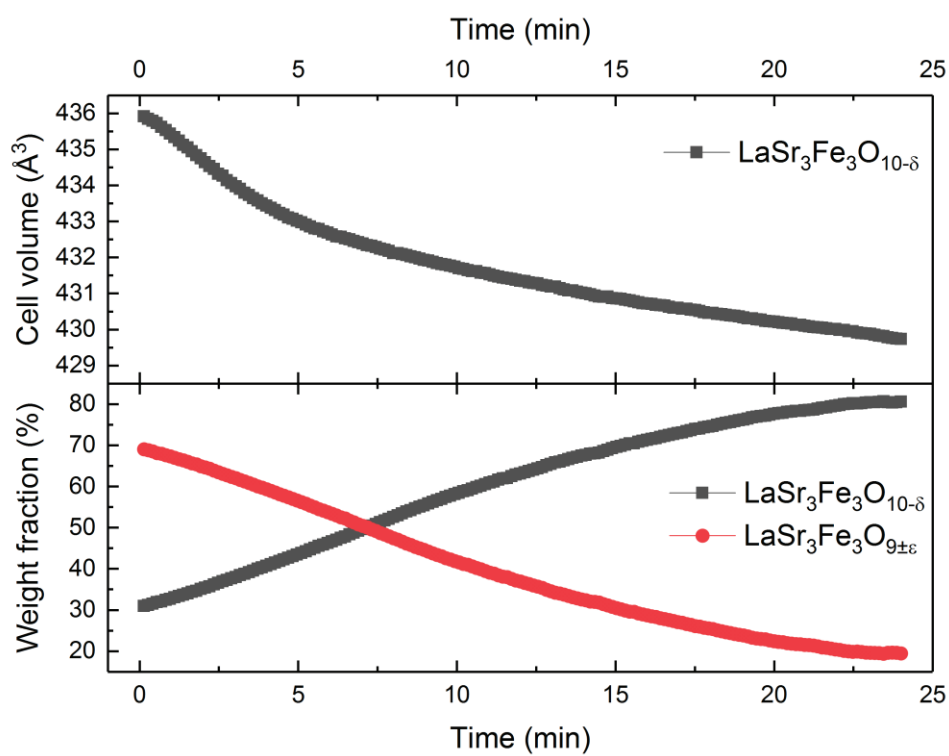**Figure S2: Illustration of the FeO$_4$ chains in the brownmillerite like layer viewed along the a–axis.**

Figure S3: Evolution of cell volume of LaSr$_3$Fe$_3$O$_{10-\delta}$ (top) and evolution of phase fractions for LaSr$_3$Fe$_3$O$_{10-\delta}$ and LaSr$_3$Fe$_3$O$_{9\pm\epsilon}$ during isothermal oxidation at 663 K from Rietveld refinements.
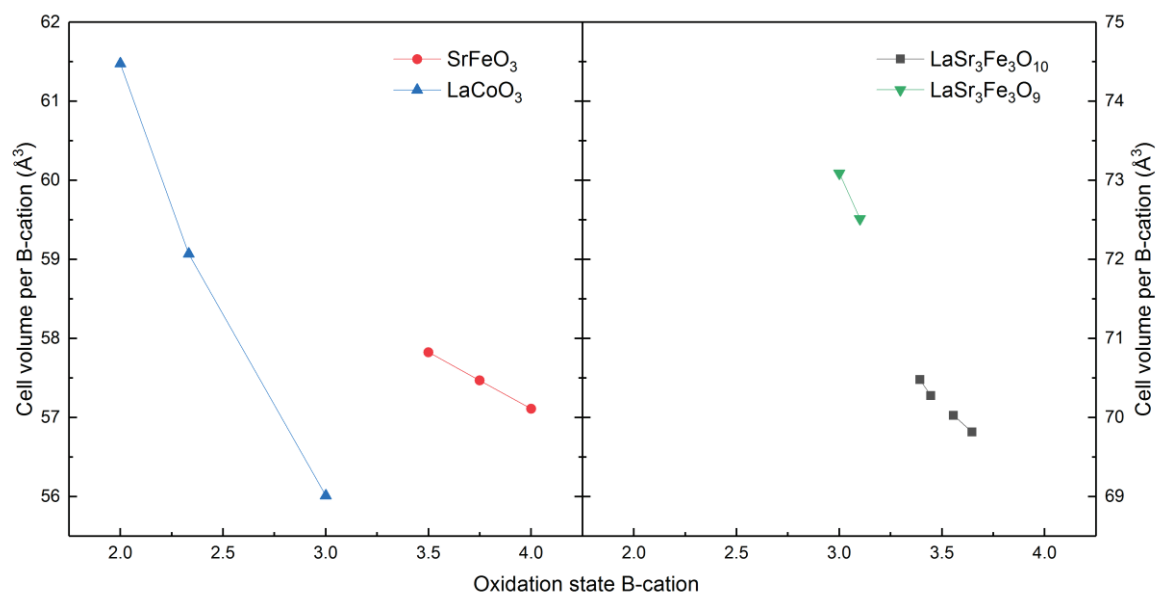
Figure S4: Cell volume per B-cation as a function of oxidation state.